5-4-2018

Material Characterization using Laser-Induced Breakdown Spectroscopy

Chet Raj Bhatt

Material characterization using laser-induced breakdown spectroscopy

By

Chet Raj Bhatt

A Dissertation
Submitted to the Faculty of
Mississippi State University
in Partial Fulfillment of the Requirements
for the Degree of Doctor of Philosophy
in Engineering with an Emphasis in Applied Physics
in the Department of Physics and Astronomy

Mississippi State, Mississippi

May 2018

Material characterization using laser-induced breakdown spectroscopy

By

Chet Raj Bhatt

Approved:

_____

Hendrik F. Arnoldus
(Major Professor and Graduate Coordinator)

_____

Jagdish P. Singh
(Director of Dissertation)

_____

David L. Monts
(Committee Member)

_____

Dustin McIntyre
(Committee Member)

_____

Ratneshwar Jha
(Committee Member)

_____

Jason M. Keith
Dean
Bagley College of Engineering

Name: Chet Raj Bhatt

Date of Degree: May 4, 2018

Institution: Mississippi State University

Major Field: Engineering with an Emphasis in Applied Physics

Major Professor: Hendrik F. Arnoldus

Title of Study: Material characterization using laser-induced breakdown spectroscopy

Pages in Study 154

Candidate for Degree of Doctor of Philosophy

Laser-induced breakdown spectroscopy (LIBS) has been established as a rapid, *in situ*, and real-time spectroscopic analytical technique for material characterization. It is very handy for the study of all kinds of materials irrespective of their state. After being used for a Mars mission, LIBS has gained global attention and many scientific researches are investigating its applications. The main objective of this dissertation is to study the possibility of using laser spectroscopic sensing techniques for material characterization and if possible, to develop methodologies.

Studying molecular emission spectra for elemental analysis is a relatively new trend in the spectroscopic field. Molecular emission from SrCl and SrO observed in LIBS spectra were analyzed and compared with atomic emission from Sr. Calibration models were developed using both molecular bands and atomic spectral peaks.

The determination of nutritional elements in crops, vegetables, and fruits is very important to evaluate their nutritional status. The LIBS technique was applied to identify the nutritional elements present in cauliflower and broccoli, and to evaluate the difference between organic and conventional vegetables in terms of nutritional elements. Principal

component analysis (PCA) and one-to-one comparison using Student's t-test were employed for discrimination between organic and conventional vegetable flowers.

Early iron and steel production in the state of Pennsylvania (United States) mostly utilized blast furnaces that were operated by charcoal as a primary fuel, followed by anthracite, then coke. The process left behind a by-product known as blast furnace slag. Blast furnace slag, non-metallic in nature, appears to have various industrial applications. LIBS was used for the analysis of charcoal blast furnace slags and qualitative as well as quantitative analyses were demonstrated.

To evaluate the possibility of using the LIBS technique to detect and quantify rare earth elements, three consecutive studies were executed. Firstly, pure oxides of six rare earth elements were studied and then real samples directly taken from natural ores were analyzed. In the third step, two rare earth elements (Eu and Yb) in aqueous solutions were studied by underwater LIBS and the pressure effect on the plasma emission is discussed.

DEDICATION

To my parents,

Mr. Mani Ram Bhatt and Mrs. Tara Devi Bhatt

My sisters,

Janaki, Shanti, Gita, and Neelam

My wife,

Chandu

My little ones,

Jasmine and Aaryan

and

My school principal,

Mr. (Late) Bhaskar Datta Bhatt

ACKNOWLEDGEMENTS

I would like to express my gratitude and thank to my Ph.D. dissertation director Dr. Jagdish P. Singh. I could not have successfully finished my Ph.D. degree without his guidance, teaching, enriching ideas, patience, and constant inspiration. I am really privileged to work on my research under his supervision. I would also like to specially thank Dr. Dustin L. McIntyre, my mentor during postgraduate fellowship at the National Energy Technology Laboratory (NETL) not only for continuous support in research, but also for giving me an opportunity to expose myself to a bigger research environment. I extend my thanks and gratitude towards my major professor and graduate coordinator, Dr. Henk F. Arnoldus, for continuous guidance and support. I want to dedicate my deepest appreciation to Dr. David L. Monts for his help as graduate coordinator from the beginning of my admission to MSU, for continuous support in writing manuscripts, and for serving as a committee member. To my other committee member Dr. Ratan Jha, I would like to express my sincere gratitude.

I also want to acknowledge Ms. Fang-Yu Yueh for her significant guidance in research and writing manuscripts. To my research group members at MSU, Mr. Bader Alfarraj, Dr. Charles Ghany, Dr. Herve Sanghapi, Mr. Ayed Binzowaimi, and Dr. Krishna K. Ayyalasomayajula, I would like to express my gratitude for important discussions and collaborations.

I am also grateful to Dr. Jinesh Jain and Dr. Christian L. Goueguel for their continuous support, discussions, and collaboration during my postgraduate fellowship at NETL.

I would like to thank all the professors, staff, and friends at Department of Physics and Astronomy and at the Institute of Clean Energy Technology (ICET), MSU for their continuous inspiration and help.

My sincere gratitude to the Oak Ridge Institute for Science and Education (ORISE) for offering me a postgraduate fellowship which gave me an opportunity to widen my professional and experimental research experience.

I want to acknowledge the MSU Department of Physics and Astronomy for providing graduate assistantship and the Institute for Clean Energy Technology (ICET) and NETL for providing all the lab facilities for my research.

TABLE OF CONTENTS

LIST OF TABLES

LIST OF FIGURES

CHAPTER I

INTRODUCTION

Spectroscopy and spectroscopic techniques have become integral parts of material science because of their usefulness in material characterization. Spectroscopy deals with the interaction of energy in the form of electromagnetic radiation with atoms and molecules of matter to obtain qualitative and quantitative information. Spectroscopy is so broad that it encompasses many sub-disciplines, depending up on the nature of interaction, type of radiation, and type of application. The interaction of electromagnetic radiation with atoms and molecules leads to absorption, emission, and scattering of radiation, which correspond to three categories of spectroscopy; absorption spectroscopy, emission spectroscopy, and scattering spectroscopy, respectively. According to the type of radiation involved, ultraviolet spectroscopy, visible spectroscopy, infrared spectroscopy, etc. are common in the scientific community.

With the advancement in science and technology, application of spectroscopy has also expanded and several spectroscopic techniques have been derived with various applications. Mass spectrometry (MS), inductively coupled plasma-optical emission spectrometry (ICP-OES), inductively coupled plasma-mass spectrometry (ICP-MS), X-ray spectroscopy (XRS), electron spectroscopy (ES), atomic absorption spectroscopy (AAS), X-ray fluorescence (XRF), laser spectroscopy, and many other popular techniques are spectroscopic techniques. Since these techniques use optical

materials/equipment to disperse and focus the radiation, they are also identified as optical spectroscopies. With the invention of lasers in early 1960s, modern spectroscopic techniques have been able to surpass most of the limitations of classical spectroscopic techniques. Many studies have become attainable which were not possible with incoherent sources of light [1]. Laser spectroscopy includes all the techniques using a laser as an excitation source to interact with the matter. Laser-induced photoionization spectroscopy, laser-induced fluorescence spectroscopy, laser optogalvanic spectroscopy, cavity ring-down laser absorption spectroscopy, and laser-induced breakdown spectroscopy are some of the laser spectroscopy techniques used for material characterization. All the analytical techniques use a wide range of principles to reveal the information about materials.

Material characterization fundamentally includes qualitative and quantitative analysis of physics and chemistry of atoms and molecules of materials. Study of the composition of materials, structure of components, abundance of the elements in the materials, and numerous other fundamental macroscopic and microscopic properties of the materials is the primary task in material science with the ultimate goal of using or preserving them for human welfare.

Despite myriad advantages of modern analytical techniques, some limitations are always associated with them. In order to make the best utilization of existing techniques, their optimization is important for better understanding of the universe and its phenomena, which gradually will open an avenue for alternative, more universal, more precise, more accurate, and faster analytical techniques.

In this research study, one of the laser-based analytical techniques, laser-induced breakdown spectroscopy (LIBS), will be discussed with its applications in various fields. Its application for qualitative and quantitative analysis will be presented with case studies of powder samples, vegetable samples, furnace blast slag samples, and solid, geological, and liquid samples containing rare-earth elements at atmospheric as well as deep ocean conditions.

1.1 Laser-Induced Breakdown Spectroscopy (LIBS)

Laser-induced breakdown spectroscopy (LIBS) is an atomic emission spectroscopy in which a laser is used as the source of radiation to interact with matter [2, 3]. It is also known as laser-induced plasma spectroscopy (LIPS) or laser spark spectroscopy (LSS). Developing LIBS as an analytical technique for qualitative and quantitative analysis of materials was initiated by a group of researchers including D.A. Cremer and L.J. Radziemski in the 1980s. For the last couple of decades, LIBS has been used in a wide range of applications and has become a robust laboratory as well as field-deployable analytical tool. Major credit goes to technological developments in the equipment (lasers, spectrometers, detectors, optical devices, etc.) used in LIBS which brought it to this level where it has been already used for a Mars mission in 2012 and again proposed for 2020 [4]. Spectrometers with improved resolution, intensified charge-coupled device (ICCD) detectors, and robust lasers, which can be administrated by software, have been introduced.

Because of LIBS versatility and because of the infeasibility of using other techniques in harsh environments, LIBS is becoming more extensively used. In principle, LIBS can analyze any matter regardless of its physical state, whether it be solid, liquid,

gas, or aerosol with no or minimal sample preparation. Compared with traditional techniques, LIBS has more advantages. It has high spatial resolution, it can be used in harsh environments like melting and burning samples with remote detection. It has broad elemental coverage, including lighter elements, such as H, Be, Li, C, N, O, Na, and Mg.

1.1.1 Principle of LIBS

When a laser pulse with sufficient irradiance is focused onto a material, a plasma is produced through rapid vaporization, dissociation, heating, and ionization of atoms of the material. This plasma has very high temperature and starts to expand and cool, during which it emits specific radiation representative of the elements present in the material. Since all the elements emit light at their characteristic frequencies (wavelengths) and hence produce unique spectral signatures, LIBS can detect all the elements. Laser-induced breakdown and spectral emissions from the plasma plume depend up on the environmental conditions and properties of the constituent species of the material [5]. The continuum and line emissions from the plasma are visualized in the form of spectra with the help of spectrograph. These spectra obtained from the test material are analyzed for both qualitative as well as quantitative analysis.

1.1.2 Mechanism of Laser-Induced Breakdown

Laser-induced breakdown of any material occurs by two mechanisms: cascade ionization or direct ionization [6-8]. In cascade ionization, there are two steps: cascade initiation through seed electrons and cascade buildup to high free electron densities. In the first step, one or more free electrons are required in the focal volume at the beginning of the pulse for initiation. In the second step, the seed electrons absorb laser photons

during collisions with molecules or ions. This process is called inverse Bremsstrahlung absorption. When a free electron gets energy surpassing the ionization potential, it ionizes bound electrons by collision and produces two free electrons. This process repeats and produces a cascade of free electrons, which causes breakdown.

The direct ionization occurs by multi-photon absorption and no seed electrons are required. Each electron is ionized by simultaneous absorption of multiple photons. There is no collision and no interaction between particles; therefore, the breakdown process is free from impurities. Multi-photon ionization is a non-linear optical process, which occurs only at high irradiances. The threshold irradiance for multi-photon ionization is higher than that of cascade ionization.

1.1.3 Spectral Emission from Laser-Induced Plasma

When the laser-induced plasma starts cooling down, it emits continuum, band, and line radiation. The continuum emission results from free-free and free-bound transitions [5, 9]. A free-free transition is a de-excitation process in which free electrons and cations interact and lose kinetic energy. Radiation produced by the deceleration of an electron due to the interaction with another charged particle is known as Bremsstrahlung radiation. A free-bound transition is a recombination process where a cation absorbs a free electron.

The emission of continuum radiation originates near the sample surface; it covers the spectral range of almost 2-600 nm. The presence of both neutral and ionic species is observed in line specta. The continuum emission from a hot plasma decays faster than does line emission. Neutral and low ionization species are observed in the outskirts of a plasma while those of high ionization are found in the center of the plasma. As the

plasma expands and cools, more atomic emission is observed than ionic emission. The time variation of spectral line intensities shows that line emission from multiply ionized species occur at the time of plasma formation while emission from singly ionized or neutral species occur after a certain time after plasma formation. The number of photons emitted per unit time and per unit volume is called emissivity of a spectral line. It is equal to the product of radiative transition probability and the emitting excited level density.

1.1.4 Plasma Characterization

The emission lines obtained from the plasma have three main features: wavelength, intensity, and intensity profile. LIBS analyses, such as identification of elements, and calculation of the concentration of elements in the material are performed by studying these features. These features depend on both the structure of the emitting atoms and their environment. Wavelengths of the spectral lines are determined by the distinct energy levels associated with each kind of atom. For LIBS experiments, it is important to understand and quantify different phenomena and parameters related to the plasma and plasma emission.

1.1.4.1 Local Thermodynamic Equilibrium

At thermodynamic equilibrium, the whole system of the plasma can be described by statistical mechanics and electrons, atoms, and ions all are characterized by the same temperature [10, 11]. The electron energy distribution function follows the Maxwellian form and the atomic state distribution function is given by Boltzmann distribution [12, 13]. According to the principle of detailed balancing, every process has its inverse process to make maintain balance at thermodynamic equilibrium [14]. When the system

does not follow this principle, it deviates from thermodynamic equilibrium and goes to a new different equilibrium. When a plasma emits photons, their energy distribution deviates from the Planck function and the balance of electrons, atoms, and ions also gets disturbed. In this situation, if the energy lost by radiation is smaller than that with other processes, the system still follows the Saha-Boltzmann and Maxwell distribution and reaches a new equilibrium known as local thermodynamic equilibrium (LTE). At LTE, the excitation temperature is equal to the temperature of the electrons, atoms, and ions. For the plasma to be in local thermodynamic equilibrium, the following criterion must be valid [15, 16].

$$n_e \geq 1.6 \times 10^{12}\, T^{1/2} (\Delta E)^3 \tag{1.1}$$

where n_e is electron number density, ΔE is energy gap of the transition lines (in eV), and T is the temperature (in K). This criterion is known as the McWhirter criterion. For reliable quantitative analysis, a plasma should be in LTE.

1.1.4.2 Optical Thickness, Self-Absorption, and Self-Reversal

When the plasma has very high density, it absorbs its own emission and causes a distortion in the emission line profile. This is known as self-absorption and the plasma is said to be optically thick. This effect is prominent in resonance lines connected with the ground state. During plasma expansion and emission, the temperature of its outer part is less than that of the center. When light passes through these colder outer parts of a plasma, a dip in the intensity line profile of emission line is observed, this effect is known as self-reversal. For accurate analysis, the emission lines to be considered should be free from these effects and for which the plasma should be optically thin. To identify whether the plasma is optically thin or not, theoretical and observed values of the intensity ratio of

resonant and non-resonant lines are compared and they should be consistent for optically thin plasmas [17-19]. The theoretical value of the intensity ratio of two lines can be obtained by using [16]

$$\frac{I_1}{I_2} = \left(\frac{\lambda_{nm,z}}{\lambda_{ki,z}}\right)\left(\frac{A_{ki,z}}{A_{nm,z}}\right)\left(\frac{g_{k,z}}{g_{n,z}}\right)exp\left(-\frac{E_{k,z}-E_{n,z}}{k_B T}\right) \quad (1.2)$$

where I_1 is the line intensity from the k-i transition and I_2 is that from the n-m transition; λ is the wavelength; A_i are the transition probabilities; g_i are the degeneracies of the energy levels; E_i the energy of the level; k_B is Boltzmann's constant; and T is the temperature.

1.1.4.3 Line Broadening

A spectral line extends over a range of wavelengths (or frequencies) and shows a certain profile. The emission profile is useful for LIBS analysis because it gives information about emitting species and their surroundings. This line profile can be broadened due to some local or external effects. Different types of line broadening are observed in plasma emission [5, 20]. Due to the finite lifetime of excited states, natural broadening takes place and the line profile is Lorentzian. Doppler broadening is observed because of the thermal motion of the emitting species and the shape of line profile is Gaussian. Stark broadening occurs due to an electric field produced by the plasma electrons and ions. Stark broadening is prominent at the early stages of the plasma when electron density is high, while as the plasma expands and cools more effect of Doppler broadening is observed in line profile [21]. Pressure broadening occurs due to collisions between neutral species at higher pressures.

1.1.4.4 Electron Density and Plasma Temperature

To estimate the electron density in a plasma, Stark broadening and Saha-Boltzmann methods are employed. For the Stark broadening profile, the relation between line width and electron density is given as [12]

$$\Delta\lambda_{FWHM} = 2[2 + 1.75 \times 10^{-4} N_e^{1/4} \alpha \left(1 - 0.068\, N_e^{1/6} T^{-1/2}\right)] \times 10^{-16} \omega N_e \quad (1.3)$$

where $\Delta\lambda_{FWHM}$ is the full-width-at-half-maximum of the transition, ω is the electron impact parameter at $N_e = 10^{16}$ cm^{-3}, α is the ion broadening parameter, and T is the temperature.

The first term in the bracket is the broadening contribution from electrons and the second term is due to ion broadening. The second term is very small and can be neglected to express Eq (1.3) as

$$\Delta\lambda_{FWHM} = 2 \times 10^{-16} \omega N_e \quad (1.4)$$

The FWHM can be calculated experimentally and ω is generally referenced from the literature to estimate the electron density.

The Saha- Boltzmann equation is given as [22, 23]

$$n_e = \frac{I_z^*}{I_{z+1}^*} 6.04 \times 10^{21} (T)^{3/2} \times exp\left[\frac{-E_{k.z+1} + E_{k,z} - \varkappa_z}{k_B T}\right] \quad cm^{-3} \quad (1.5)$$

where $I_z^* = I_z \lambda_{ki,z} / g_{k,z} A_{ki,z}$, I_z is intensity of spectral line of an element in the ionization stage z, and $\varkappa_z$ is the ionization energy of the species in the ionization stage z, E stands for energy, and T is the temperature.

To calculate the plasma temperature, the Boltzmann plot method is generally applied. The Boltzmann equation is given as [24]

$$ln\left(\frac{I_{ik}\lambda_{ik}}{g_i A_{ik}}\right) = \left(-\frac{1}{k_B T}\right) E_i + ln\left(\frac{nhc}{U(T)}\right) \quad (1.6)$$

where I is the intensity of a spectral line, λ is the wave length, g_i is the statistical weight of the upper energy level, A_{ik} is the transition probability from level i to k, E is the energy, n is the number density, U is partition function, k_B is the Boltzmann constant, and T is the temperature. When the term on the left-hand side is plotted against E_i, it yields a linear plot known as the Boltzmann plot. The slope $-1/k_BT$ is used to determine the temperature T. Spectroscopic data for spectral lines are taken from NIST Atomic Database [25].

1.1.5 LIBS Instrumentation

Instrumentation for LIBS experiments has three major components: laser, sample, and detection system. Various types of lasers ranging from UV excimer later to infrared solid state lasers are used to generate the laser-induced plasmas [26]. The main features of the lasers, such as energy, wavelength, pulse duration, operation mode, etc., have significant effects on plasma properties, which equally depend up on the quality of the sample material as well. The test sample could be in solid, liquid, or gaseous states; therefore, the sample holder is to be adjusted accordingly.

Solid samples are easiest to handle for LIBS experiments. Laboratory-based LIBS experiments can be performed on samples kept in a chamber, which could be under vacuum or filled with an inert gas or simply kept at atmospheric conditions, but field-based experiments are carried out under atmospheric environments. The detection system consists of focusing optics, spectrograph, and computer. The focusing optics includes lenses and optical fibers, while the spectrograph has dispersing elements, signal

processing electronics, camera, etc. Nowadays, photomultiplier tubes (PMT), photo diodes, or intensified charge-coupled devices (ICCD) detectors are being used in place of traditional photographic plates. Computers are used for data recording, processing, and analysis.

1.1.6 Experimental Parameters and Signal Optimization

Depending up on the application and sample properties, different types of lasers are used in LIBS experiments. Material ablation depends up on the laser irradiance and its wavelength. A relation of mass ablation rate dm/dt (kg/s cm^2) with laser irradiance (W/cm^2) and wavelength λ has been reported as [5]

$$\frac{dm}{dt} = 110 \frac{I_L^{1/3}}{10^{14}} \lambda^{-4/3} \quad (1.7)$$

This relation shows that the shorter the laser wavelength, the higher the mass ablation rate. Likewise, Mao *et.al*. have reported that a higher mass ablation rate is produced by shorter pulses (picoseconds) than by nanosecond pulses [27]. A higher mass ablation rate implies an increase in plasma density, which will absorb more laser energy and will affect the plasma emission. This fact requires the selection of favorable laser energy with a given wavelength and pulse width to obtain optimum signal with the lowest background.

When a laser-induced plasma expands, continuum emission is observed in the beginning due to Bremsstrahlung radiation, and line emission is observed at later times when the temperature decreases. Decay of continuum emission is also faster than that of line emission. Therefore, proper delay time and time width are to be selected for acquisition of line emissions. These delay time and time width should be selected to

optimize the signal-to-noise ratio (SNR) or signal-to-background (SBR) ratio for elemental analysis.

1.1.7 Double-Pulse LIBS

LIBS community has agreed that traditional LIBS (single pulse) technique has low sensitivity as one of its limitations [28, 29]. In 1984, Cremers *et al*. [30] for the first time showed the use of sequential pulses in liquids; since then, double-pulse LIBS has been continuously getting attention from many research groups. Studies are reported showing enhancement in signal intensity, lower detection limits, and more stable emission with double-pulse LIBS [31, 32]. It is assumed that material ablation and plasma volume increases with the use of consecutive laser pulses [33]. Plasmas produced by a second pulse experiences a hotter environment to expand due to the plasma produced by the first pulse. Consequently, temperature decreases slowly and hence stable signal can be obtained. People have performed experiments with various combinations of lasers with different pulse widths, wavelengths, and energies at different inter-pulse delays [34-37].

1.1.8 LIBS for Qualitative Analysis

LIBS has been widely used for qualitative analysis in the material science field. It mainly includes the identification of elements and grouping of elements in a test sample by studying LIBS spectra recorded from a sample. Multiple factors are taken into account for confirmation of the presence of elements in the sample. Wavelength positions and relative intensities of the observed spectral lines are compared with those given in references like the NIST atomic data base or previously reported results. Since different

spectral lines might have different spectroscopic properties such as ionization energy, transition probability, not all the lines may be observed all the time. It is important to record spectra with favorable experimental parameters to observe a sufficient number of lines with justified experimental repetition. Generally, neutral spectral lines are preferred compared to multiply ionized lines in case of possible interference with lines of other elements. Knowledge about the sample and its source is also very helpful for the identification of spectral lines and corresponding elements.

1.1.9 LIBS for Quantitative Analysis

For LIBS quantitative analysis, two approaches are in practice; calibration free LIBS and calibration LIBS. The calibration free method is complex and it depends on the existence of the local thermodynamic equilibrium (LTE) condition in the laser-induced plasma. Moreover, it requires the plasma to be spatially homogeneous and optically thin for accurate and precise diagnostics of plasma emission [38]. Several research groups have reported use of calibration free LIBS for quantification of different elements [39-41]. In calibration LIBS, spectra obtained from known or standard samples are used to produce statistical training models. These models are then used to predict the concentration of various elements in unknown samples. To obtain reliable quantitative results, the samples used for developing calibration models and unknown samples should be stoichiometric. Both univariate and multivariate analysis methods have been used for quantification depending up on the samples. To apply the univariate calibration method, one must be careful in selecting spectral lines; lines should be free from interference and self-absorption. Multivariate analyses are useful when the samples and spectra recorded

from them are complex. Internal standardization, normalization, etc. are generally applied in LIBS analysis to reduce the matrix effect [42-45].

Major statistical methods used for quantitative LIBS analysis include simple linear regression (SLR), multiple linear regression (MLR), principal components analysis (PCA), principal component regression (PCR) and partial least square (PLS). We will discuss briefly these methods and their working mechanisms.

1.1.9.1 Simple Linear Regression (SLR)

Simple linear regression (SLR) is a univariate statistical technique in which a dependent variable is expressed as a function of an independent variable. In LIBS, intensity or integrated intensity (area under curve) of analyte spectral lines are separately plotted as a function of known analyte concentration to develop calibration models, which are later used to predict the concentrations of elements in unknown samples. The calibration model can be expressed as a linear and first-order equation

$$y = ax + b \tag{1.8}$$

where y is the dependent variable (intensity, integrated intensity)

a is the slope of the curve

x is the independent variable (concentration of analyte), and

b is the intercept.

The predictive capacity of developed calibration models is evaluated by comparing the exact concentration of analyte and that predicted by the calibration models. The difference is termed as relative difference and calculated as

$$RD\% = \frac{|C_{LIBS} - C_{Exact}|}{C_{Exact}} \times 100\% \quad (1.9)$$

where C_{LIBS} is concentration of analyte predicted by calibration model and C_{Exact} is the exact concentration of the analyte.

1.1.9.2 Multiple Linear Regression (MLR)

Multiple linear regression simulates the relationship between two or more explanatory variables and a response variable by fitting a linear equation to observed data. For LIBS, concentration of the analyte is expressed as a linear equation

$$C = b_0 + \sum_i^n b_i A_i \quad (1.10)$$

where C is the concentration of the analyte, b_o is the intercept, b_i is the coefficient corresponding to Ai, and A_i is the intensity or integrated intensity of analyte lines.

1.1.9.3 Principal Component Regression (PCR)

PCR is a multivariate analysis (MVA) technique based on principal component analysis (PCA). PCA provides a visual representation of the relationships between samples and variables. It brings characteristic information of original variables and displays them onto a lesser number of variables known as principal components (PCs). These principal components are used as regressors to develop calibration models.

1.1.9.4 Partial Least Squares Regression (PLSR)

Partial least squares regression (PLSR) is also one of the multivariate analytical techniques used in chemometrics. It generates a regression model that correlates the two matrices; set of predictors and set of responses. The samples with known concentrations are used to construct a model correlating the two matrices, which can be later used to predict unknown concentrations of other samples.

1.1.10 LIBS Analytical Figures of Merit

Analytical figures of merits are used to assess the efficiency of analytical techniques. To evaluate the LIBS performance as an analytical technique, the limit of detection (LOD), limit of quantification (LOQ), precision, and accuracy are generally taken into consideration. According to the International Union of Pure and Applied Chemistry (IUPAC), the limit of detection (LOD) is the smallest concentration of analyte that can be detected with reasonable certainty. For LIBS analysis, it is generally calculated by the equations

$$LOD = 3\frac{C\sigma}{I} \tag{1.11}$$

and

$$LOD = 3\frac{\sigma}{S} \tag{1.12}$$

where c is the minimum concentration of analyte used in calibration, σ is the standard deviation of the background, I is the intensity of analyte spectral line used in calibration, and S is the slope of the calibration curve.

Some literatures are also found to be using a factor 2 instead of 3 in Equation (1.11) to find LODs [46, 47].

Similarly, the limit of quantification (LOQ) is considered to be the minimum amount of analyte that can be measured reliably. It is estimated by using

$$LOQ = 10\frac{\sigma}{S} \tag{1.13}$$

Accuracy is a measure of the closeness of the calculated value with its true value. In LIBS analysis, it is generally expressed as relative accuracy (RA) in percentage and is given by

$$RA\% = \left|\frac{C_{LIBS} - C_{True}}{C_{True}}\right| \times 100\% \quad (1.14)$$

where C_{LIBS} is the calculated value and C_{True} is the true or standard given value.

Precision is a measure of repeatability of the measurement. In LIBS, due to shot-to-shot fluctuations in laser pulses and heterogeneity of the samples, plasma emission and hence measurements may be affected. Standard deviation of the measurements gives a measure of reproducibility of the results.

1.2 Motivation and Objectives of the Research

LIBS consists of entirely optical equipment, requiring only optical access to the test samples. A very small amount (in the range of mg) of the sample is sufficient for LIBS analysis, which reduces the possibility of contamination. Including this, LIBS has many other advantages over traditional analytical techniques, such as minimal or no sample preparation, vary rapid measurements and analysis results, feasibility of using in harsh environments generally unattainable with other techniques, etc. Although LIBS has been widely used in various applications, still there are many areas where the possibility of using LIBS coupled with an advanced detection and analytical system has not been studied sufficiently. In this dissertation, I will present applications of the LIBS technique to develop methodologies for qualitative and quantitative analysis of various elements in different samples. The major objectives of this research work include:

1. To study the possibility of using LIBS for elemental analysis with atomic and molecular spectra.
2. To develop a LIBS technique for monitoring food materials with a case study of comparison of organic and conventional vegetables.

3. To study the application of LIBS for qualitative as well as quantitative analysis of slag samples.
4. To develop a field deployable LIBS-sensor for detection and measurement of rare earth elements in geological samples as well as in hydrothermal fluids.

1.3 Organization of the Dissertation

Studies of designing and developing optical sensing methodologies to achieve the above-mentioned objectives are discussed in this dissertation. In chapter two, qualitative and quantitative analyses of atomic and molecular spectra are discussed. Mixtures of $SrCl_2$ and Al_2O_3 in powder form are taken as working samples. The atomic emission from Sr and molecular emission from SrCl and SrO are identified in the LIBS spectra. Calibration models are developed for quantification of Sr and limits of detection for atomic and molecular LIBS are compared. This work was published in the *Applied Optics* journal.

Chapter three, which was published in the *Applied Spectroscopy* journal, is on the application of the LIBS technique to monitoring elemental nutrients in organic and conventional vegetables. Major nutrient elements are identified in cauliflower and broccoli by analyzing LIBS spectra recorded from them. It shows the possibility of developing a hand-held LIBS sensor to use in quality control of food samples.

Chapter four includes LIBS analysis of charcoal blast furnace slags. Major elements present in the slags are studied and their calibration models are developed for their quantification. Concentration of some elements is estimated by using the developed calibration models which are then compared with those obtained by ICP-OES methods. This study is accepted for publication in the journal *Applied Optics*.

In chapter five, univariate and multivariate LIBS analyses of rare earth elements in solid and liquid samples are discussed. In the first part, six rare earth elements [cerium (Ce), europium (Eu), gadolinium (Gd), neodymium (Nd), samarium (Sm), and yttrium (Y)] in standard powder forms are studied with the LIBS technique. This part was published in the *Applied Optics* journal. Study of rare earth elements in natural geological samples is discussed in the second part, which is recently accepted for the publication in the *Applied Spectroscopy* journal. In the third part, underwater LIBS of two rare earth elements is discussed. Eu and Yb in aqueous solutions are studied at atmospheric as well as deep ocean environments.

In chapter six, a summary of the research work reported in this dissertation and some future recommendations for prospective researchers are presented.

REFERENCES

[1] W. Demtröder, *Laser spectroscopy: basic concepts and instrumentation*: Springer Science & Business Media, 2013.

[2] D. A. Cremers and A. K. Knight, *Laser-Induced Breakdown Spectroscopy*: Wiley Online Library, 2006.

[3] L. J. Radziemski and D. A. Cremers, "Handbook of Laser Induced Breakdown Spectroscopy," ed: John Wiley & Sons, West Sussex, England, 2006.

[4] S. Maurice*, et al.*, "The ChemCam instrument suite on the Mars Science Laboratory (MSL) rover: Science objectives and mast unit description," *Space science reviews,* vol. 170, pp. 95-166, 2012.

[5] J. P. Singh and S. N. Thakur, *Laser-induced breakdown spectroscopy*: Elsevier, 2007.

[6] P. K. Kennedy*, et al.*, "Laser-induced breakdown in aqueous media," *Progress in Quantum Electronics,* vol. 21, pp. 155-248, 1997.

[7] P. K. Kennedy, "A first-order model for computation of laser-induced breakdown thresholds in ocular and aqueous media. I. Theory," *IEEE Journal of Quantum Electronics,* vol. 31, pp. 2241-2249, 1995.

[8] G. Bekefi, "Principles of laser plasmas," *New York, Wiley-Interscience, 1976. 712 p,* 1976.

[9] F. Anabitarte*, et al.*, "Laser-induced breakdown spectroscopy: fundamentals, applications, and challenges," *ISRN Spectroscopy,* vol. 2012, 2012.

[10] G. Cristoforetti*, et al.*, "Local thermodynamic equilibrium in laser-induced breakdown spectroscopy: beyond the McWhirter criterion," *Spectrochimica Acta Part B: Atomic Spectroscopy,* vol. 65, pp. 86-95, 2010.

[11] J. Van der Mullen, "Excitation equilibria in plasmas; a classification," *Physics Reports,* vol. 191, pp. 109-220, 1990.

[12] H. R. Griem, "Plasma spectroscopy," 1961.

[13] T. Fujimoto, *Plasma spectroscopy* vol. 123: Oxford University Press on Demand, 2004.

[14] J. Van der Mullen, "On the atomic state distribution function in inductively coupled plasmas—I. Thermodynamic equilibrium considered on the elementary

level," *Spectrochimica Acta Part B: Atomic Spectroscopy,* vol. 44, pp. 1067-1080, 1989.

[15] T. Fujimoto and R. McWhirter, "Validity criteria for local thermodynamic equilibrium in plasma spectroscopy," *Physical Review A,* vol. 42, p. 6588, 1990.

[16] M. Shah*, et al.*, "Quantitative elemental analysis of steel using calibration-free laser-induced breakdown spectroscopy," *Applied optics,* vol. 51, pp. 4612-4621, 2012.

[17] L. J. Radziemski*, et al.*, "Time-resolved laser-induced breakdown spectrometry of aerosols," *Analytical chemistry,* vol. 55, pp. 1246-1252, 1983.

[18] J. B. Simeonsson and A. W. Miziolek, "Time-resolved emission studies of ArF-laser-produced microplasmas," *Applied optics,* vol. 32, pp. 939-947, 1993.

[19] M. Sabsabi and P. Cielo, "Quantitative analysis of aluminum alloys by laser-induced breakdown spectroscopy and plasma characterization," *Applied Spectroscopy,* vol. 49, pp. 499-507, 1995.

[20] G. Gabrielse and H. Dehmelt, "Observation of inhibited spontaneous emission," *Physical review letters,* vol. 55, p. 67, 1985.

[21] O. Samek*, et al.*, "Application of laser-induced breakdown spectroscopy to in situ analysis of liquid samples," *Optical Engineering,* vol. 39, pp. 2248-2262, 2000.

[22] C. Aragón and J. A. Aguilera, "Characterization of laser induced plasmas by optical emission spectroscopy: A review of experiments and methods," *Spectrochimica Acta Part B: Atomic Spectroscopy,* vol. 63, pp. 893-916, 2008.

[23] V. Unnikrishnan*, et al.*, "Measurements of plasma temperature and electron density in laser-induced copper plasma by time-resolved spectroscopy of neutral atom and ion emissions," *Pramana J. Phys,* vol. 74, pp. 983-993, 2010.

[24] D. Devia*, et al.*, "Métodos empleados en el análisis de espectroscopia óptica de emisión: una revisión," *Ingeniería y Ciencia,* vol. 11, pp. 239-268, 2015.

[25] NIST Atomic Spectra Database [Online]. Available: https://www.nist.gov/pml/atomic-spectra-database

[26] Y.-I. Lee*, et al.*, "Recent advances in laser-induced breakdown spectrometry," *Spectroscopy,* vol. 13, pp. 14-+, 1998.

[27] X. Mao, *et al.*, "Laser ablation processes investigated using inductively coupled plasma–atomic emission spectroscopy (ICP–AES)," *Applied surface science,* vol. 127, pp. 262-268, 1998.

[28] V. Babushok, *et al.*, "Double pulse laser ablation and plasma: Laser induced breakdown spectroscopy signal enhancement," *Spectrochimica Acta Part B: Atomic Spectroscopy,* vol. 61, pp. 999-1014, 2006.

[29] C. Gautier, *et al.*, "Quantification of the intensity enhancements for the double-pulse laser-induced breakdown spectroscopy in the orthogonal beam geometry," *Spectrochimica Acta Part B: Atomic Spectroscopy,* vol. 60, pp. 265-276, 2005.

[30] D. A. Cremers, *et al.*, "Spectrochemical analysis of liquids using the laser spark," *Applied spectroscopy,* vol. 38, pp. 721-729, 1984.

[31] J. Scaffidi, *et al.*, "Emission enhancement mechanisms in dual-pulse LIBS," ed: ACS Publications, 2006.

[32] J. Pender, *et al.*, "Laser-induced breakdown spectroscopy using sequential laser pulses," vol. 15, ed: chapter, 2006.

[33] R. Noll, *et al.*, "Space-and time-resolved dynamics of plasmas generated by laser double pulses interacting with metallic samples," *Journal of Analytical Atomic Spectrometry,* vol. 19, pp. 419-428, 2004.

[34] J. Scaffidi, *et al.*, "Dual-pulse laser-induced breakdown spectroscopy with combinations of femtosecond and nanosecond laser pulses," *Applied optics,* vol. 42, pp. 6099-6106, 2003.

[35] J. Scaffidi, *et al.*, "Temporal dependence of the enhancement of material removal in femtosecond–nanosecond dual-pulse laser-induced breakdown spectroscopy," *Applied optics,* vol. 43, pp. 6492-6499, 2004.

[36] V. N. Rai, *et al.*, "Study of laser-induced breakdown emission from liquid under double-pulse excitation," *Applied optics,* vol. 42, pp. 2094-2101, 2003.

[37] P. Benedetti, *et al.*, "Effect of laser pulse energies in laser induced breakdown spectroscopy in double-pulse configuration," *Spectrochimica Acta Part B: Atomic Spectroscopy,* vol. 60, pp. 1392-1401, 2005.

[38] D. A. Cremers and L. J. Radziemski, "LIBS analytical figures of merit and calibration," *Handbook of Laser-Induced Breakdown Spectroscopy, Second Edition,* pp. 123-150, 2013.

[39] A. Ciucci*, et al.*, "New procedure for quantitative elemental analysis by laser-induced plasma spectroscopy," *Applied spectroscopy,* vol. 53, pp. 960-964, 1999.

[40] E. Tognoni*, et al.*, "A numerical study of expected accuracy and precision in calibration-free laser-induced breakdown spectroscopy in the assumption of ideal analytical plasma," *Spectrochimica Acta Part B: Atomic Spectroscopy,* vol. 62, pp. 1287-1302, 2007.

[41] F. Colao*, et al.*, "LIBS used as a diagnostic tool during the laser cleaning of ancient marble from Mediterranean areas," *Applied Physics A,* vol. 79, pp. 213-219, 2004.

[42] T. A. Labutin*, et al.*, "Comparison of the thermodynamic and correlation criteria for internal standard selection in laser-induced breakdown spectrometry," *Spectrochimica Acta Part B: Atomic Spectroscopy,* vol. 87, pp. 57-64, 2013.

[43] D. Choi*, et al.*, "Laser-induced breakdown spectroscopy (LIBS) analysis of calcium ions dissolved in water using filter paper substrates: an ideal internal standard for precision improvement," *Applied spectroscopy,* vol. 68, pp. 198-212, 2014.

[44] R. Lasheras*, et al.*, "Quantitative analysis of oxide materials by laser-induced breakdown spectroscopy with argon as an internal standard," *Spectrochimica Acta Part B: Atomic Spectroscopy,* vol. 82, pp. 65-70, 2013.

[45] S. Gornushkin*, et al.*, "Effective normalization technique for correction of matrix effects in laser-induced breakdown spectroscopy detection of magnesium in powdered samples," *Applied spectroscopy,* vol. 56, pp. 433-436, 2002.

[46] P. Fichet*, et al.*, "Quantitative elemental determination in water and oil by laser induced breakdown spectroscopy," *Analytica chimica acta,* vol. 429, pp. 269-278, 2001.

[47] M. Gondal and T. Hussain, "Determination of poisonous metals in wastewater collected from paint manufacturing plant using laser-induced breakdown spectroscopy," *Talanta,* vol. 71, pp. 73-80, 2007.

CHAPTER II

STUDY OF ATOMIC AND MOLECULAR EMISSION SPECTRA OF Sr BY LASER INDUCED BREAKDOWN SPECTROSCOPY

2.1 Abstract

Laser-Induced Breakdown Spectroscopy (LIBS) is an ideal analytical technique for *in situ* analysis of elemental composition. I have performed a comparative study of the quantitative and qualitative analysis of atomic and molecular emission from LIBS spectra. In my experiments, a mixture of $SrCl_2$ and Al_2O_3 in powder form was used as sample. The atomic emission from Sr and molecular emission from SrCl and SrO observed in LIBS spectra were analyzed. The optimum laser energies, gate delays, and gate widths for selected atomic lines and molecular bands were determined from spectra recorded at various experimental parameters. These optimum experimental conditions were used to collect calibration data and the calibration curves were used to predict the Sr concentration. Limits of detection (LODs) for selected atomic and molecular emission spectra were determined.

Most of the content in this chapter has been adapted from *Applied Optics* Volume 54, Pages 10264-10271(2015), Chet. R. Bhatt, Bader Alfarraj, Krishna K. Ayyalasomayajula, Charles Ghany, Fang Y. Yueh, and Jagdish P. Singh, "Study of atomic and molecular emission spectra of Sr by laser induced breakdown spectroscopy (LIBS)."

2.2 Introduction

LIBS has been proven to be one of the emerging techniques for elemental analysis [1-4]. Its main characteristics (such as it needs no sample preparation or minimum sample preparation, *in situ*, capability of remote material assessment) have made it vibrant in the current atomic spectroscopy field. LIBS is an atomic emission spectroscopy technique, in which highly energetic laser pulses are used to excite the sample for plasma formation. Spectral signatures of the elements present in the sample can be obtained from this plasma, which are used for qualitative and quantitative analysis. LIBS is used for the detection of impurities [5-7], standoff detection of explosives [8-10], chemical and biological detection [11, 12], nuclear material detection [13-17], geological analysis and space exploration [18, 19], diagnostics of archaeological objects [20], and metal diffusion in solar cells [21, 22]. Tripathi *et al*. reported that matrix effects have significant effect on spectral emission intensity [6]. The physical and chemical properties of the sample can affect the characteristics of elemental emission. In a sample with two elements, the change in concentration of one element can affect the emission and distribution from another element. This creates a complication in developing calibration models and adds a drawback to LIBS as an analytical technique. To overcome these deficits with matrix effect, researchers are moving forward interestingly. More research is continuing on molecular emission. Sometimes, due to feature reversals and interference of atomic lines, analysis of molecular emission may be another option to try. So, it is worthwhile to study atomic and molecular emission comparatively.

Doucet *et al.* demonstrated quantitative molecular prediction using laser-induced molecular bands along with chemometrics [23]. They also claim that molecular LIBS and

chemometrics provide a new approach for the analysis of many molecules that are not possible by atomic LIBS. A new technique proposed by Russo *et al.,* known as Laser Ablation Molecular Isotopic Spectrometry (LAMIS), uses radiative transitions from molecular species from the sample [24, 25]. Mao *et al.* reported the possibility of application of LAMIS to analyze solid samples containing Sr at normal atmospheric pressure [26]. They obtained and measured spectra of SrO and spectra of diatomic halides of strontium (SrF, SrCl, SrBr, and SrI) in laser-induced plasmas.

This study has used laser-induced molecular band emission as well as laser-induced atomic emission for qualitative and quantitative analysis and compares the results. Binary mixtures of $SrCl_2$ and Al_2O_3 were used as experimental samples; Al_2O_3 was used to make a matrix because Al lines have very less or no interference with Sr lines. Both strong and weak atomic lines of Sr were used for the analysis of atomic emission and SrCl and SrO bands were used for the analysis of molecular emission. The results obtained from atomic and molecular emission were compared for the quantification of strontium (Sr).

2.3 Experimental Details

2.3.1 Experimental Setup

The experimental setup used in this study to record spectra is as shown in Fig. 2.1. The 532-nm laser light from a frequency-doubled Q-switched Nd:YAG laser (Quantel CFR400, 20 Hz, 7-ns pulse width, 6-mm diameter, 235- mJ maximum) was focused through a 30-cm focal length quartz lens and then a right- angle prism, was used to direct the laser light onto the sample. The sample was placed on a constantly rotating platform so that laser pulse would interact with fresh sample each time. A pick-up lens (Ocean

Optics Inc. (OOI) Part No.74-UV) tilted at 45˚ with respect to the laser beam, was used to collect the emitted spectra from a laser-induced plasma. This collected spectrum was coupled into a broadband spectrometer (Andor Technology model ME5000, 200-975 nm spectral range) through a 100-µm diameter optical fiber. The spectrograph signal was integrated with a 1024x1024 intensified charge-coupled device (ICCD) detector.

The spectrograph has a digital delay generator (DDG), which controls the gate delay (GD) and gate width (GW). The DDG is activated by the trigger from the laser Q-switch output to synchronize data acquisition with the laser pulse. For data acquisition, the spectrograph was connected to a computer, and to analyze the data, Andor Technology iStar software (version 4.15) was used. Each spectrum collected was an average of ten accumulations, and each accumulation was an average of ten laser shots. Spectra of atomic emission and molecular emission are shown in Figs. 2.2 and 2.3, respectively.

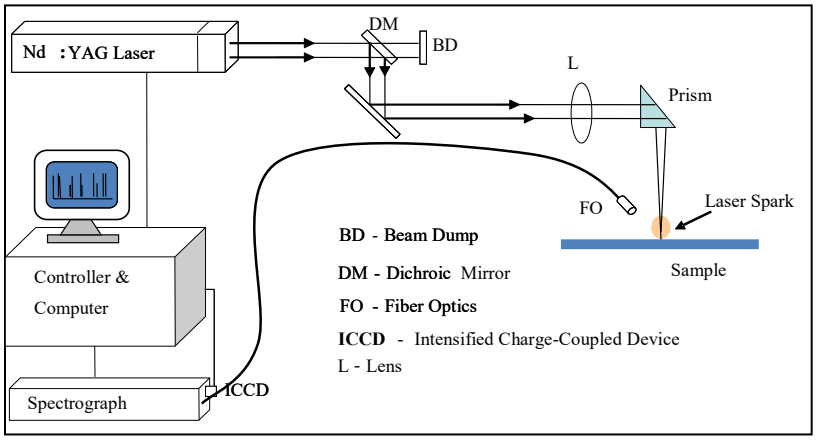

Figure 2.1 Schematic diagram of experimental set up of LIBS.

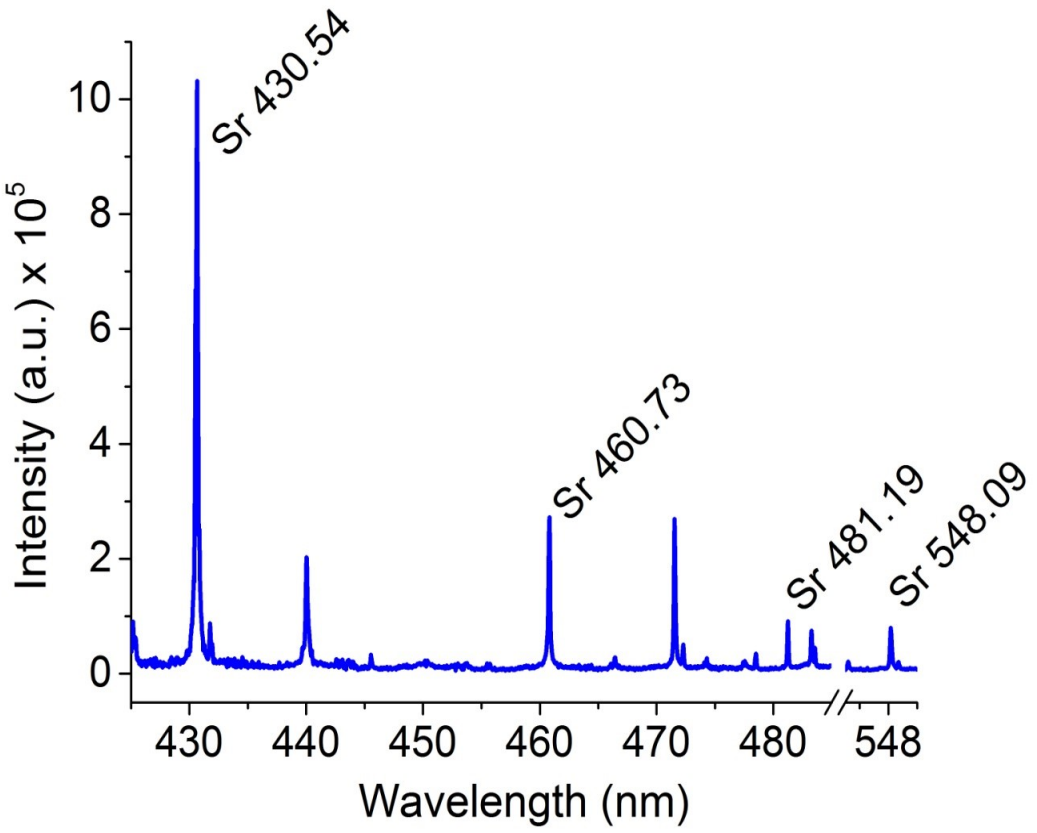

Figure 2.2 LIBS spectra of Atomic - LIBS

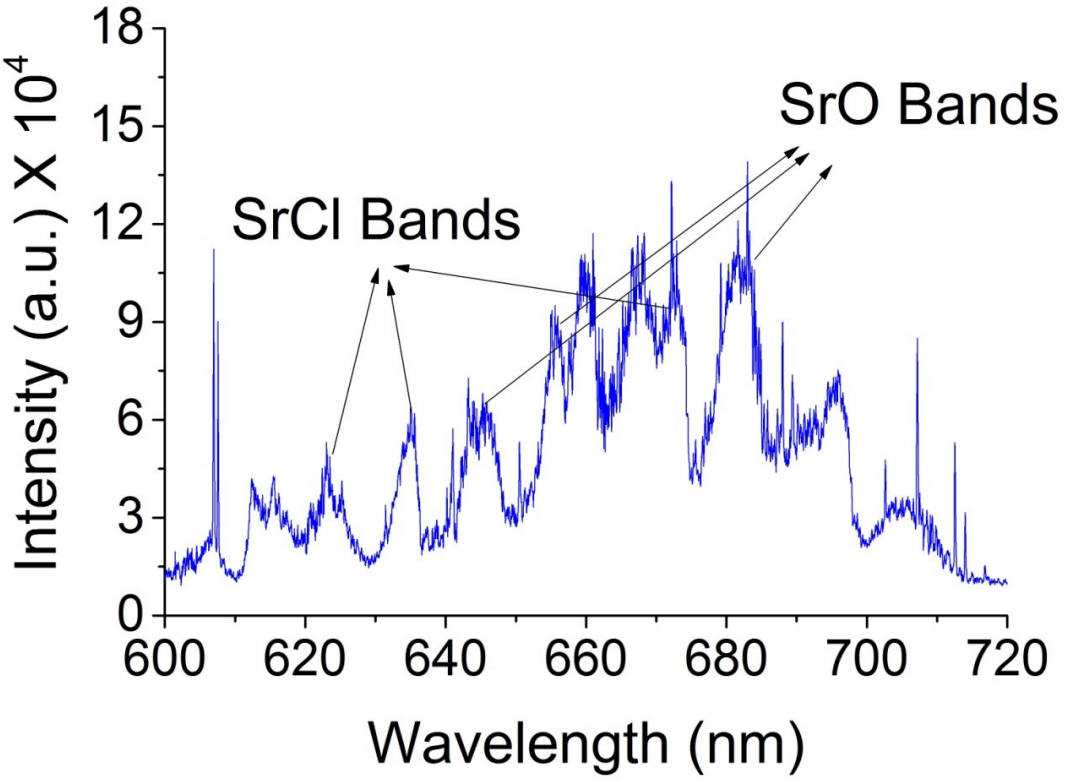

Figure 2.3 LIBS spectra of Molecular - LIBS.

2.3.2 Sample Preparation and Experimental Conditions

Experimental samples were prepared by using binary mixtures of $SrCl_2$ and Al_2O_3. The concentration of $SrCl_2$ (in weight percent (wt%), varying from 0.25% to 100%) was mixed with Al_2O_3 to make each sample's total weight to be 5 g; numerical details are given in Table 2.1. The sample was in thoroughly mixed powder form. A small amount of about 20 mg of this binary mixture was placed on a glass slide with double-sided tape on it. It was uniformly distributed on the slide by using another glass slide. The glass slide with uniformly distributed sample was placed on the rotating

platform, and the sample is interacted with the laser pulse as described above in the experimental setup.

Table 2.1 $SrCl_2$, Al_2O_3, and Sr concentrations

Sample No.	$SrCl_2$ (wt %)	$SrCl_2$ (g)	Al_2O_3 (g)	Sr %
1	0.25	0.0125	4.9875	0.14
2	0.5	0.025	4.975	0.28
3	1	0.05	4.95	0.55
4	1.5	0.075	4.925	0.83
5	2	0.1	4.9	1.1
6	2.5	0.125	4.875	1.38
7	3	0.15	4.85	1.66
8	4	0.2	4.8	2.21
9	5	0.25	4.75	2.76
10	7	0.35	4.65	3.87
11	10	0.5	4.5	5.53
12	15	0.75	4.25	8.29
13	25	1.25	3.75	13.82
14	50	2.5	2.5	27.64
15	75	3.75	1.25	41.45
16	100	5	0	55.27

To obtain the best qualitative and quantitative results, the values of experimental parameters [i.e., laser pulse energy, gate delay (GD), and gate width (GW)] were optimized. For this, several spectra were recorded at different pulse energies, gate delays (GD), and gate widths (GW) and were analyzed. The intensities of the atomic or ionic lines were prominent at lower GDs and decreased gradually with increasing GD while molecular bands were observed at higher values of GD and GW.

After analyzing many spectra at different experimental parameters, the values at which the best signal-to-noise ratio, signal-to-background ratio, reproducibility and signal optimization were obtained, were selected as optimum values. The optimum values were found to be 68-mJ pulse energy, 1-μs GD, and 5-μs GW for atomic emission and 82-mJ

pulse energy, 45-µs GD, and 45-µs GW for molecular emission. The frequency at which the laser was operated was 2.0 Hz.

2.4 Results and Discussion

A large number of spectra (more than fifty) were recorded for each sample. The spectra recorded for atomic emission with 68-mJ pulse energy, 1-µs GD, and 5-µs GW were designated as Atomic - LIBS, and those for molecular emission at 82-mJ pulse energy, 45-µs GD, and 45-µs GW were called Molecular - LIBS. Intensity and area under curve (AUC) of atomic lines and of molecular bands were taken into account for analysis and were calculated by using Andor Technology iStar software. Simple linear regression analysis (SLR) was performed on the experimental data to develop calibration models and correlation coefficient (R^2) values were determined. SLR was based on the plots of intensity and AUC of the atomic lines as a function of concentration of the analyte.

The predictive accuracy of the developed calibration model is given by the relative accuracy (RA%), which can be calculated as

$$RA\% = \frac{|C_{libs} - C_{true}|}{C_{true}} \text{ x } 100\% \quad (2.1)$$

where C_{libs} is predicted value of the concentration and C_{true} is the real value of the concentration.

The limit of detection (LOD) of Sr was calculated by using the equation

$$LOD = \frac{2\ \sigma}{I} \text{ x } C \quad (2.2)$$

where σ is the standard deviation of the background, I is the absolute peak height of the Sr analyte line or band of the lowest concentration, and C is the lowest concentration used in the calibration model.

2.4.1 Atomic - LIBS

To develop a calibration model, selection of emission lines is important. In this study, the four best emission lines of Sr (430.54, 460.73, 481.18, and 548.08 nm using NIST Atomic Database [27]), were selected for analysis. Although the Sr 407.77 and 421.55 nm lines are more intensive lines, due to self-absorption and feature reversal or inconsistency in measurements, they are not considered for calibration. The Sr 430.54 nm line is an ionized atomic line while the other Sr lines are neutral atomic lines. The stronger Sr lines (430.54 and 460.73 nm) show very good peaks in the spectra obtained from the sample of 0.14% concentration of Sr (0.25% $SrCl_2$) or higher, so 0.14% of Sr was used as minimum concentration for calibration of these lines, but for the weaker Sr lines (481.18 and 548.08 nm), the minimum concentration of Sr used was 0.28%.

So, we used spectra of 0.14, 0.55, 1.10, 1.66, and 2.21 % of Sr samples to develop calibration models for the stronger Sr lines (430.54 and 460.73 nm) while spectra of 0.28, 1.10, 2.21, 3.87, and 5.53 % of Sr samples were used to develop calibration models for the weaker Sr lines (481.18 and 548.08 nm). Calibration models were developed by plotting intensity and AUC of atomic lines versus concentration of Sr; the intensity and AUC are considered after subtracting the background. Fig.2.4 (a), (b), (c), and (d) show the calibration models of Atomic - LIBS. Probably due to the uniformity of the background, the results obtained from the models with and without subtracting the background were similar. A linear relationship of intensity and of AUC of these lines with lower values of Sr concentration was found. For higher values, both are saturated due to self-absorption. From these calibration models, we have found that the linear relation of intensity and of AUC of the stronger Sr lines (430.54 and 460.73 nm) is valid

only for lower values of Sr concentration while that of the weaker Sr lines (481.18 and 548.08 nm) is valid up to slightly higher values than the stronger Sr lines (430.54 and 460.73 nm); (detailed explanation is presented below in "Saturation Effect" section. Error bars represent the standard deviations of ten replicates in the Figures.

Also, the AUC of atomic lines was normalized with the total plasma emission (which is termed as "normalized area") and plotted as a function of concentration of Sr which was also found to be linear for lower values of concentration of Sr as shown in Figs. 2.4 (e) and (f). The R^2 values and slopes of these models are shown in Table 2.2. These calibration models obtained by using the stronger Sr lines (430.54 and 460.73 nm) were validated with a 0.83% and 1.38% of Sr sample and those obtained by using the weaker Sr lines (481.18 and 548.08 nm) were validated with 1.38% and 1.66% of Sr sample, the values of RA% were found to be less than 15% in each case as presented in Table 2.3. The values of LODs were found to be different for different lines and it is the smallest (13 ppm; parts per million) for the 430.54 nm Sr line as shown in Table 2.2.

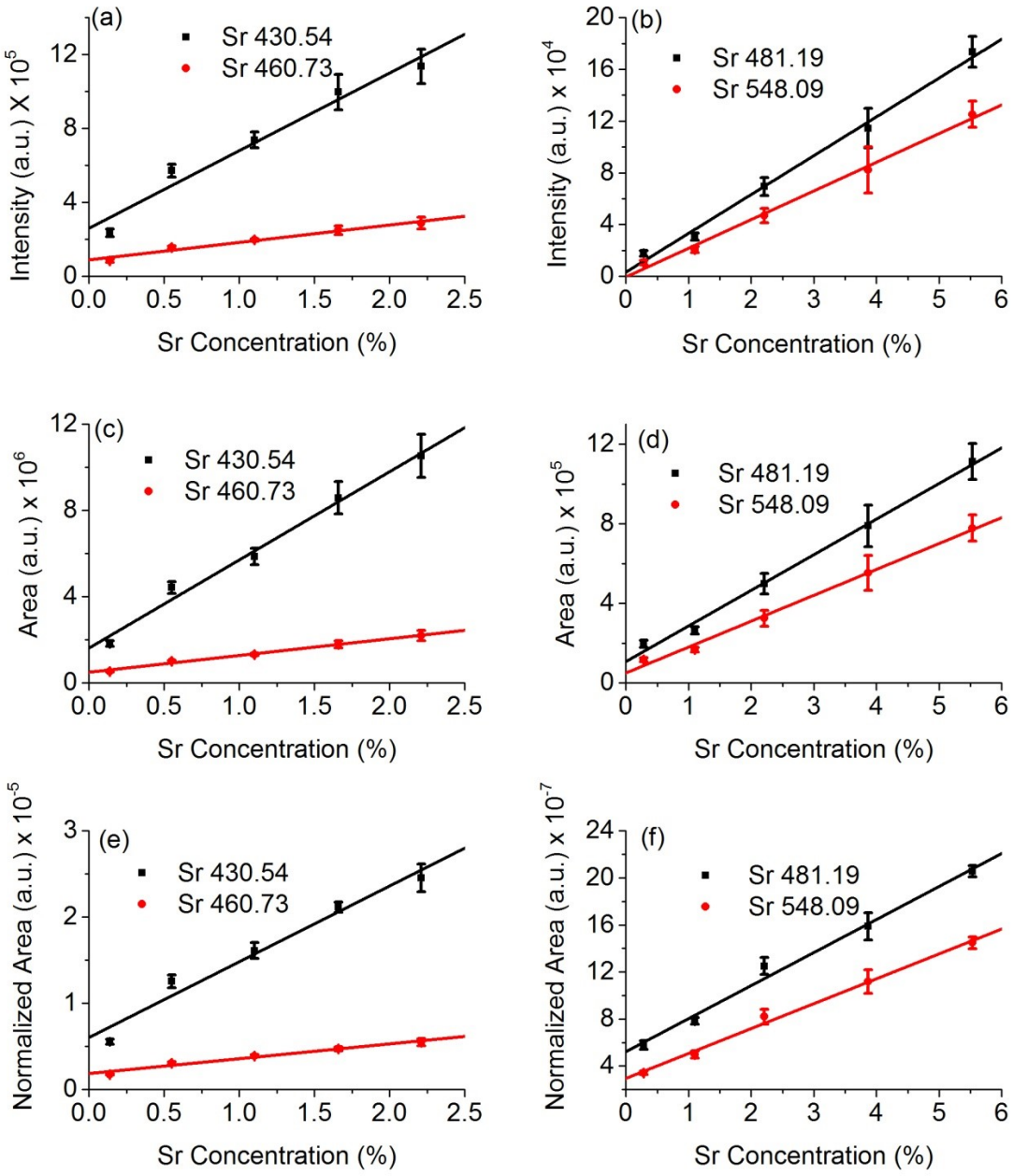

Figure 2.4 Calibration models using Sr lines: (a, b) with intensity, (c, d) with area under curve, and (e, f) with normalized area.

Table 2.2 R^2 Values and LODs

Emission Type	Considered lines or bands (nm)	Intensity vs Concentration		Area Under Curve vs Concentration		Normalized Area vs Concentration		LOD(ppm) ppm=mg/kg
		R^2 Values	Slope	R^2 Values	Slope	R^2 Values	Slope	
Atomic - LIBS	Sr 430.54	0.965	4.2E+05	0.988	4.1E+06	0.969	8.8E-06	13
	Sr 460.73	0.972	9.4E+04	0.993	7.8E+05	0.972	1.7E-06	19
	Sr 481.18	0.994	3.0E+04	0.994	1.8E+05	0.99	2.8E-07	210
	Sr 548.08	0.994	2.9E+04	0.995	1.3E+05	0.995	2.1E-07	239
Molecular-LIBS	SrCl 619-628	0.983	8.9E+02	0.998	1.2E+05	0.929	3.0E-06	347
	SrCl 630-637	0.962	1.1E+03	0.979	1.2E+05	0.993	4.3E-06	1263
	SrCl 668-675	0.984	3.2E+03	0.978	3.3E+05	0.989	1.4E-05	813
	SrO 640-650	0.977	2.2E+03	0.98	2.6E+05	0.976	1.0E-05	309
	SrO 651-662	0.971	3.3E+03	0.971	4.1E+05	0.988	1.7E-05	307
	SrO 676-685	0.991	2.8E+03	0.99	3.5E+05	0.967	1.4E-05	317
	653-675	0.989	3.5E+03	0.979	1.1E+06	0.986	4.5E-05	253

2.4.2 Molecular - LIBS

For the study of Molecular - LIBS, SrCl bands and SrO bands were considered. Three small spectral regions were selected for each band. For the SrCl bands, the first spectral region ranges from 619 nm to 628 nm with band center at 623 nm, the second region ranges from 630 nm to 637 nm with band center at 635 nm, and the third region ranges from 668 nm to 675 nm with band center at 672 nm [26]. For the SrO bands, the first region is from 640 nm to 650 nm with band center at 646 nm, the second region is from 651 nm to 662 nm with band center at 660 nm, and the third region ranges from 676 nm to 685 nm with the band center at 681 nm [26]. In addition, we considered one more band which consists of a region of both SrCl and SrO bands ranging from 653nm to 675nm, which we call the "overlapping band".

Table 2.3 Prediction results and relative accuracy (RA%)

Emission Type	Considered lines or bands (nm)	Exact Value of Sr%	Used Calibration Model					
			Intensity vs Concentration		Area Under Curve vs Concentration		Normalized Area vs Concentration	
			Predicted Value of Sr%	RA%	Predicted Value of Sr%	RA%	Predicted Value of Sr%	RA%
Atomic - LIBS	Sr 430.54	0.83	0.88	6.02	0.8	3.61	0.94	13.2
	Sr 460.73	0.83	0.78	6.02	0.72	13.2	0.84	1.2
	Sr 430.54	1.38	1.42	2.9	1.34	2.9	1.39	0.72
	Sr 460.73	1.38	1.4	1.45	1.32	4.35	1.37	0.72
	Sr 481.18	1.38	1.28	7.25	1.48	7.25	1.24	10.1
	Sr 548.08	1.38	1.2	13.04	1.5	8.7	1.28	7.25
	Sr 481.19	1.66	1.63	1.81	1.55	6.63	1.78	7.23
	Sr 548.09	1.66	1.51	9.04	1.42	14.4	1.57	5.42
Molecular - LIBS	SrCl 619-628	2.21	2.14	3.17	2.02	8.6	2.2	0.45
	SrCl 630-	2.21	2.2	0.45	2.13	3.62	2.33	5.43
	SrCl 668-	2.21	2.41	9.05	2.32	4.98	2.42	9.5
	SrO 640-650	2.21	2.23	0.9	2.25	1.81	2.38	7.69
	SrO 651-662	2.21	2.2	0.45	2.22	0.45	2.33	5.43
	SrO 676-685	2.21	2.3	4.07	2.31	4.52	2.27	2.71
	653-675	2.21	2.22	0.45	2.29	3.62	1.98	10.4

Calibration models were developed by plotting intensity, AUC and normalized area under the bands versus concentration of Sr. As for Atomic - LIBS, intensity and AUC are considered after subtracting the background. The molecular bands were easily observed only in the spectra obtained from the sample with Sr concentration 0.55% (1% $SrCl_2$) or higher, which is expected as a primary reason of the higher values of LODs of Molecular-LIBS than those of Atomic - LIBS. Figs. 2.5(a), (b), and (c) show the calibration models based on intensity. Figs. 2.5(d), (e), and (f) show those based on AUC and Figs. 2.5 (g), (h), and (i) show those based on normalized area. Error bars represent the standard deviations of ten replicates. The linear relation of intensity, AUC, and normalized area with concentration of Sr was found up to a certain value of

concentration, which is discussed below in the section "Saturation Effect". The obtained R^2 values and slopes are shown in Table 2.2. Spectra from 0.55, 1.66, 2.76, 3.87, and 5.53% Sr were used to develop the calibration models, which were validated with a 2.21% of Sr sample. By using each calibration model, RA% was found to be less than 15%. Prediction results and RA% are presented in Table 2.3. The values of LODs obtained by using different bands are presented in Table 2.2.

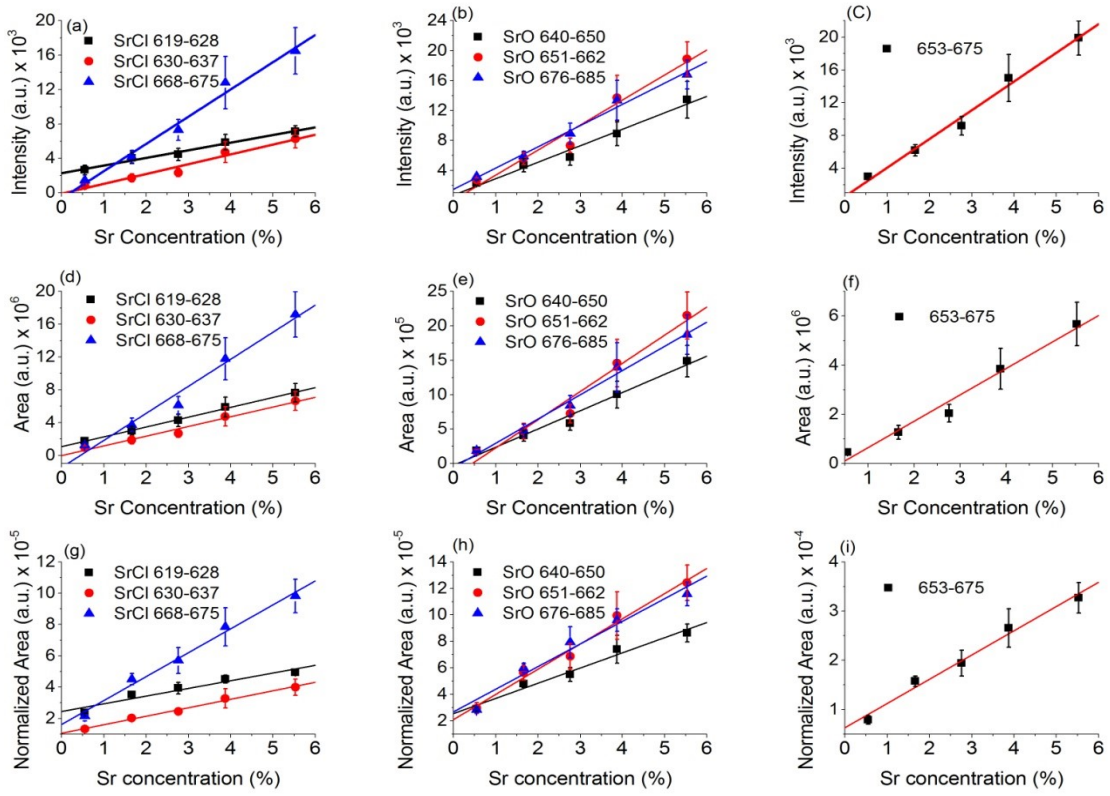

Figure 2.5 Calibration models using SrCl and SrO bands: (a, b, c) with intensity, (d, e, f) with area under curve, and (g, h, i) with normalized area.

2.4.3 Saturation Effect

In case of Atomic - LIBS, the study shows that strong and weak Sr lines demonstrate different behavior with the variation of concentration of Sr. All the calibration models discussed above get saturated after certain values of Sr concentration (saturation trend continues up to 55.27% Sr (100% $SrCl_2$), however, in order to show the deviation point clearly, graphs are not shown up to 55.27% Sr (100% $SrCl_2$) in Figs 2.6 and 2.7). The 430.54 and 460.73 nm Sr lines show a linear relationship of intensity, AUC, and normalized area with Sr concentration for only the lower values of Sr concentration. For concentration values higher than 2.76% Sr, the intensity, AUC, and normalized area are all saturated as shown in Fig. 2.6(a), (b), and (c), respectively. The Sr 481.18 and 548.08 nm lines also show a linear relationship of intensity, AUC, and normalized area with Sr concentration; the linearity is very good up to the concentration of 5.53% Sr and above 5.53% Sr, the relationship deviates slightly and is saturated for higher concentrations as shown in Fig. 2.6(d), (e), and (f), respectively. Self-absorption is the main reason of saturation of these analyte lines at higher concentration of Sr.

The Sr 430.54 and 460.73 nm atomic lines are stronger than the Sr 481.18 and 548.08 nm atomic lines. I used 0.14% Sr concentration as the minimum concentration for the calibration of Sr 430.54 and 460.73 nm lines while I used 0.28% Sr concentration as that for Sr 430.54 and 460.73 nm lines. Consequently, the values of the LODs are smaller (better) for the Sr 430.54 and 460.73 nm lines than for the 481.18 and 548.08 nm lines.

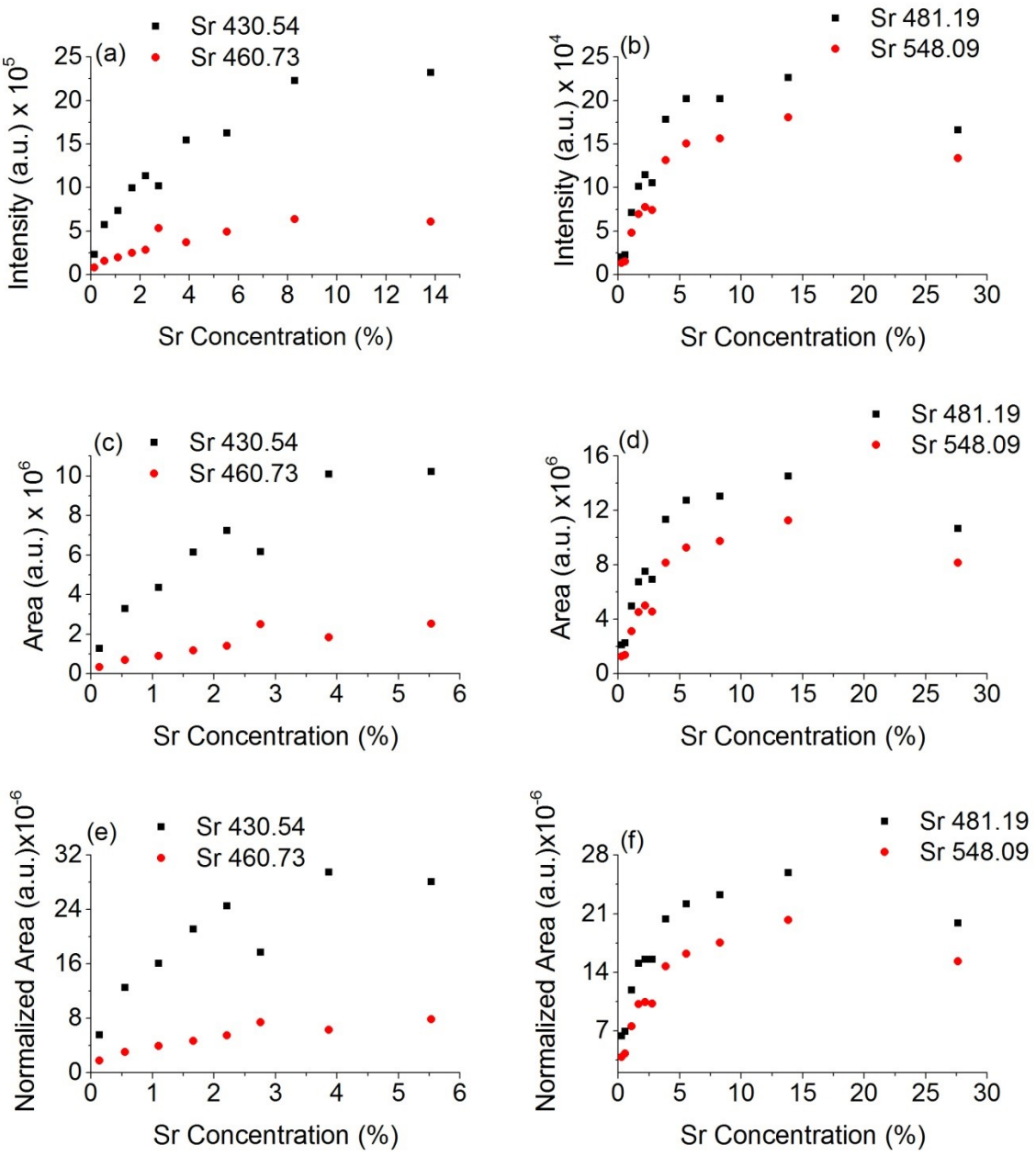

Figure 2.6 Graphs showing saturation effect at higher concentration using Sr lines: (a, b) with intensity, (c, d) with area under curve, and (e, f) with normalized area.

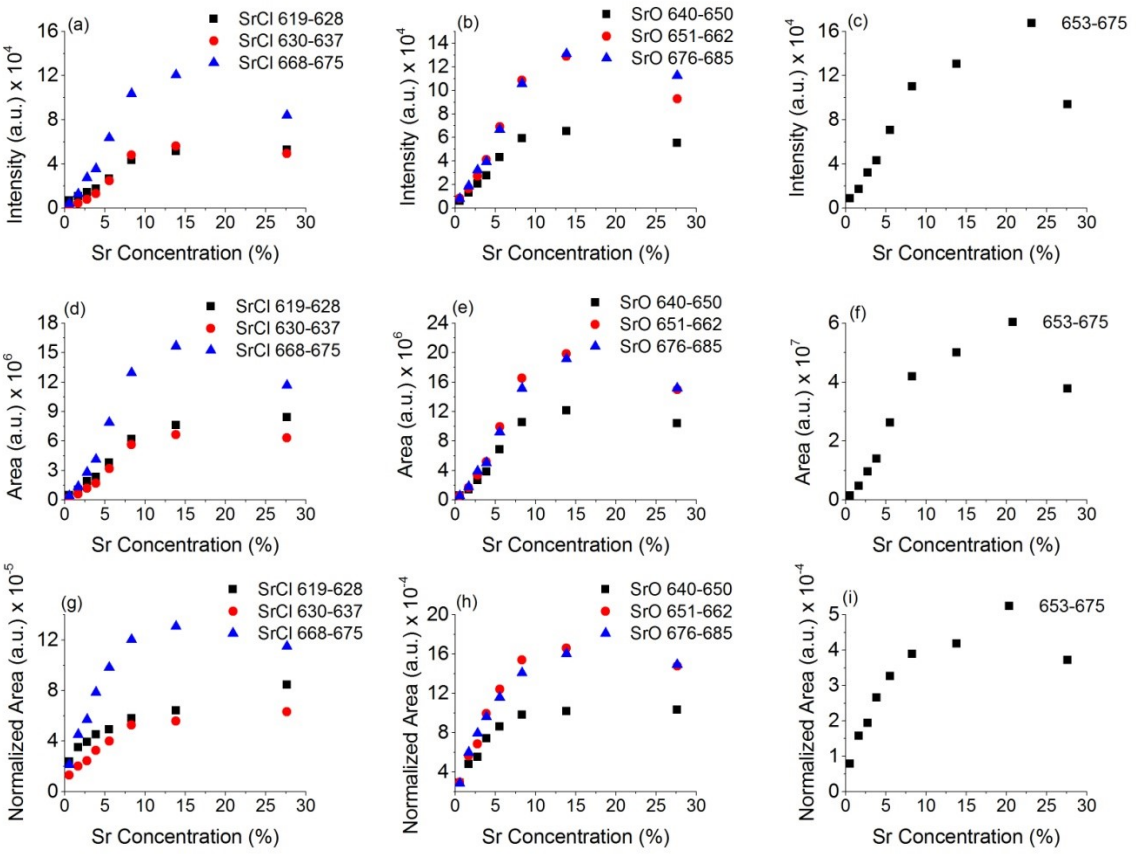

Figure 2.7 Graphs showing saturation effect at higher concentration using SrCl and SrO bands: (a, b, c) with intensity, (d, e, f) with area under curve, and (g, h, i) with normalized area.

For Molecular–LIBS, it is found that the intensity, AUC, and normalized area of all the SrCl and SrO bands considered have a linear relationship with Sr concentration up to 8.29% of Sr (15% of $SrCl_2$) and for higher concentrations due to the self-absorption they get saturated as shown in Fig.2.7(a), (b), (c), (d), (e), (f), (g), (h), and (i). Both the SrCl and SrO bands were calibrated only for 0.55% Sr and higher concentrations; consequentially, the values of the LOD for these molecular bands are found to be higher (worse) than those of the atomic lines.

2.5 Conclusions

Atomic emission and molecular emission were compared quantitatively and qualitatively by using spectra obtained from a binary mixture of $SrCl_2$ and Al_2O_3. For the analysis of atomic emission (Atomic - LIBS), four Sr lines (430.54, 460.73, 481.18, and 548.08 nm) were used to develop calibration models, while to analyze the molecular emission (Molecular - LIBS), SrCl bands and SrO bands were selected to develop calibration models. These calibration models were used to predict the concentration of Sr and different calibration models showed different prediction results and RA% for different atomic lines and molecular bands, RA% ranging from 0.4 to 15%. Based on the results discussed in the section 'Saturation Effect', the calibration models for Atomic - LIBS obtained by using the Sr 430.54 and 460.73 nm atomic lines are useful for only lower concentrations of Sr (less than 2.76% Sr or 5% $SrCl_2$) while the calibration models obtained by using the Sr 481.18 and 548.08 nm lines can be used for the Sr concentrations up to 5.53% Sr (10% $SrCl_2$). For Molecular - LIBS, the calibration models are useful for the Sr concentrations up to 8.29 % (15% $SrCl_2$). The values of LODs obtained by using Sr 430.54 and 460.73 nm lines have lower (better) values than those from the other atomic lines and molecular bands. So, in general, all the atomic lines and molecular bands (considered above) have different LODs and different prediction accuracy; hence, calibration models based on properly selected atomic lines, molecular bands, or combination of few atomic lines and molecular bands are recommended for better accuracy of Sr analysis, depending upon the expected Sr concentration.

REFERENCES

[1] A. W. Miziolek*, et al.*, *Laser induced breakdown spectroscopy*: Cambridge University Press, 2006.

[2] J. P. Singh and S. N. Thakur, *Laser-induced breakdown spectroscopy*: Elsevier, 2007.

[3] L. J. Radziemski and D. A. Cremers, "Handbook of laser induced breakdown spectroscopy," *John Wiley & Sons,* vol. 1, pp. 1-4, 2006.

[4] W. B. Lee*, et al.*, "Recent applications of laser-induced breakdown spectrometry: a review of material approaches," *Applied Spectroscopy Reviews,* vol. 39, pp. 27-97, 2004.

[5] K. K. Ayyalasomayajula*, et al.*, "Determination of elemental impurities in plastic calibration standards using laser-induced breakdown spectroscopy," *Applied optics,* vol. 51, pp. B143-B148, 2012.

[6] M. M. Tripathi*, et al.*, "An optical sensor for multi-species impurity monitoring in hydrogen fuel," *Sensors and Actuators B: Chemical,* vol. 171, pp. 416-422, 2012.

[7] S. T. Järvinen*, et al.*, "Detection of Ni, Pb and Zn in water using electrodynamic single-particle levitation and laser-induced breakdown spectroscopy," *Spectrochimica Acta Part B: Atomic Spectroscopy,* vol. 99, pp. 9-14, 2014.

[8] S. Palanco*, et al.*, "Design, construction and assessment of a field-deployable laser-induced breakdown spectrometer for remote elemental sensing," *Spectrochimica Acta Part B: Atomic Spectroscopy,* vol. 61, pp. 88-95, 2006.

[9] R. González*, et al.*, "Standoff LIBS detection of explosive residues behind a barrier," *Journal of Analytical Atomic Spectrometry,* vol. 24, pp. 1123-1126, 2009.

[10] P. Lucena*, et al.*, "Location and detection of explosive-contaminated human fingerprints on distant targets using standoff laser-induced breakdown spectroscopy," *Spectrochimica Acta Part B: Atomic Spectroscopy,* vol. 85, pp. 71-77, 2013.

[11] J. L. Gottfried*, et al.*, "Standoff detection of chemical and biological threats using laser-induced breakdown spectroscopy," *Applied spectroscopy,* vol. 62, pp. 353-363, 2008.

[12] J. L. Gottfried, "Discrimination of biological and chemical threat simulants in residue mixtures on multiple substrates," *Analytical and bioanalytical chemistry,* vol. 400, pp. 3289-3301, 2011.

[13] Y.-S. Kim, *et al.*, "Determination of uranium concentration in an ore sample using laser-induced breakdown spectroscopy," *Spectrochimica Acta Part B: Atomic Spectroscopy,* vol. 74, pp. 190-193, 2012.

[14] R. C. Chinni, *et al.*, "Detection of uranium using laser-induced breakdown spectroscopy," *Applied spectroscopy,* vol. 63, pp. 1238-1250, 2009.

[15] F. R. Doucet, *et al.*, "Determination of isotope ratios using laser-induced breakdown spectroscopy in ambient air at atmospheric pressure for nuclear forensics," *Journal of Analytical Atomic Spectrometry,* vol. 26, pp. 536-541, 2011.

[16] M. Z. Martin, *et al.*, "Exploring laser-induced breakdown spectroscopy for nuclear materials analysis and in-situ applications," *Spectrochimica Acta Part B: Atomic Spectroscopy,* vol. 74, pp. 177-183, 2012.

[17] E. J. Judge, *et al.*, "Laser-induced breakdown spectroscopy measurements of uranium and thorium powders and uranium ore," *Spectrochimica Acta Part B: Atomic Spectroscopy,* vol. 83, pp. 28-36, 2013.

[18] R. S. Harmon, *et al.*, "Applications of laser-induced breakdown spectroscopy for geochemical and environmental analysis: A comprehensive review," *Spectrochimica Acta Part B: Atomic Spectroscopy,* vol. 87, pp. 11-26, 2013.

[19] P.-Y. Meslin, *et al.*, "Soil diversity and hydration as observed by ChemCam at Gale Crater, Mars," *Science,* vol. 341, p. 1238670, 2013.

[20] I. Gaona, *et al.*, "Evaluating the use of standoff LIBS in architectural heritage: surveying the Cathedral of Málaga," *Journal of Analytical Atomic Spectrometry,* vol. 28, pp. 810-820, 2013.

[21] D. Diego-Vallejo, *et al.*, "Selective ablation of Copper-Indium-Diselenide solar cells monitored by laser-induced breakdown spectroscopy and classification methods," *Spectrochimica Acta Part B: Atomic Spectroscopy,* vol. 87, pp. 92-99, 2013.

[22] C. K. Kim, *et al.*, "Influence of laser wavelength on the laser induced breakdown spectroscopy measurement of thin CuIn 1− x Ga x Se 2 solar cell films," *Spectrochimica Acta Part B: Atomic Spectroscopy,* vol. 88, pp. 20-25, 2013.

[23] F. R. Doucet, *et al.*, "Quantitative molecular analysis with molecular bands emission using laser-induced breakdown spectroscopy and chemometrics," *Journal of Analytical Atomic Spectrometry,* vol. 23, pp. 694-701, 2008.

[24] R. E. Russo*, et al.*, "Laser ablation molecular isotopic spectrometry," *Spectrochimica Acta Part B: Atomic Spectroscopy,* vol. 66, pp. 99-104, 2011.

[25] X. Mao*, et al.*, "Laser ablation molecular isotopic spectrometry: parameter influence on boron isotope measurements," *Spectrochimica Acta Part B: Atomic Spectroscopy,* vol. 66, pp. 604-609, 2011.

[26] X. Mao*, et al.*, "Laser ablation molecular isotopic spectrometry: strontium and its isotopes," *Spectrochimica Acta Part B: Atomic Spectroscopy,* vol. 66, pp. 767-775, 2011.

[27] NIST Atomic Spectra Database [Online]. Available: https://www.nist.gov/pml/atomic-spectra-database

CHAPTER III

COMPARATIVE STUDY OF ELEMENTAL NUTRIENTS IN ORGANIC AND CONVENTIONAL VEGETABLES BY LASER-INDUCED BREAKDOWN SPECTROSCOPY.

3.1 Abstract

In this study, the laser-induced breakdown spectroscopy (LIBS) technique was used to identify and compare the presence of major nutrient elements in organic and conventional vegetables. Different parts of cauliflowers and broccolis were used as working samples. LIBS spectra from these samples were acquired at optimum values of laser energy, gate delay, and gate width. Both univariate and multivariate analysis were performed for the comparison of these organic and conventional vegetable flowers. Principal component analysis (PCA) was taken into account for multivariate analysis while for univariate analysis, the intensity of selected atomic lines of different elements and their intensity ratio with some reference lines of organic cauliflower and broccoli samples were compared with those of conventional ones. In addition, different parts of the cauliflower and broccoli were compared in terms of intensity and intensity ratio of elemental lines.

Most of the content in this chapter has been adapted from *Applied Spectroscopy*, Volume 71, Pages 686-698 (2017), Chet R. Bhatt, Bader Alfarraj, Charles T. Ghany, Fang Y. Yueh, and Jagdish P. Singh, "Comparative Study of Elemental Nutrients in Organic and Conventional Vegetables Using Laser-Induced Breakdown Spectroscopy (LIBS)."

3.2 Introduction

Vegetables and fruits are precious gifts from nature, which contain numerous nutritional elements. The determination of these elements in plant vegetables and fruits is very important to evaluate their nutritional status. Based on nutritional status of crops, their economical business value and consumption is determined. In this modern competitive market, different techniques are used to increase production; farmers commonly use different pesticides and fertilizers. Question arises: whether these artificial techniques used to produce crops change their nutritional status or not. In the United States, the National Organic Program (NOP), administered by the United States Department of Agriculture (USDA), develops the rules and regulations for organic production. Consumers believe that organic foods contain more nutrients than conventionally grown foods. However, Swedish surveys showed that there is a discrepancy between attitudes and behavior of people regarding organic foods [1]. People are positive towards organic foods, but often do not purchase them. Typically, organic foods cost 10 to 40% more than conventionally grown foods [2]. Many factors are playing roles to make the price higher, such as higher labor costs, lower productivity, etc. Traditional concepts have guided people to believe that organic foods have greater amount of nutrients, but research studies have shown mixed results. Some studies have shown that there is lower nitrate level in organically grown vegetables and no significant difference in minerals and vitamin B levels of organic and conventional cereals, vegetables or potatoes [3]. Higher vitamin C levels were found in organic vegetables, particularly for leafy ones, than in conventional ones. When literatures about organically and conventionally grown foods are reviewed, various results are found [4-9]. Based on a

systematic review of 55 studies of satisfactory quality, Dangour *et al*. claimed that conventionally grown foods had higher content of nitrogen, and organically produced foods had higher content of phosphorus and higher titratable acidity [10]. They mentioned there is no difference in the quality of nutrients between organic and conventional foods; slight differences in concentration of nutrient are because of the differences in production methods. Different techniques are used to identify the elements present in crops, vegetables, and fruits. Major techniques include inductively coupled plasma-optical emission spectrometry (ICP-OES), mass spectrometry (MS), laser-induced breakdown spectroscopy (LIBS), etc. During recent years, LIBS has gained significant popularity as one of the more powerful sensor technologies for laboratory and field use [11]. High-energy laser beams are focused on the material to be studied, which produces plasma plumes due to rapid vaporization of the material. Since all elements emit light of characteristic frequencies when excited, the LIBS technique can detect all elements present in the sample material irrespective of its physical state, whether it is in solid, liquid, or gaseous state. LIBS is an *in situ* technique which needs minimal or no sample preparation. A portable spectrometer with high resolution and the capability of standoff detection has made LIBS more attractive [12]. LIBS is applied for qualitative and quantitative elemental analysis in the fields of space exploration, environmental sciences, and cultural heritages [13]. In dentistry, LIBS is combined with pattern recognition algorithms for dental caries identification [14]. For biological study, LIBS has proven itself as useful technique [15-19]. In my previous work, LIBS was used to compare atomic and molecular spectra of Sr [20]. Trevizan *et al*. evaluated LIBS for the determination of micronutrients and macronutrients in plant materials [21, 22]. They

claimed that the outcome of LIBS analysis of plant samples was buttressed by the results given by ICP-OES after wet acid decomposition. Hussain *et al*. measured nutrients in soil; and predicted the concentration of Ca, K, P, Mg, Fe, S, Ni and Ba [23]. When ICP-OES and MS were used to analyze elements present in organically and conventionally grown wheat, barley, faba bean, and potato, no significant difference in content of the main plant nutrients was found between organic and conventional crops [24].

Cauliflowers and broccolis are widely used vegetables. As they can be consumed with and without cooking, they are considered as popular vegetables. In this study, we have used the laser-induced breakdown spectroscopy (LIBS) technique to identify the elemental nutrients present in both cauliflower and broccoli. Cauliflower and broccoli were obtained from a local grocery store. Experiment was performed for twenty - one weeks from August to December 2015. Each week new pieces of cauliflower and broccoli were used to prepare samples. Top and stem parts were separately used to obtain spectra. Spectral signatures of different elements were analyzed quantitatively to evaluate the difference between organic and conventional cauliflowers and broccolis.

3.3 Experimental Details

3.3.1 Experimental Set Up

A frequency-doubled Q-switched Nd:YAG laser (Quantel CFR400, 20 Hz, 7-ns pulse width, 6-mm diameter, 235- mJ maximum) was used as a source of light from which 532-nm laser pulses were focused onto samples through a 30-cm focal length quartz lens and then a right-angle prism. As the platform on which the sample was placed was uniformly rotated, laser light hit on fresh sample material each time. The emission spectra from the plasma formed by the interaction of laser light with sample were

collected by using a pick-up lens and were coupled into a broadband spectrometer (Andor Technology model ME5000, 200-975 nm spectral range) through a 100-µm diameter optical fiber. The spectrograph signal was integrated with a 1024x1024 intensified charge-coupled device (ICCD) detector. The spectrograph had a digital delay generator (DDG), which was activated by the trigger from the laser Q-switch output to synchronize data acquisition with the laser pulse. The DDG controlled the gate delay (GD) and gate width (GW). The spectrograph was connected to a computer for data acquisition. Each spectrum collected was an average of ten accumulations, and each accumulation was an average of ten laser shots. Andor Technology iStar software (version 4.15) was used for data analysis. A schematic diagram of the experimental set up is as shown in Figure 3.1.

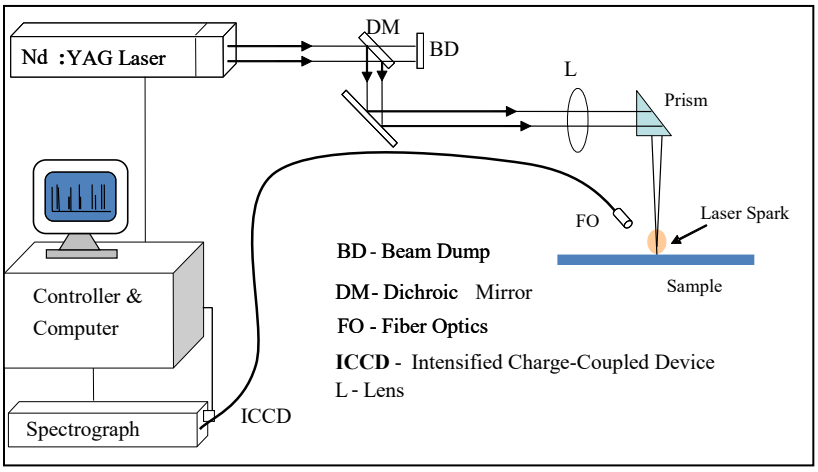

Figure 3.1 Schematic diagram of experimental set up of LIBS.

3.3.2 Sample Preparation

Top and stem parts of cleaned organic and conventional cauliflower as well as broccoli were separated. Top and stem parts are shown in Figure 3.2. These top and stem

parts were separately ground finely using a normal mortar and pestle to make a homogeneous paste. About 300 mg of this paste of top and stem parts of both organic and conventional cauliflowers as well as broccolis was uniformly distributed on separate glass slides. These slides were kept at room temperature until the paste dried completely. Generally, it took three to four days to get them dried. All the samples were dried for almost equal time before using them to collect spectra. The glass slide with dried sample was placed on the rotating platform, and the sample interacted with the laser pulse to produce spectra.

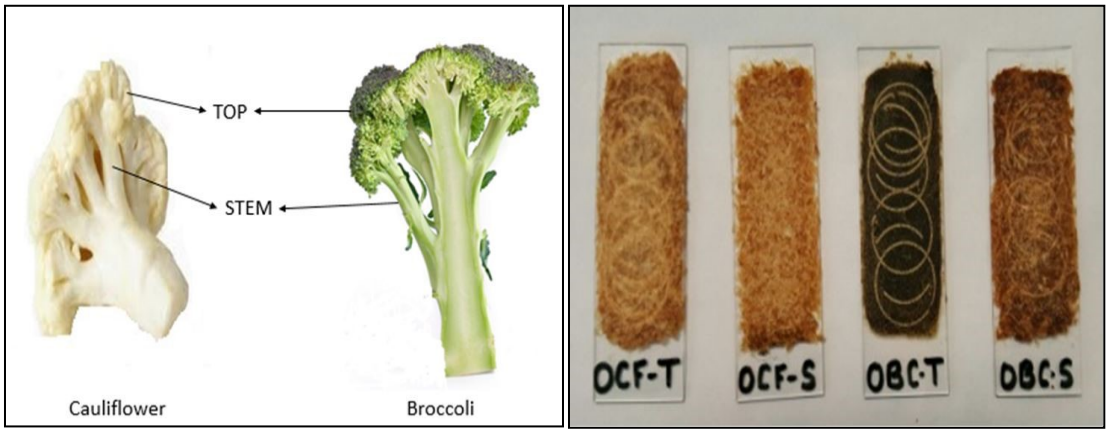

Figure 3.2 Left: Top part and Stem part of cauliflower and broccoli. Right: Samples on glass slides

3.3.3 Experimental Conditions

Several spectra were recorded from top (and stem) parts of organic and conventional cauliflower (and broccoli) samples at different values of gate delay (GD), gate width (GW), and laser pulse energy. These parameters were optimized by considering the signal-to-noise ratio. Optimum values obtained were 1-µs GD, 5-µs GW,

and 96- mJ laser energy. These optimum values were used to record the spectra from these vegetables and the laser was operated at a frequency of 2.0 Hz.

3.4 Theoretical Description

3.4.1 Population Distribution and Spectral Line Intensity

At thermodynamic equilibrium, the population distribution N_i (E_i) of the i-th energy level is given by the Boltzmann distribution as [25]

$$N_i = \frac{Ng_i}{U(T)} \exp\left(-\frac{E_i}{kT}\right) \tag{3.1}$$

where g_i is the statistical weight, T is the average temperature of the atoms/ions in the i-th energy state, N is total density of all levels sum, and U(T) is partition function given as

$$U(T) = \sum_i g_i \exp\left(-\frac{E_i}{kT}\right) \tag{3.2}$$

and spectral line intensity is expressed as

$$I_{ik} = \frac{NhcA_{ik}g_i}{U(T)\lambda_{ik}} exp\left(-\frac{E_i}{kT}\right) \tag{3.3}$$

where A_{ij} is the transition probability from level i to k, and the rest of the symbols have their usual meanings.

3.4.2 Criterion for Local Thermodynamic Equilibrium (LTE) Plasma

At local thermodynamic equilibrium (LTE) [26],

$$T_{exc} = T_e = T_i \tag{3.4}$$

where T_{exc} is the excitation temperature, T_e and T_i are the temperatures of atoms and ions.

LTE condition is generally checked by McWhirter criterion given as [26]

$$n_e \geq 1.6 \times 10^{12}\, T^{1/2} (\Delta E)^3 \quad (3.5)$$

where n_e is electron number density, ΔE is energy gap of the transition lines (in eV), and T is the temperature (in K).

3.5 Results and Discussion

3.5.1 Detection of Spectral Lines

We recorded several spectra from both top and stem parts of cauliflower and broccoli. The structure of these spectra obtained from top and stem parts of both cauliflower as well as broccoli were almost similar as shown in Figure 3.3, which probably indicates that more or less the same elements are present in both top and stem parts of cauliflower as well as broccoli. However, as their intensities were not the same, their concentrations may vary.

With the help of the NIST Atomic Data base [27], the atomic lines of elements Ca, Mg, K, Na, and Fe were identified. The emission lines Ca I 422.67 nm, Ca II 393.36 nm, Ca II 396.84 nm, Mg I 285.21 nm, Mg II 279.55 nm, Mg II 280.27 nm, K I 404.72 nm, K I 766.48 nm, K I 769.89 nm, Na I 588.99 nm, Na I 589.59 nm, Fe I 373.71 nm, Fe I 438.35 nm and many other lines of these elements were observed in the spectra obtained from top and stem parts of both cauliflowers and broccoli as shown in Figure 3.4. This identification of different atomic lines confirms the presence of the elements Ca, Mg, K, Na, and Fe in cauliflower and broccoli.

The producer or seller has listed the presence of Ca, Na, and Fe on the label, but not that of Mg and K. So, LIBS technique has shown its potentiality to detect the presence of the elements like Mg and K, which are not labeled for these vegetable flowers.

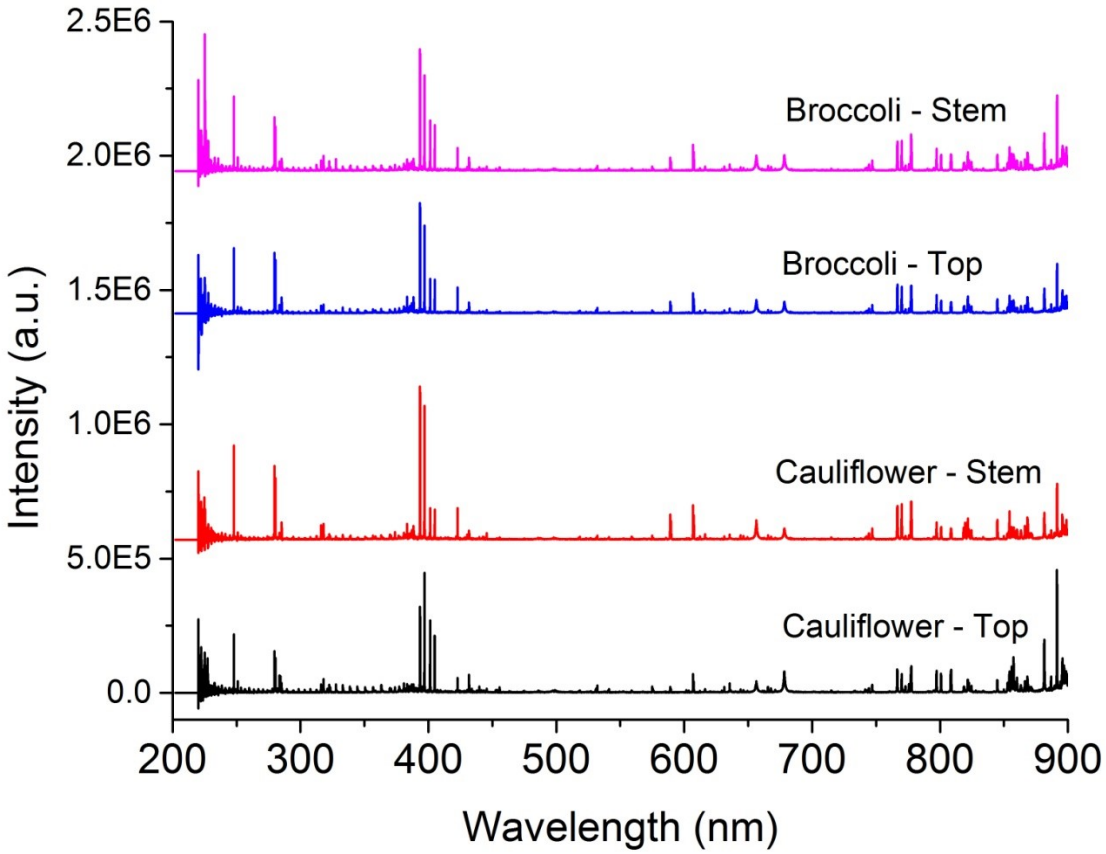

Figure 3.3 LIBS spectra obtained from top and stem parts of cauliflower and broccoli.

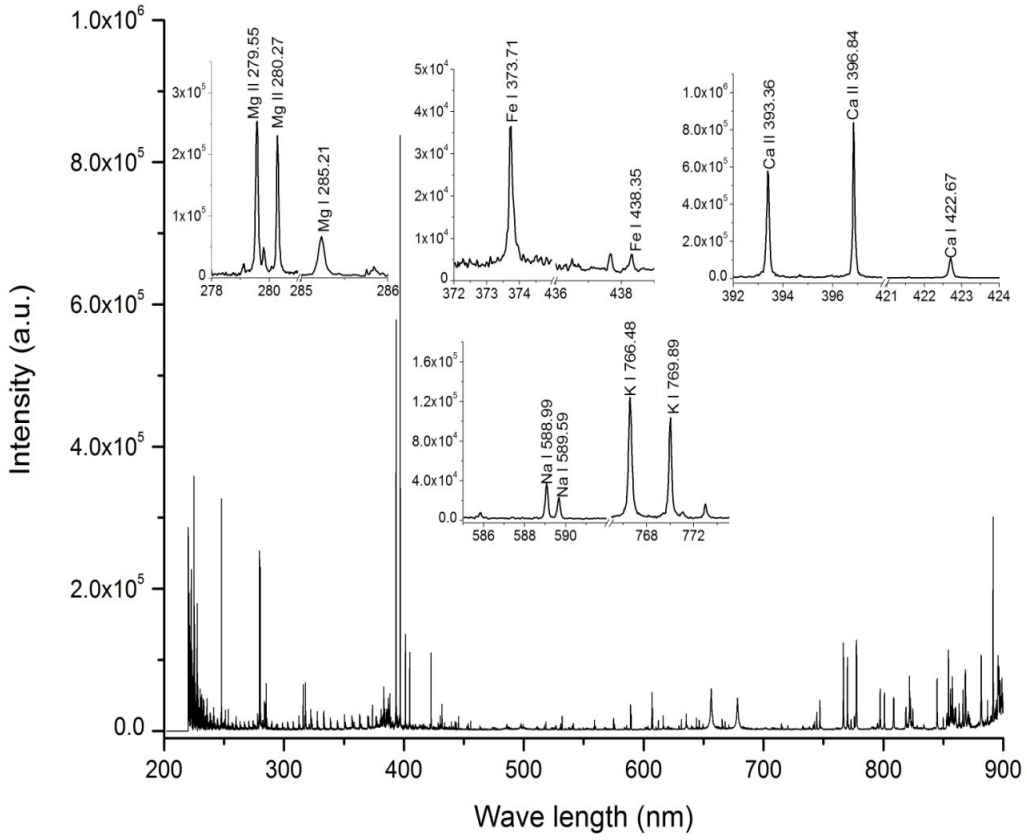

Figure 3.4 LIBS spectra showing different spectral lines.

3.5.2 Determination of Plasma Temperature and Electron Density

To determine the plasma temperature, the Boltzmann plot method was employed. Taking the natural logarithm, Equation (3.3) can be written as

$$ln\left(\frac{I_{ik}\lambda_{ik}}{g_i A_{ik}}\right) = \left(-\frac{1}{k_B T}\right) E_i + ln\left(\frac{Nhc}{U(T)}\right) \tag{3.6}$$

when the term on the left-hand side is plotted against E_i, it yields a linear plot known as the Boltzmann plot. The slope $-1/k_BT$ was used to determine temperature T.

We used neutral and ionic lines of Ca separately to find the Boltzmann plots for the determination of temperature of atoms and ions (i.e. T_e and T_i). The used neutral lines were Ca I 422.67, Ca I 558.87, Ca I 643.9, and Ca I 646.25 nm and the ionic lines were Ca II 315.88, Ca II 370.6, Ca II 393.36, and Ca II 396.84 nm. Spectroscopic constants for these spectral lines from the NIST Atomic Database [27] are presented in Table 3.1 and Boltzmann plots are shown in Figure 3.5.

Table 3.1 Spectroscopic constants for Ca lines

Wavelength (nm)	A_{ki} (s^{-1})	E_i (eV)	E_k (eV)	Statistical wt.	
				g_i	g_k
Ca I 422.67	2.18×10^8	0.00	2.93	1	3
Ca I 558.87	4.9×10^7	2.52	4.74	7	7
Ca I 643.90	5.3×10^7	2.52	4.45	7	9
Ca I 646.25	4.7×10^7	2.52	4.44	5	7
Ca II 315.88	3.1×10^8	3.12	7.04	2	4
Ca II 370.60	8.8×10^7	3.12	6.46	2	2
Ca II 393.36	1.47×10^8	0.00	3.15	2	4
Ca II 396.84	1.4×10^8	0.00	3.12	2	2

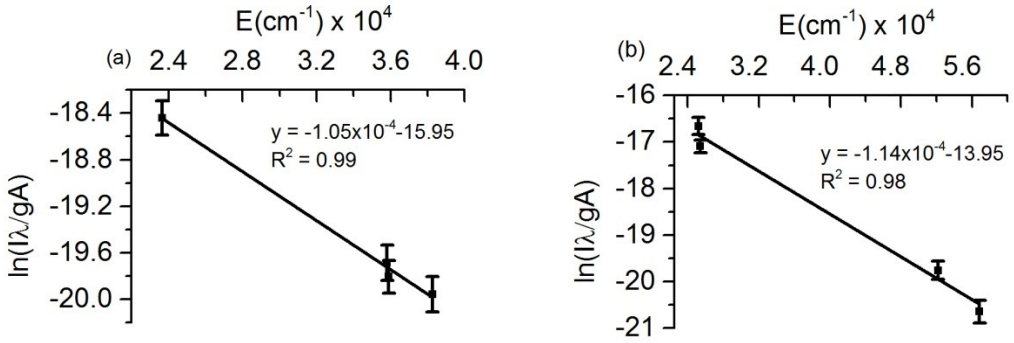

Figure 3.5 Boltzmann plots: (a) from Ca I lines and (b) from Ca II lines. (Error bars represent the standard deviations of five replicates).

We calculated temperature for fifty spectra and the average value was calculated for both cauliflower and broccoli separately. The temperature of atoms (T_e) and ions (T_i) was found in the range of 1.115 eV (~13000 K) for both cauliflower and broccoli. This high value of temperature may be because of high laser energy (96 mJ) used to ablate the sample.

For the estimation of electron density, the Saha- Boltzmann equation was used, which is given as [28-31].

$$n_e = \frac{I_z^*}{I_{z+1}^*} 6.04 \times 10^{21} (T)^{3/2} \times exp\left[\frac{-E_{k.z+1} + E_{k,z} - \varkappa_z}{k_B T}\right] \quad cm^{-3} \qquad (3.7)$$

where $I_z^* = I_z \lambda_{ki,z} / g_{k,z} A_{ki,z}$, I_z is intensity of spectral line of an element in the ionization stage z, and $\varkappa_z$ is the ionization energy of the species in the ionization stage z.

As the Ca I 422.67 nm line was the most intense and well isolated neutral line, it was used for the estimation of electron density, which was estimated to be 1.9 x10^{19}cm^{-3}.

For the Ca I 422.67 nm line, the value of the right-hand side of Equation (3.5) (i.e., $1.6 \times 10^{12} T^{1/2} (\Delta E)^3$) was calculated to be 4.58×10^{15} cm^{-3}. As Equation (3.5) (McWhirter criterion) is valid, the plasma can be considered to be in LTE.

3.5.3 Multivariate Analysis

Vegetable flowers are natural products composed of many elements and compounds. They can be treated as a complex mixture of different elements with unknown concentrations. Hence, the principal component analysis (PCA) technique was used to find if there was a difference between two samples in terms of LIBS spectra. PCA is a multivariate analysis (MVA) technique that provides visual representation of the relationships between samples and variables. It brings characteristic information of

original variables and displays them onto a lesser number of variables known as principal components (PC). Two attributes of PCA (scores and explained variances) were considered here. Scores describe the characteristics of samples and show the differences or similarities of samples. It is a two-dimensional scatter plot of scores of two specified principal components. The closer the samples are in the scatter plot, the more similar they are and samples far away from each other are different from each other. Explained variance shows how much of the variation in the data is described by the different components.

Unscrambler (version 10.3) CAMO software was used for PCA. For this, the whole spectral range was divided into five small spectral ranges: 245-290, 390-440, 580-610, 760-775, and 890-895 nm. These spectral ranges include emission lines of interest of Ca, Mg, Na, K, and Fe. A total of 42 samples, 21 from organic and 21 from conventional vegetable flowers, with 50 spectra from each were considered for PCA. Explained variance showed that the data was sufficiently expressed by seven components. Indeed, the first two PC's covered more than 65% of the total variance. We performed PCA to see the similarity or difference between top parts (and stem parts) of organic and conventional cauliflowers (and broccolis) separately.

Figures 3.6(a) and (b) show the scores plot with the first two PCs (PC1 covered 50% and PC2 covered 16% of the total variance) and that with 3rd and 4th PC's (PC3 covered 10% and PC4 covered 5% of total variance) respectively, for the top parts of organic and conventional cauliflowers by taking all five ranges together. Comparison of stem parts also showed exactly similar results as for the top parts. Similarly, PCA was performed to see if there is any difference or similarity between top and stem parts of

cauliflowers. Scores plot for top and stem parts of organic cauliflower is shown in Figure 3.6(c) and exactly similar plot was obtained for conventional cauliflower as well.

Again, to see the difference or similarity between organic and conventional broccoli, PCA was performed for top and stem parts separately. The scores plots were exactly similar to those of cauliflowers. Scores plot for the top parts of organic and conventional broccoli is presented in Figure 3.6(d).

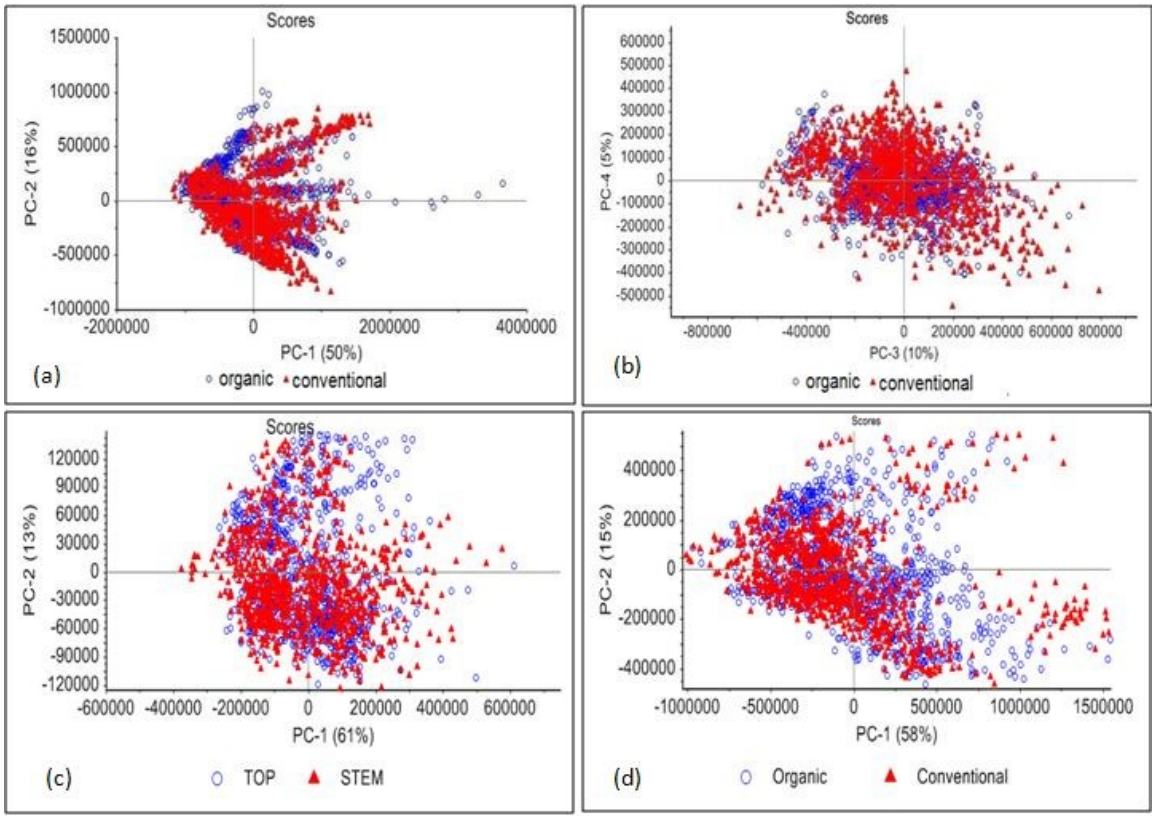

Figure 3.6 Scores plots: (a, b) for top parts of organic and conventional cauliflowers. (c) for top and stem parts of organic cauliflower. (d) for top parts of organic and conventional broccoli.

From this PCA performed with large number of samples for both cauliflower and broccoli, it can be concluded that there should not be any significant difference between

organic and conventional vegetable flowers (cauliflower and broccoli) in terms of elemental lines we have taken into account. However, when we performed a one-to-one comparison, i.e., just one sample with 50 spectra from organic vegetable and the other from conventional one, we obtained a random result. Sometimes, we obtained a significant difference and sometimes no difference between organic and conventional vegetables, but most of the time, we got no difference. For one-to-one comparison, we performed univariate analysis as described below.

3.5.4 Univariate Analysis

For univariate analysis of elemental presence in vegetable flowers, intensity of different spectral lines of elements and their intensity ratio with some reference lines were taken into account. Since the samples were prepared manually, it is hard to guarantee that particle size in the sample was the same and sample distribution on glass slides was perfectly uniform. There is the possibility of uncertainty in intensity measurements and comparison due to these deficits, but these possible effects are expected to be mitigated against by employing normalized intensity and intensity ratios. Hence, we have used normalized intensity of spectral lines and their intensity ratio with some reference lines for comparison.

In the spectra obtained from cauliflower and broccoli, the most intense strong lines of Ca, Mg, K and Na were Ca II 396.84, Mg II 279.55, K I 769.89, and Na I 588.99 nm, respectively. Compared to others, Fe lines were very less intense. Ca II 396.84 and Mg II 279.55 nm are ionized atomic lines, and K I 769.89 and Na I 588.99 nm are neutral atomic lines. When intensity of these intensive lines was compared, it was found that the Ca II 396.84 nm line has the largest and Na I 588.99 nm has the smallest values of

intensity among these four atomic lines as shown in Figure 3.7. The Mg II 279.55-nm line had higher intensity than the KI 769.89 nm line (i.e., $I_{Ca\ II\ 396.84} > I_{Mg\ II\ 279.55} > I_{K\ I\ 769.89} > I_{Na\ I\ 588.99}$, where I represents intensity of line given). The most intense ionized atomic lines, Ca(II) 396.84 and Mg(II) 279.55 nm, were taken as reference lines to find intensity ratios. We compared normalized intensity of different atomic lines as well as their intensity ratio with these reference lines between organic and conventional vegetable flowers by considering top and stem parts separately. The intensity mentioned hereafter is the normalized intensity.

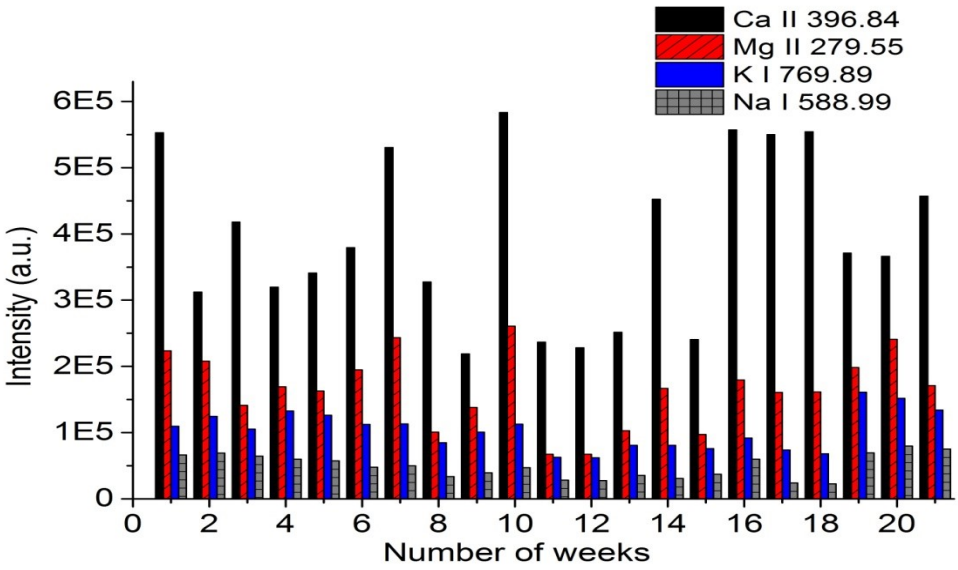

Figure 3.7 Comparison of intensity of lines Na I 588.99, K I 769.89, Mg II 279.55, and Ca II 396.84 nm.

3.5.4.1 Comparison of Organic and Conventional Cauliflowers

To compare organic and conventional cauliflowers, the most intense neutral spectral lines (Ca I 422.67, Mg I 285.21, K I 769.89, Na I 588.995, Fe I 438.35 nm) and

ionized spectral lines (Ca II 396.84 and Mg II 279.55 nm) were selected. Intensity of these lines of organic and conventional cauliflowers were compared for twenty-one weeks using fresh pieces of sample each time. Student t-test at a significance level of 5% was used to find if there was significant difference in intensity of selected lines between organic and conventional cauliflowers. If the t-test showed a significant difference, it was noted which one has the higher value by comparing the average values of intensity. Since the comparison result was not found to be consistent, we counted the number of times (weeks) that intensity of atomic lines in organic cauliflower had the higher value or conventional cauliflower had the higher value or there is no difference. If the same result was obtained for more than 50% of the time, we considered it as occurring most of the time.

Figure 3.8 shows the graphical comparison of intensity of the Mg I 285.21-nm line between top parts of organic and conventional cauliflower, where the number of times that intensity of the line is higher in organic is 2, that in conventional is higher is 3 and no difference is 16 out of 21. As the number 16 is significantly greater than both 2 and 3, we say that there is no significant difference most of the time in intensity of the Mg 285.21-nm line between top parts of organic and conventional cauliflowers. The error bars represent the standard deviations of ten replicates. Similarly, we compared intensity of all the selected lines. Top parts and stem parts were compared separately.

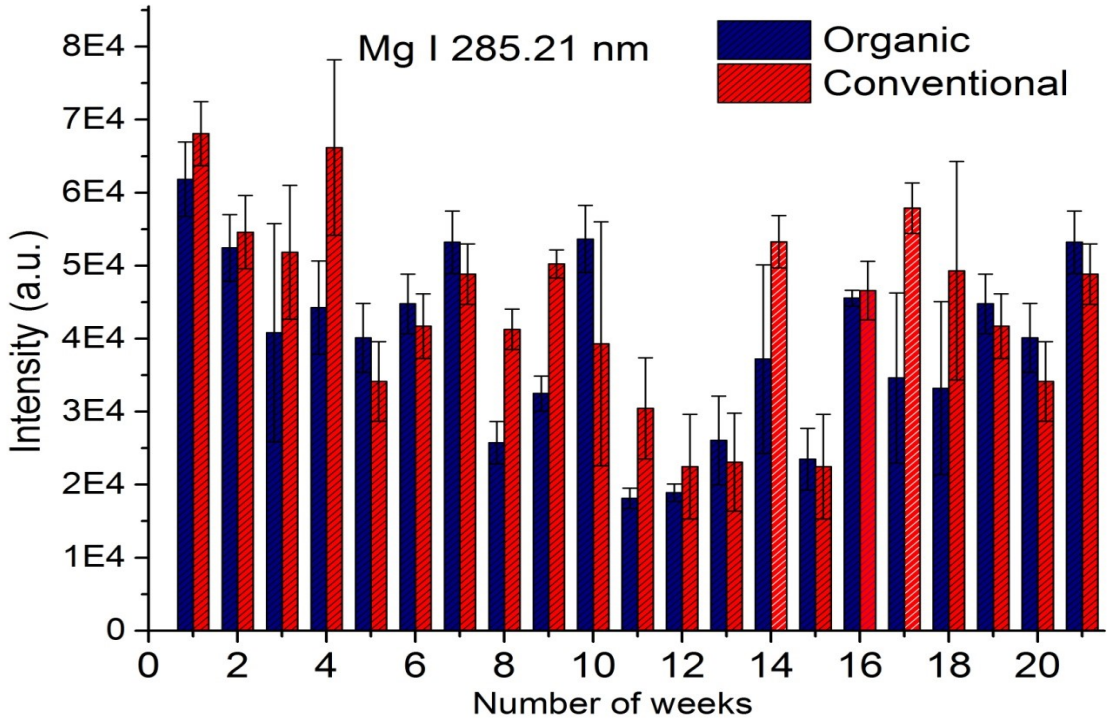

Figure 3.8 Comparison of intensity of the Mg I 285.21-nm line between the top parts of organic and conventional cauliflowers.

Table 3.2. shows the comparison of intensity of different lines of elements Ca, Mg, K, Na, and Fe between top parts (and stem parts) of organic and conventional cauliflowers. For both top and stem parts, all the neutral lines (Ca I 422.67, Mg I 285.21, K I 769.89, Na I 588.995, Fe I 438.35 nm) and ionized lines (Ca II 396.84 and Mg II 279.55 nm) have shown that the number of times that there is no difference in intensity is greater than that of both organic higher and conventional higher.

Again, intensity ratios of these lines (Ca I 422.67, Mg I 285.21, K I 769.89, Na I 588.995, and Fe I 438.35 nm) with reference lines (Ca II 396.84 and Mg II 279.55 nm) were compared between organic and conventional cauliflowers. Process of comparison was exactly the same as that of intensity explained above. Comparison of intensity ratio

of the Mg I 285.21 nm line with the Ca II 396.84-nm line between the top parts of organic and conventional cauliflowers is shown in Figure 3.9. Comparison of all the intensity ratios of different lines between top parts (and stem parts) of organic and conventional cauliflowers is presented in Table 3.3.

While comparing top parts, there was no difference most of the time (60% or more of the time) in values of intensity ratios of lines (Ca I 422.67, Mg I 285.21, K I 769.89, Na I 588.99, and Fe I 438.35 nm) with both the reference lines (Ca II 396.84 and Mg II 279.55 nm) between organic and conventional cauliflowers. Again, an exactly similar result was obtained for the stem parts.

Table 3.2 Comparison of intensity between organic and conventional cauliflowers

Spectral lines	Number of comparisons of Intensity					
	Top parts			Stem parts		
	Organic higher	Conventional higher	No difference	Organic higher	Conventional higher	No difference
Ca I 422.67	4	3	14	4	3	14
Ca II 396.84	4	4	13	2	4	15
Mg I 285.212	2	3	16	3	4	14
Mg II 279.55	1	4	16	4	4	13
KI 769.89	4	3	14	4	3	14
Na I 588.99	3	5	13	3	5	13
Fe I 438.35	4	3	14	4	3	14

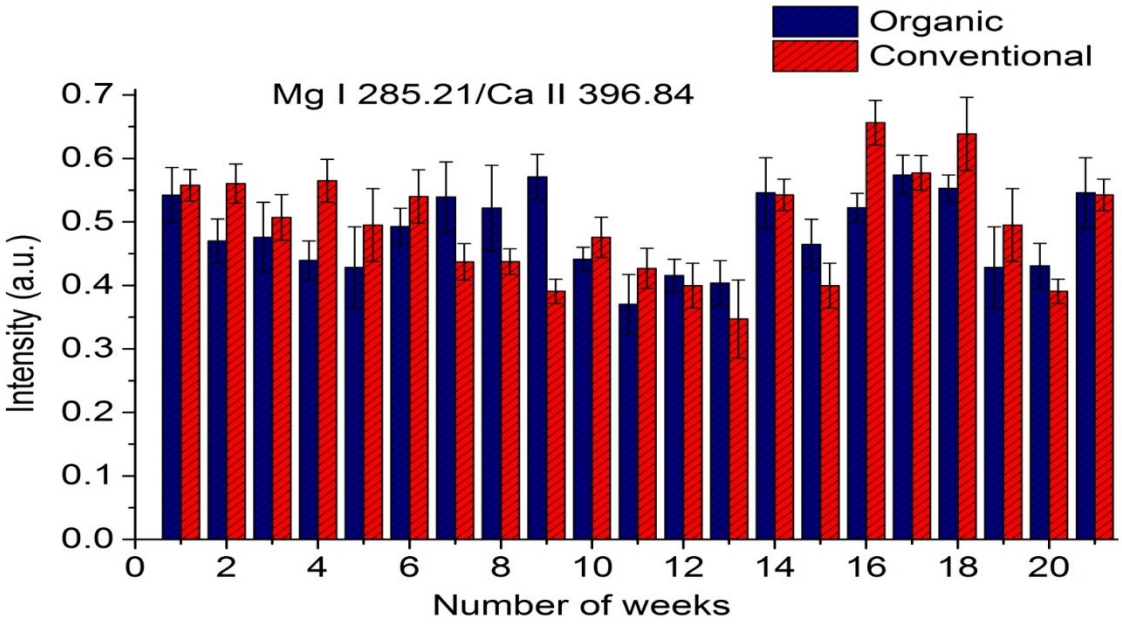

Figure 3.9 Comparison of intensity ratio of the Mg I 285.21-nm line with the Ca II 396.84-nm line between the top parts of organic and conventional cauliflowers.

Table 3.3 Comparison of intensity ratio between organic and conventional cauliflowers

Intensity ratio	Number of Comparisons of Intensity ratio					
	Top parts			Stem parts		
	Organic higher	Conventional higher	No difference	Organic higher	Conventional higher	No difference
Ca I 422.67/Ca II 396.84	2	5	14	2	5	14
Ca I 422.67/Mg II 279.55	3	5	13	3	4	14
Mg I 285.21/Ca II 396.84	2	3	16	2	5	14
Mg I 285.21/Mg II 279.55	2	4	15	3	3	15
K I 769.89/Ca II 396.84	3	5	13	3	4	14
K I 769.89/ Mg II 279.55	7	1	13	4	4	13
Na I 588.99/Ca II 396.84	4	3	14	3	3	15
Na I 588.99/Mg II279.55	3	4	14	3	3	15
Fe I 438.35/Ca II 396.84	4	3	14	4	3	14
Fe I 438.35/Mg II 279.55	3	2	16	3	3	15

For both top and stem parts, although we observed no difference in values of intensity and intensity ratio of spectral lines taken into account most of the times, we observed sometimes that the organic had the higher value and sometimes that the conventionally grown had the higher value. This fact therefore buttresses that there should not automatically be a difference or equality between organic and conventional cauliflowers in terms of intensity for being organic or just for being conventionally grown. However, it strongly advocates the higher possibility of having no difference in values of intensity and intensity ratio of these lines and hence in concentration of these elements also. Moreover, it can be inferred that it may depend on the circumstances under which these cauliflowers are grown. It may depend on seed quality or seed variety, geographical location of farm, climatic conditions, soil quality in which they are grown, naturally and manually provided fertilizers' quality, etc. It cannot be said that the intensities of atomic lines of elements in organic cauliflower have higher values than those of conventionally grown cauliflower or vice versa; rather it depends on individual piece of vegetables.

3.5.4.2 Comparison of Top and Stem Parts of Cauliflowers

In the same way that we compared organic and conventional cauliflowers, the top and stem parts of both organic as well as conventional cauliflowers were also compared. Spectral lines of Ca, Mg, K, Na, and Fe were used for comparison. Most of the time, there was no difference in intensity of all these spectral lines between top and stem parts of organic as well as conventional cauliflowers, which was also supported by comparison of their intensity ratio with reference lines (Ca II 396.84 and Mg II 279.55nm). The comparison results are presented in Table 3.4 and 3.5. The stem parts we considered here

were the parts just below of top parts. This could be one of the probable rationales for having almost equal values of intensity of spectral lines between them. Again, since it was observed that sometimes the top and sometimes the stem parts had higher values of intensity and intensity ratio of spectral lines, it should depend on the particular piece of cauliflower, which of course will depend on its growing circumstances. It showed a possibility of having higher intensity of spectral lines in top parts than stem parts in one plant/piece of cauliflower while the opposite in another plant/piece.

Table 3.4 Comparison of intensity between top and stem parts of cauliflowers

Spectral lines	Number of comparisons of Intensity					
	organic cauliflowers			conventional cauliflowers		
	Top part higher	Stem part higher	No difference	Top part higher	Stem part higher	No difference
Ca I 422.67	5	2	14	6	2	13
Ca II 396.84	4	4	13	4	3	14
Mg I 285.212	5	1	15	4	2	15
Mg II 279.55	3	4	14	5	3	13
KI 769.89	3	4	14	4	3	14
Na I 588.99	3	3	15	3	4	14
Fe I 438.35	5	3	13	4	3	14

Table 3.5 Comparison of intensity ratio between top and stem parts of cauliflowers

Intensity ratio	Number of Comparisons of Intensity ratio					
	organic cauliflowers			conventional cauliflowers		
	Top part higher	Stem part higher	No difference	Top part higher	Stem part higher	No difference
Ca I 422.67 / Ca II 396.84	2	6	13	4	3	14
Ca I 422.67/Mg II 279.55	3	4	14	1	6	14
Mg I 285.21/Ca II 396.84	3	4	14	6	2	13
Mg I 285.21/Mg II279.55	4	3	14	5	2	14
K I 769.89/Ca II 396.84	2	1	18	3	3	15
K I 769/Mg II 279.55	3	3	15	4	4	13
Na I 588.99/Ca II 396.84	3	3	15	4	3	14
Na I 588.99/Mg II279.55	3	3	15	3	4	14
Fe I 438.35/Ca II 396.84	4	3	14	4	3	14
Fe I 438.35/Mg II 279.55	3	2	16	3	3	15

3.5.4.3 Comparison of Organic and Conventional Broccoli

As in the study of cauliflowers, the spectral lines of Ca, Mg, K, Na, and Fe (Ca I 422.67, Ca II 396.84, Mg I 285.21, Mg II 279.55, KI 769.89, Na I 588.99, Fe I 438.35 nm) were considered for the study of broccoli. The comparison process was also exactly the same as for cauliflower. Top parts and stem parts were separately compared between organic and conventional broccoli. From the study of 21 weeks, comparison of top parts between organic and conventional broccoli showed that the number of times of no difference in intensity of lines taken into account is significantly higher than both the number of times of organic had higher values and number of times that conventional had higher values as shown in Table 3.6. Comparison of stem parts also showed exactly similar result as that of top parts.

Table 3.6 Comparison of intensity between organic and conventional broccoli

Spectral lines	Number of comparisons of Intensity					
	Top parts			Stem parts		
	Organic higher	Conventional higher	No difference	Organic higher	Conventional higher	No difference
Ca I 422.67	3	3	15	5	3	13
Ca II 396.84	4	4	13	5	2	14
Mg I 285.21	4	3	14	3	5	13
Mg II 279.55	4	3	14	2	4	15
KI 769.89	5	1	15	5	1	15
Na I 588.99	4	1	16	5	0	16
Fe I 438.35	3	3	15	4	3	14

In addition, intensity ratio of selected atomic lines with reference lines I have considered was compared between organic and conventional broccoli. While comparing top and stem parts separately, there was no difference most of the time in their values between organic and conventional broccolis as presented in Table 3.7.

Table 3.7 Comparison of intensity ratio between organic and conventional broccoli

Intensity ratio	Number of Comparisons of Intensity ratio					
	Top parts			Stem parts		
	Organic higher	Conventional higher	No difference	Organic higher	Conventional higher	No difference
Ca I 422.67 /Ca II 396.84	4	3	14	4	4	13
Ca I 422.67/Mg II 279.55	4	2	15	6	1	14
Mg I 285.21/Ca II 396.84	3	4	14	3	3	15
Mg I 285.21/Mg II 279.55	6	2	13	2	6	13
K I 769.89/Ca II 396.84	4	3	14	5	2	14
K I 769.89/ Mg II 279.55	3	5	13	6	2	13
Na I 588.99/Ca II 396.84	3	4	14	2	6	13
Na I 588.99/Mg II279.55	5	2	14	2	6	13
Fe I 438.35//Ca II 396.84	2	1	18	3	3	15
Fe I 438.35/Mg II 279.55	4	3	14	4	2	15

Hence, this study showed that there is no consistently systematic difference or equality in intensity of atomic lines of different elements present in organic and conventional broccoli. However, since we found that the intensity of lines and their intensity ratio with reference lines had shown most of times no difference, there should be a higher possibility of having no difference in intensity of those lines and hence in concentration of elements considered between organic and conventional broccolis. Concentration of different elements should depend on the particular piece of broccoli, which again may depend on production method.

3.5.4.4 Comparison of Top and Stem Parts of Broccoli

To compare top and stem parts of broccoli, intensity of atomic lines and their intensity ratio with reference lines were compared. Results of comparison of intensity are shown in Table 3.8 and that of comparison of intensity ratio are shown in Table 3.9. Over all, it showed possibility of having no difference in values of intensity of lines and hence

concentration of elements considered for comparison between top and stem parts of both organic as well as conventional broccolis.

Table 3.8 Comparison of intensity between the top and stem parts of broccoli.

Spectral lines	Number of comparison of Intensity					
	Organic Broccoli			Conventional Broccoli		
	Top part higher	Stem part higher	No difference	Top part higher	Stem part higher	No difference
Ca I 422.67	5	3	13	4	4	13
Ca II 396.84	5	2	14	4	2	15
Mg I 285.212	4	2	15	5	2	14
Mg II 279.55	3	4	14	5	3	13
KI 769.89	5	2	14	4	3	14
Na I 588.99	2	4	15	2	6	13
Fe I 438.35	3	3	15	3	2	16

Table 3.9 Comparison of intensity ratio between the top and stem parts of broccoli.

Intensity ratio	Number of Comparisons of Intensity ratio					
	Organic Broccoli			Conventional Broccoli		
	Top part higher	Stem part higher	No difference	Top part higher	Stem part higher	No difference
Ca I 422.67 /Ca II 396.84	4	3	14	6	2	13
Ca I 422.67/Mg II 279.55	3	3	15	4	3	14
Mg I 285.21/Ca II 396.84	6	2	13	6	2	13
Mg I 285.21/Mg II279.55	7	0	14	3	4	14
K I 769.89/Ca II 396.84	3	4	14	5	3	13
K I 769.89/Mg II 279.55	3	5	13	3	4	14
Na I 588.99/Ca II 396.84	3	3	15	3	5	13
Na I 588.99/Mg II279.55	3	4	14	3	5	13
Fe I 438.35/Ca II 396.84	4	3	14	4	4	13
Fe I 438.35/Mg II279.55	3	2	16	3	3	15

3.5.5 Comparison of Concentration of Nutrient Elements

From Equation (3), the electron density can be expressed as

$$N = \frac{I_{ik}U(T)\lambda_{ik}}{hcA_{ik}g_i} exp\left(\frac{E_i}{kT}\right) \quad (3.8)$$

I used this expression (Eq 3.8) to calculate the ratio of concentration of Ca and Na by using experimental values of intensity of the Ca I 422.67 and Na I 588.99 nm lines and their spectroscopic constants (from Table 3.1). The ratio was found to have values between 1.2 and 3.6 from the study of 21 pieces of cauliflower and broccoli as shown in Figure 3.10. This advocates that the concentration of Ca was 1.2 to 3.6 (average 2.6) times greater than that of Na in those vegetable flowers. Again, concentration of Mg was found to be 4.0 to 7.6 (average 5.7) times larger than Na, concentration of K was 5.3 to 9.1 (average 7.4) times larger than Na, and concentration of Fe was 1.8 to 3.5 (average 2.7) times larger than Na.

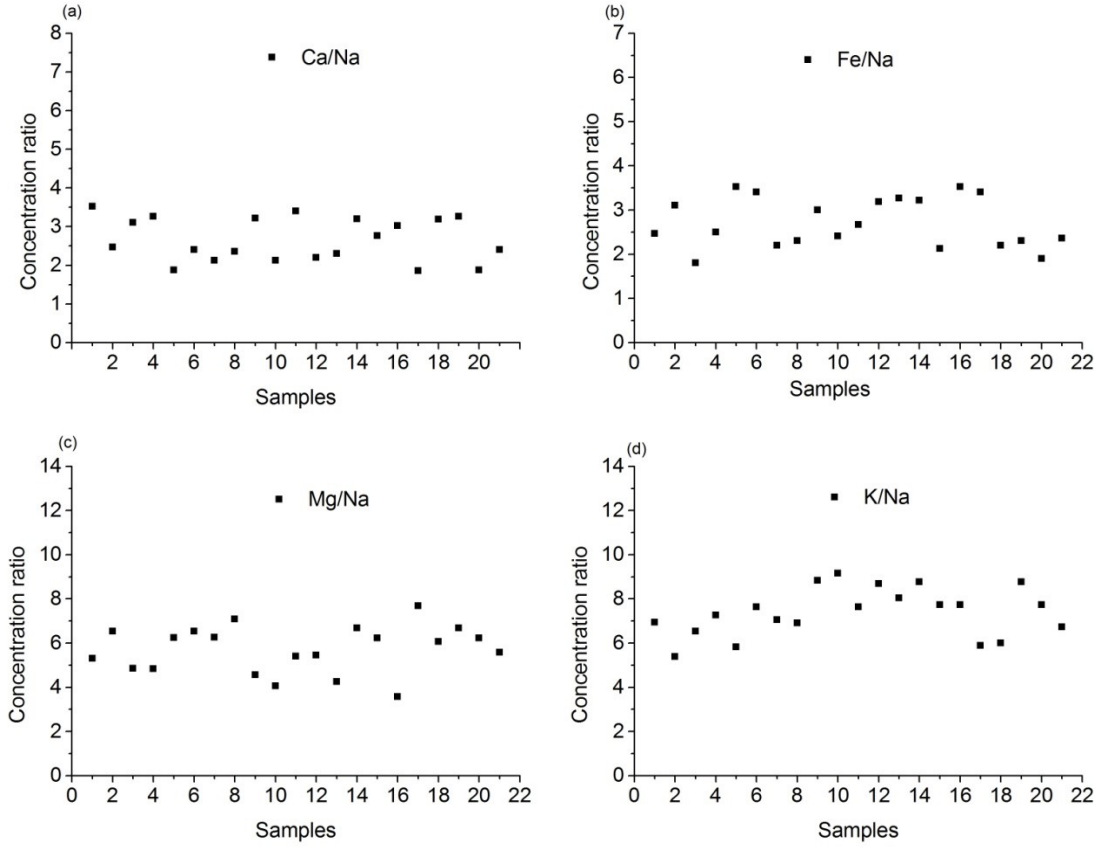

Figure 3.10 Plots showing the variation of concentration ratio of Ca, Fe, Mg, and K with Na respectively.

3.6 Conclusions

Different atomic lines of elements Ca, Mg, K, Na, and Fe were identified in LIBS spectra obtained from both top and stem parts of cauliflowers as well as broccolis, which proves the presence of these elements in these vegetables. Intensity of different atomic lines and their intensity ratio with some reference lines were compared between organic and conventional vegetables (cauliflower and broccoli). For both cauliflower and broccoli, it was found that most of the time there is no significant difference in intensity of the atomic lines of elements Ca, Mg, K, Na, and Fe between organic and conventional.

This probably indicates that there is no consistently systematic difference in concentration of nutritional elements in organic and conventional cauliflowers as well as broccolis. However, since we observed that sometimes organic had higher values of intensity and sometimes conventional had higher values, it can be concluded that it should depend on individual piece of cauliflower and broccoli and their growing circumstances. We also compared top parts and stem parts of both cauliflower and broccoli. In both organic and conventional vegetable flowers, it was found that there should not be any consistently systematic difference in intensity of the spectral lines and hence in concentration of elements considered between top and stem parts of these vegetable flowers.

Again, it was estimated that the concentration of Ca could be 1.2 to 3.6 times greater than that of Na, and Fe concentration to be 1.8 to 3.5 times greater than that of Na. Similarly, concentration of Mg could be 4.0 to 7.6 times and that of K could be 5.3 to 9.1 times larger than that of Na.

Finally, as this result is solely based on the 21-week study of randomly selected cauliflowers and broccolis, it may not be applicable to all vegetables. Detailed study is recommended on vegetables whose growing circumstances are known for comparison of organic and conventional vegetables. In addition, it is recommended to compare the results obtained from LIBS technique and other techniques.

Acknowledgment

The authors are thankful to Department of Physics and Astronomy and the Institute of Clean Energy Technology (ICET), Mississippi State University for providing

lab facilities. We also thank Dr. David Monts for proof reading. Mr. Bhatt and Mr. Ghany are also grateful to Department of Physics and Astronomy for providing graduate assistantships.

REFERENCES

[1] R. Shepherd, *et al.*, "Determinants of consumer behavior related to organic foods," *AMBIO: A Journal of the Human Environment,* vol. 34, pp. 352-359, 2005.

[2] C. K. Winter and S. F. Davis, "Organic foods," *Journal of food science,* vol. 71, 2006.

[3] C. M. Williams, "Nutritional quality of organic food: shades of grey or shades of green?," *Proceedings of the Nutrition Society,* vol. 61, pp. 19-24, 2002.

[4] V. Worthington, "Nutritional quality of organic versus conventional fruits, vegetables, and grains," *The Journal of Alternative & Complementary Medicine,* vol. 7, pp. 161-173, 2001.

[5] S. Association, "Organic farming, food quality and human health: a review of the evidence," *Bristol, United Kingdom: Soil Association,* 2000.

[6] F. Magkos, *et al.*, "Organic food: nutritious food or food for thought? A review of the evidence," *International journal of food sciences and nutrition,* vol. 54, pp. 357-371, 2003.

[7] D. Bourn and J. Prescott, "A comparison of the nutritional value, sensory qualities, and food safety of organically and conventionally produced foods," *Critical reviews in food science and nutrition,* vol. 42, pp. 1-34, 2002.

[8] K. Woese, *et al.*, "A comparison of organically and conventionally grown foods—results of a review of the relevant literature," *Journal of the Science of Food and Agriculture,* vol. 74, pp. 281-293, 1997.

[9] J. Forman and J. Silverstein, "Organic foods: health and environmental advantages and disadvantages," *Pediatrics,* vol. 130, pp. e1406-e1415, 2012.

[10] A. D. Dangour, *et al.*, "Nutritional quality of organic foods: a systematic review," *The American journal of clinical nutrition,* vol. 90, pp. 680-685, 2009.

[11] J. P. Singh and S. N. Thakur, *Laser-induced breakdown spectroscopy*: Elsevier, 2007.

[12] R. S. Harmon, *et al.*, "Laser-induced breakdown spectroscopy (LIBS)–an emerging field-portable sensor technology for real-time, in-situ geochemical and environmental analysis," *Geochemistry: Exploration, Environment, Analysis,* vol. 5, pp. 21-28, 2005.

[13] R. Gaudiuso, *et al.*, "Laser induced breakdown spectroscopy for elemental analysis in environmental, cultural heritage and space applications: a review of methods and results," *Sensors,* vol. 10, pp. 7434-7468, 2010.

[14] O. Samek, *et al.*, "Laser-induced breakdown spectroscopy: a tool for real-time, in vitro and in vivo identification of carious teeth," *BMC Oral Health,* vol. 1, p. 1, 2001.

[15] J. D. Hybl, *et al.*, "Laser-induced fluorescence-cued, laser-induced breakdown spectroscopy biological-agent detection," *Applied optics,* vol. 45, pp. 8806-8814, 2006.

[16] A. R. Boyain-Goitia, *et al.*, "Single-pollen analysis by laser-induced breakdown spectroscopy and Raman microscopy," *Applied optics,* vol. 42, pp. 6119-6132, 2003.

[17] S. J. Rehse, *et al.*, "Towards the clinical application of laser-induced breakdown spectroscopy for rapid pathogen diagnosis: the effect of mixed cultures and sample dilution on bacterial identification," *Applied optics,* vol. 49, pp. C27-C35, 2010.

[18] M. Martin, *et al.*, "Laser-induced breakdown spectroscopy used to detect palladium and silver metal dispersed in bacterial cellulose membranes," *Applied optics,* vol. 42, pp. 6174-6178, 2003.

[19] D. Santos, *et al.*, "Evaluation of femtosecond laser-induced breakdown spectroscopy for analysis of animal tissues," *Applied spectroscopy,* vol. 62, pp. 1137-1143, 2008.

[20] C. R. Bhatt, *et al.*, "Study of atomic and molecular emission spectra of Sr by laser induced breakdown spectroscopy (LIBS)," *Applied optics,* vol. 54, pp. 10264-10271, 2015.

[21] L. C. Trevizan, *et al.*, "Evaluation of laser induced breakdown spectroscopy for the determination of micronutrients in plant materials," *Spectrochimica Acta Part B: Atomic Spectroscopy,* vol. 64, pp. 369-377, 2009.

[22] L. C. Trevizan, *et al.*, "Evaluation of laser induced breakdown spectroscopy for the determination of macronutrients in plant materials," *Spectrochimica Acta Part B: Atomic Spectroscopy,* vol. 63, pp. 1151-1158, 2008.

[23] T. Hussain, *et al.*, "Measurement of nutrients in green house soil with laser induced breakdown spectroscopy," *Environmental monitoring and assessment,* vol. 124, pp. 131-139, 2007.

[24] K. H. Laursen*, et al.*, "Multielemental fingerprinting as a tool for authentication of organic wheat, barley, faba bean, and potato," *Journal of Agricultural and Food chemistry,* vol. 59, pp. 4385-4396, 2011.

[25] D. Devia*, et al.*, "Métodos empleados en el análisis de espectroscopía óptica de emisión: una revisión," *Ingeniería y Ciencia-ing. cienc.,* vol. 11, pp. 239-267, 2015.

[26] G. Cristoforetti*, et al.*, "Local thermodynamic equilibrium in laser-induced breakdown spectroscopy: beyond the McWhirter criterion," *Spectrochimica Acta Part B: Atomic Spectroscopy,* vol. 65, pp. 86-95, 2010.

[27] NIST Atomic Spectra Database [Online]. Available: https://www.nist.gov/pml/atomic-spectra-database

[28] H. R. Griem, *Principles of plasma spectroscopy* vol. 2: Cambridge University Press, 2005.

[29] C. Aragón and J. A. Aguilera, "Characterization of laser induced plasmas by optical emission spectroscopy: A review of experiments and methods," *Spectrochimica Acta Part B: Atomic Spectroscopy,* vol. 63, pp. 893-916, 2008.

[30] M. Shah*, et al.*, "Quantitative elemental analysis of steel using calibration-free laser-induced breakdown spectroscopy," *Applied optics,* vol. 51, pp. 4612-4621, 2012.

[31] V. Unnikrishnan*, et al.*, "Measurements of plasma temperature and electron density in laser-induced copper plasma by time-resolved spectroscopy of neutral atom and ion emissions," *Pramana J. Phys.,* vol. 74, pp. 983-993, 2010.

CHAPTER IV

ANALYSIS OF CHARCOAL BLAST FURNACE SLAGS BY LASER-INDUCED BREAKDOWN SPECTROSCOPY

4.1 Abstract

Laser-induced breakdown spectroscopy (LIBS) was used for the analysis of charcoal blast furnace slags. Plasma was generated by an application of a 1064-nm wavelength Nd:YAG laser beam to the surface of pellets created from the slags. The presence of Al, Ca, Fe, K, Mg, Mn, and Si was determined by identifying their characteristic spectral signatures. Multivariate analysis was performed for the quantification of these elements. The predicted LIBS results were found to be in agreement with inductively coupled plasma-optical emission spectrometry (ICP-OES) analysis. The limits of detection for Al, Ca, Fe, K, Mg, Mn, and Si were calculated to be 0.10, 0.22, 0.02, 0.01, 0.01, 0.005, and 0.18 wt %, respectively.

Most of the content in this chapter has been adapted from *Applied Optics*, Chet R. Bhatt, Christian Gouguel, Jinesh Jain, Harry Edenborn, Dustin McIntire, "Analysis of charcoal blast furnace slags by laser-induced breakdown spectroscopy." Appl. Opt.doc. ID. 302388 (posted 08/31/2017, in press).

4.2 Introduction

Metallurgical slags are waste materials produced during the smelting of metal ores and the production of ferrous and non-ferrous metals. The mineralogical and physical characteristics of slags vary widely depending on their method of production, the composition of the source materials, and the conditions under which the molten slag cools [1]. Blast furnace slag is generated during the production of molten iron via the reduction of iron ore in the presence of a limestone flux and a carbon-based fuel/reductant. Hundreds of blast furnaces operated in the eastern United States prior to the mid-1800s and typically used locally available low-grade iron ores, limestone flux, and charcoal produced from abundant hardwood timber to produce cast iron. The resulting blast furnace slag had few contemporary uses, and is often the only surviving remnant of iron furnace activity at historic furnace sites. Chemical analysis of residual metallurgical slags can be useful in the field of industrial archaeology, potentially aiding in the provenancing of manufactured iron objects [2, 3], the identification of specific sources of the iron ores and fluxes used during iron production [1], as well as providing information on furnace temperature and the relative efficiencies at which each blast furnace operated [4, 5]. In some cases, enough slag remains at sites to consider its reuse as a source of metal, or in secondary uses, such as a construction aggregate [6]. Additionally, the production of alkaline leachates or toxic metals from the natural weathering of slags may be of local environmental concern [1].

X-ray fluorescence (XRF), inductively coupled plasma-optical emission spectrometry (ICP-OES), inductively coupled plasma-mass spectrometry (ICP-MS), and atomic absorption spectroscopy (AAS) are methods currently used for total sample

analysis of metallurgical slags [7-10]. XRF needs a bulk amount of sample to analyze, has high detection limits, and is not suitable for lighter elements. ICP-OES and ICP-MS are both more time-consuming and sample preparation/dissolution can be tedious. As such, it is promising to look for alternative techniques that can give fast and accurate analysis of a wider range of elemental concentrations and do not require lengthy sample preparation. Laser-induced breakdown spectroscopy (LIBS) has the potential to fulfill these demands. It is a versatile *in situ* method, requires minimal or no sample preparation, and can provide rapid results [11]. Multi-elemental analysis irrespective of the state of the matter can be performed simultaneously [12]. In addition, LIBS can perform depth profiling and thin sections can be analyzed without worry of substrate interference. For qualitative as well as quantitative analysis, LIBS has been employed in various fields, including food science, space exploration and planetary science, geological, nuclear, environmental, agricultural, and pharmaceutical sciences [13-20].

A few studies are reported on the application of LIBS for slag analysis [21-30]. Aragon *et al.* [22] used slag samples obtained from a steel plant to study experimental factors influencing the LIBS analysis. LIBS based generalized curves of growth for quantification of various elements present in slag have been reported in [26]. Kolmhofer *et al*. [28] and Ahamer *et al*. [29] have presented calibration free LIBS for slag analysis. Sanghapi *et al*. [30] studied the slags generated during the gasification process to convert carbon feedstocks into electricity, chemical products, and transport fuel. All these slags differ from calcium-rich silicate iron blast furnace slags. In this study, the application of LIBS for qualitative as well as quantitative analysis of historic iron blast furnace slag samples was demonstrated. Multivariate analysis was employed for the quantification of

elements aluminium (Al), calcium (Ca), iron (Fe), magnesium (Mg), manganese (Mn), potassium (K), and silicon (Si). Since the samples were real slags from industrial furnaces, I was aware that they might be heterogeneous complex mixtures. Therefore, to develop calibration curves, normalized intensities were used.

4.3 Experimental

4.3.1 LIBS Apparatus

Figure 4.1 illustrates the experimental set-up used in this study. A Q-switched Nd:YAG laser (TEMPEST, New Wave Research) operating at 1064 nm, 5 ns, and 1 Hz was used as an excitation source. The laser output energy was varied by means of a pair of half-wave plate and polarizing beam splitter cube (60:40). The pulse energy was monitored throughout the measurements using an Ophir® pyroelectric high energy sensor (PE25BF-DIF-C) and a compact Juno® USB interface connected to the computer. An N-BK7 plano-convex lens of 10-cm focal length was used to focus the laser beam onto the sample surface at normal incidence. Dry air was used to sweep the sample surface to remove accumulation of laser-produced aerosols. The sample was placed on a uniformly rotating platform so that each laser shot would interact with fresh sample. Plasma emission was collected through a telescope made of two UV-grade fused silica plano-convex lenses of 5-cm and 1-cm focal lengths, and a UV-Vis fiber optic of 1000-µm core diameter and 2 meters long (Ocean Optics). The optical fiber was connected to an Echelle spectrograph (ARYELLE 200, LTB Lasertechnik Berlin) which was coupled with a 1024×1024 intensified charge-coupled device (ICCD) camera (PI-MAX4, Princeton Instruments).

In order to obtain the best spectral lines, experimental parameters (pulse energy, gate delay and, gate width) were optimized by considering the favorable signal-to-noise ratio (SNR). Taking some strong lines of major elements into account, these experimental conditions were optimized to 32 mJ per pulse, 4 µs gate delay and, 8 µs gate width. The relative standard deviation (% RSD) of the pulse energy was less than 2%. All the spectra from each sample were recorded at these optimized conditions. One hundred laser shots were collected for five replicates and all were averaged to minimize shot-to-shot fluctuation during data evaluation.

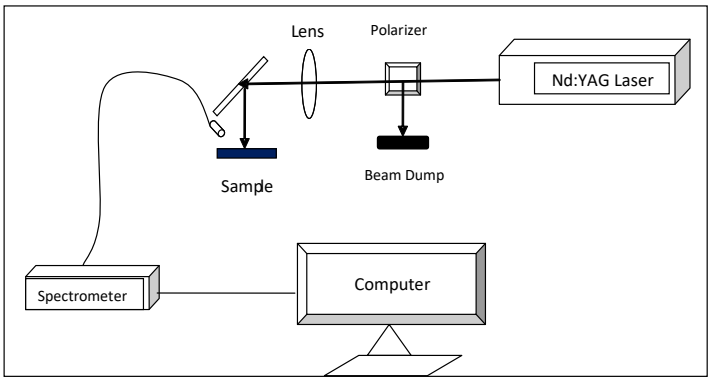

Figure 4.1 LIBS experimental set up for slags

4.3.2 Slags Samples

Ten slag samples were collected from historical charcoal iron furnace sites in eastern (2 samples) and northwestern (8 samples) Pennsylvania. The principal years of furnace operation at these sites were between 1833 and 1857. All samples consisted of relatively homogenous green to gray-green glassy material. Representative samples of each washed slag were powdered in a mortar and pestle and sieved to < 75 µm. Part of

each sample was used for ICP-OES measurements; the data are presented in Table 4.1. The analyte concentrations ranged from 4.52–9.00 % wt. for Al, 4.27–15.84 % wt. for Ca, 0.63–16.47 % wt. for Fe, 0.72–3.06 % wt. for K, 0.48–8.17 % wt. for Mg, 0.38–5.88 % wt. for Mn, and 23.12–31.40 % wt. for Si. The RSDs of the measurements varied between 4 and 23%.

For LIBS analysis, the samples were pressed into pellets by using starch as a binder. A 0.4-gram sample of each powder was mixed thoroughly with about 0.1g (i.e., 20% of total weight) of starch in mortar and pestle. The mixture was pressed into 13-mm diameter and almost 2mm thickness pellets using a Carver® bench top manual pellet press. A pressure of 6.5 ton was applied.

Table 4.1 Elemental composition of the slag samples obtained by ICP-OES.

Samples	Weight %						
	Al	Ca	Fe	K	Mg	Mn	Si
S1	8.26	15.28	0.63	3.06	1.49	0.66	26.55
S2	8.00	4.27	11.59	2.81	0.96	1.92	28.78
S3	5.60	11.81	16.47	1.36	0.64	1.82	23.64
S4	4.52	7.77	0.89	2.69	8.17	1.33	31.40
S5	7.02	7.89	8.54	1.97	1.34	1.47	29.55
S6	5.40	13.91	9.19	0.72	0.48	5.88	23.62
S7	4.55	15.84	1.37	1.46	7.12	0.38	23.12
S8	9.00	11.29	1.47	1.80	0.92	1.72	25.20
S9	8.12	13.90	1.55	1.89	0.72	2.21	25.43
S10	6.20	11.54	4.43	2.46	0.72	3.94	27.59

4.4 Results and Discussion

4.4.1 Qualitative Analysis - Detection of Spectral Lines

Both strong and weak spectral lines of the elements of interest were detected in the LIBS spectra obtained from each sample, which confirms the presence of

corresponding elements in these samples. Matrix effects were observed due to the presence of various elements at varying concentrations (Table 4.1) in each sample. Therefore, the overlapping of emission lines and shifting of wavelength positions were the major challenging factors in identifying the spectral lines. With the help of the NIST Atomic Database [31]and careful analysis of factors like wavelength and intensity, I was able to identify suitable emission lines of Al, Ca, Fe, K, Mg, Mn, and Si. Figure 4.2 is a snapshot of the spectra observed in the whole wavelength range (200 to 800 nm) from sample S-5. The main spectral lines which were well separated and free from overlap were Al I doublets (308.21, 309.27, 394.40, and 396.15 nm), Ca II doublets (315.88, 317.93, 393.36, and 396.84 nm), Ca I 422.67 nm, Fe II (259.93 and 274.93 nm), Fe I (252.28 and 438.35 nm), K I doublet (766.48 and 769.89 nm), Mg II 280.27 nm, Mg I 285.21 nm, Mn II 257.61 nm, Mn I triplet (403.07, 403.30, and 403.44), and Si I (251.61 and 288.15 nm) and are presented in Figure 4.3. The spectroscopic data of these emission lines are given in Table 4.2. Self-absorption was observed for some emission lines, which was likely attributed to high concentrations of those elements.

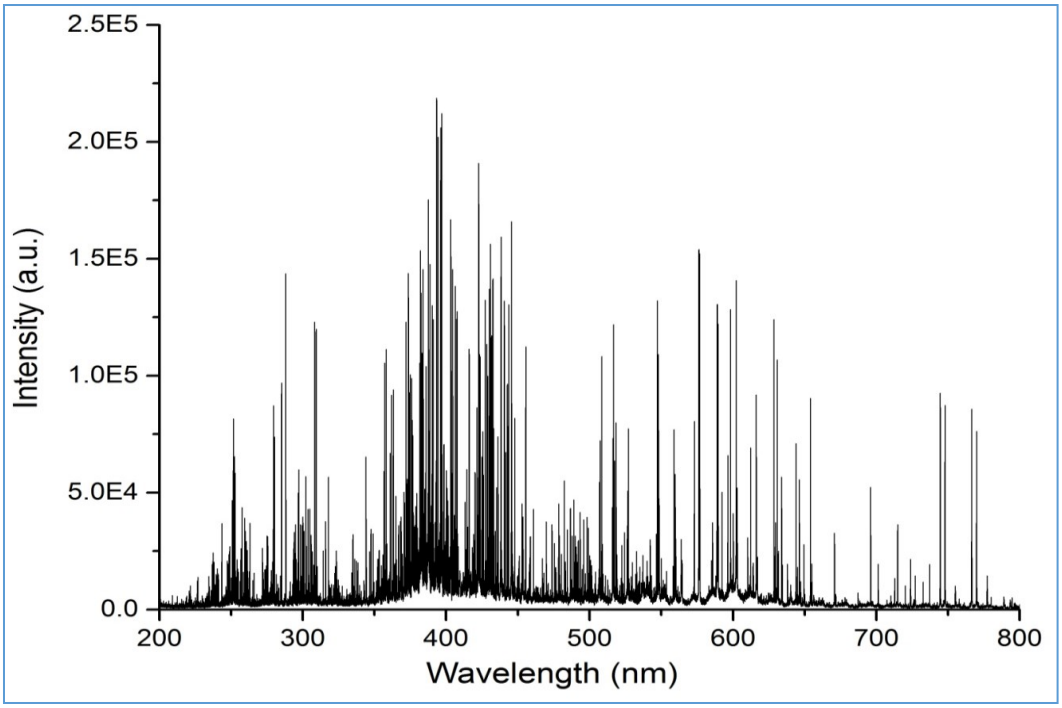

Figure 4.2 Whole LIBS spectra obtained from the slag sample S-5.

Table 4.2 Spectroscopic data of the spectral lines identified in the slag samples. The wavelength (λ), lower and upper energy ($E_i - E_j$) and statistic weight ($g_j - g_j$) of the transition levels, and probability for spontaneous emission (A_{ij}) are indicated [31].

Species	λ_{ij} (nm)	$E_i - E_j$ (cm^{-1})	A_{ij} (10^8 s^{-1})	$g_j - g_j$
Al I	308.21	0.0-32435.453	5.87E-1	2-4
	309.27	112.061 - 32436.796	0.729	4 - 6
	394.40	0.0 - 25347.756	0.499	2 - 2
	396.15	112.061 - 25347.756	0.985	4 - 2
Ca II	315.88	25191.51-56839.25	3.1	2-4
	317.93	25414.40 - 56858.46	3.6	4-6
	393.36	0.025414.40	1.47	2-4
	396.84	0.0-25191.51	1.4	2-2
Ca I	422.67	0.0-23652.304	2.18	1-3
Fe II	259.93	0.0-38458.9934	2.35	10-10
	274.93	8391.9554-44753.8179	2.16	6-8
Fe I	252.28	0.0-39625.804	2.13	9-9
	438.35	11976.239-34782.421	0.5	9-11
K I	766.48	0.0-13042.896027	0.38	2-4
	769.89	0.0-12985.185724	0.375	2-2
Mg II	280.27	0.0-35669.31	2.57	2-2
Mg I	285.21	0.0-35051.264	4.91	1-3
Mn II	257.61	0.0-38806.691	2.80	7-9
Mn I	403.07	0.0-24802.25	0.17	6-8
	403.30	0.0-24788.05	0.165	6-6
	403.44	0.0-24799.32	0.158	6-4
Si I	251.61	223.157-39955.053	1.68	5-5
	288.15	6298.85-40991.884	2.17	5-3

λ is the wavelength position of the spectral line.
E_i and E_j are the energies in the upper level i and lower level j, respectively.
A_{ij} represents the transition probability from level i to j.
g_i and g_j represents the statistical weights of the energy level i and j, respectively.

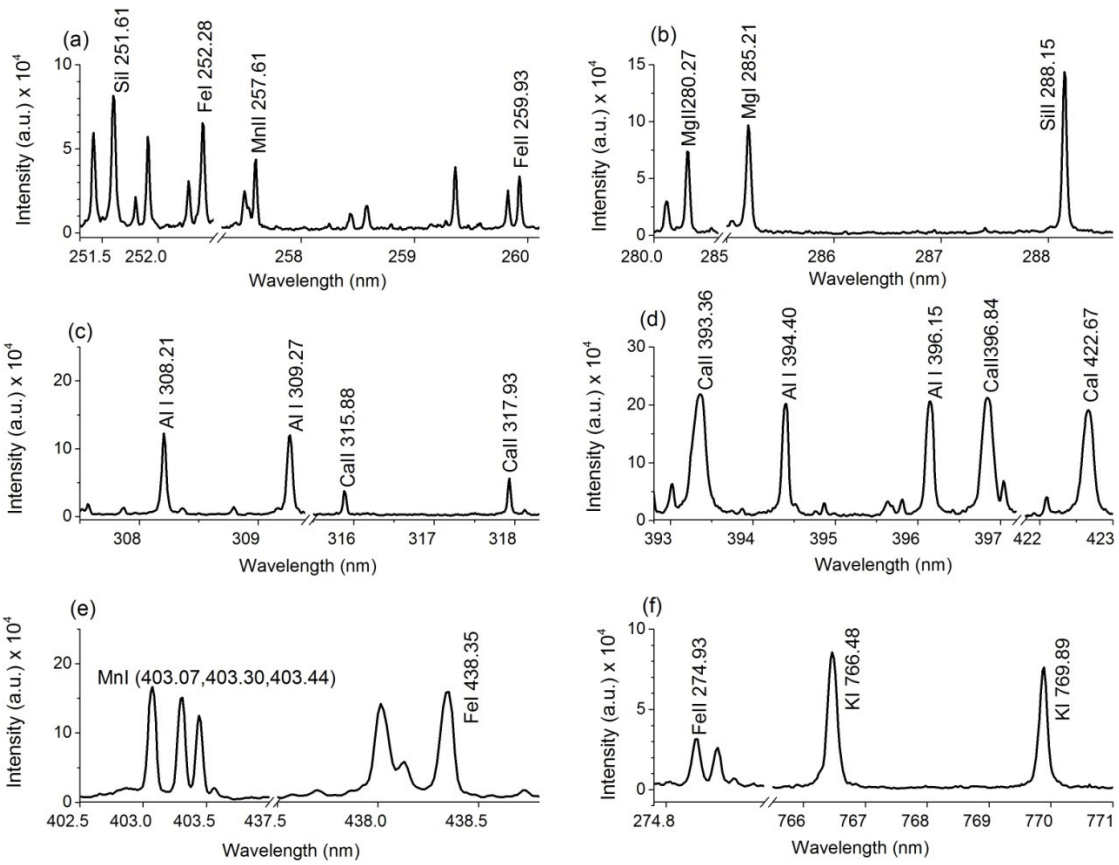

Figure 4.3 Identified spectral peaks of different elements in reduced wavelength ranges.

4.4.2 Quantitative Analysis

The slag samples were identified as complex mixtures of various elements. Selecting emission lines free from self-absorption and interference in complex spectra (Figure 4.2) is more time consuming and hectic. Reported studies have also shown multivariate analysis as more appropriate compared to univariate for the analysis of complex samples [32-34].

Therefore, multivariate analysis was performed to obtain calibration models for the quantification of analytes. The Unscrambler X version 10 software was employed to

obtain partial least squares regression (PLS-R) [35]. Partial least squares (PLS) is one of the multivariate analytical techniques used in chemometrics. It helps to reduce the matrix effect when dealing with complex samples [36]. It also generates a regression model that correlates the two matrices (X and Y) and finds variables in one (X) that predict variables in another (Y), so the matrix X can be regarded as a set of predictors (n objects, m variables) and Y as a set of responses (n objects, p responses). In this model, the samples with known concentrations are used to construct a model correlating two matrices X and Y, which can be later used to predict unknown concentrations of other samples.

In this study, elemental spectra were recorded from samples where each element had varying concentrations. The spectral intensities were normalized and were taken as m variables of predictors and concentrations were p responses. Here, nine samples were used to develop the model and one sample was used to check the predictive capacity of these models. Liang Xu and Israel Schechter have mentioned that by selecting a proper spectral range, better results can be obtained [37]. Therefore, we have selected spectral ranges containing strong lines of emission of elements. We have taken seven components (factors) into account to obtain PLS-R plots. The explained variance illustrates how much of the total variation in X or Y is described by models including different numbers of components. Ideally, models should have large (close to 100%) total explained variance with as few components as possible. The predicted versus reference plot in PLS-R displays the predictive capacity of the developed models.

Explained validation variances of the analyzed elements (Al, Ca, Fe, K, Mg, Mn, and Si) are shown in Figure 4.4 and calibration and validation curves are shown in Figure

4.5. For all the elements, very good coefficients of determination (R^2) were obtained for both calibration and validation plots (Figure 4.5).

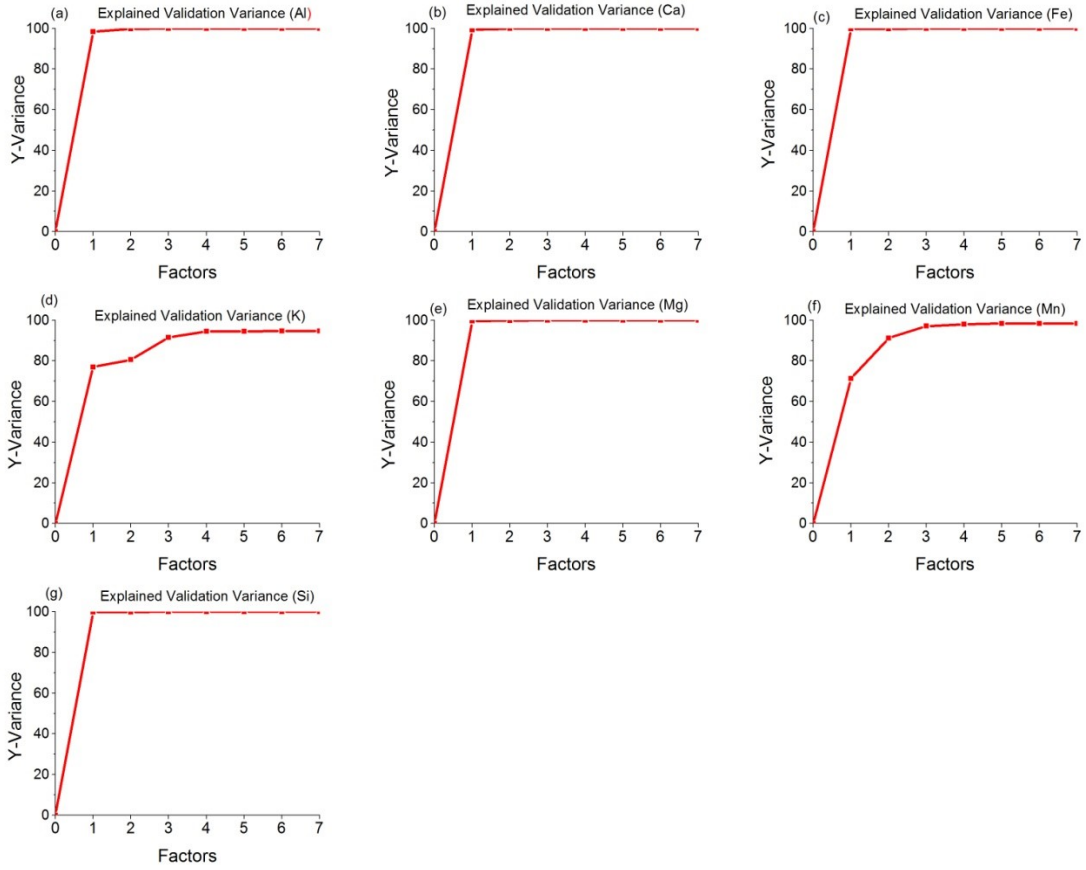

Figure 4.4 Explained validation variances for (a) Al, (b) Ca, (c) Fe, (d) K, (e) Mg, (f) Mn, (e) Si.

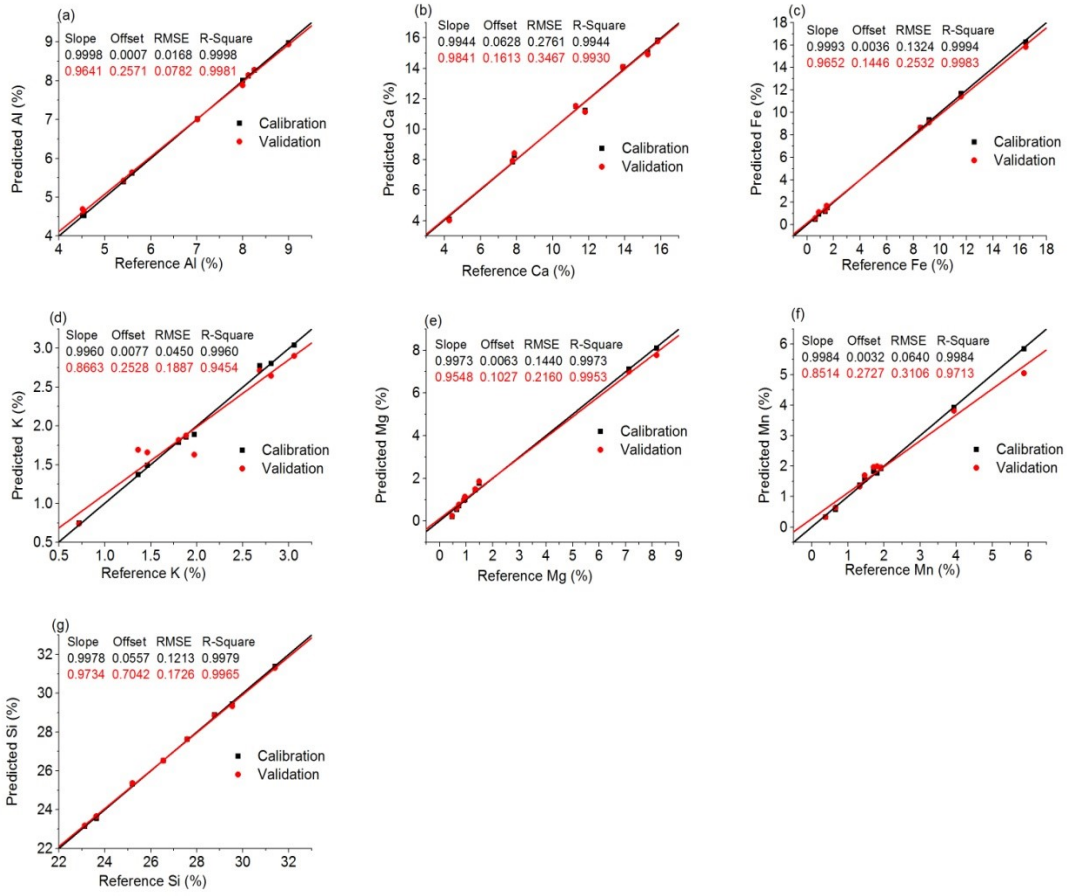

Figure 4.5 PLS-R calibration models for (a) Al, (b) Ca, (c) Fe, (d) K, (e) Mg, (f) Mn, (e) Si.

4.4.2.2 Predictive Capacity of Calibration Models

As mentioned above, out of ten samples, nine were used to develop calibration models and one (sample S10) was used as an unknown sample to check the predictive capacity of these developed models. Concentrations of Al, Ca, Fe, K, Mg, Mn, and Si in the unknown sample were predicted by using PLS-R models. These predicted values of concentrations of elements were compared with those obtained by ICP analysis and difference is expressed as relative percentage difference taking ICP value as the reference

(Table 4.3). Comparison is presented graphically in Figure 4.6. From the comparison of PLS and ICP results, it has been observed that the relative difference is less than 25% for all the elements. In fact, PLS relative difference is less than 6% for Al, Ca, Fe, and Si, while it is between 18 and 24% for K, Mg, and Mn. High relative difference may be mainly because of two reasons. The primary reason may be the heterogeneity of the unknown sample and the other reason is that the matrix and elemental composition of the samples used in developing calibration models and that of unknown sample may be different. Generally, the higher the difference in composition of samples used in models and unknown sample, the higher will be the uncertainty. In this study, relative difference is obtained to be less than 24%.

Table 4.3 Comparison of PLS predicted and ICP results

Element	Concentration (ICP)	Concentration (PLS)	Relative difference (%)
Al	6.20	6.22	0.41
Ca	11.54	11.51	0.25
Fe	4.43	4.68	5.71
K	2.46	1.89	23.05
Mg	0.72	0.55	23.84
Mn	3.94	3.20	18.62
Si	27.59	27.50	0.28

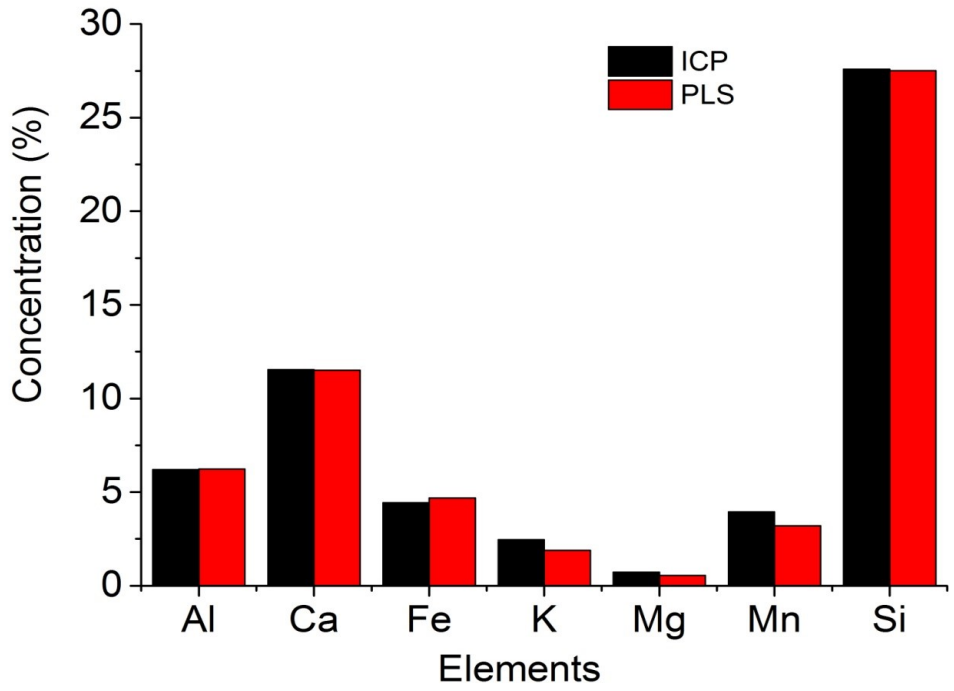

Figure 4.6 Graphical comparison of ICP and PLS values.

4.4.2.3 Limits of Detection (LOD)

The limit of detection (LOD) was calculated using the formula

$$LOD = \frac{3\sigma C}{I} \quad (4.1)$$

where σ is the standard deviation of the background, C is the minimum concentration of the analyte, and I is the intensity of analyte lines.

Minimum concentrations of elements Al, Ca, Fe, K, Mg, Mn, and Si used in calibration curves were 4.52, 4.27, 0.63, 0.72, 0.48, 0.38, and 23.12 wt % (ICP results, Table 4.1). By using the lines Al I 396.15 nm, Ca II 317.93 nm, Fe I 438.35 nm, K I 766.48 nm, Mg I 285.21 nm, Mn I 403.07 nm, and Si I 288.15 nm for Al, Ca, Fe, K, Mg,

Mn, and Si, estimated values of the limits of detection were 0.10, 0.22, 0.02, 0.01, 0.01, 0.005, and 0.18 wt % respectively.

4.5 Conclusions

Laser-induced breakdown spectroscopy (LIBS) appears to be a promising technique for rapid determination and measurement of major elements (Al, Ca, Fe, K, Mg, Mn, and Si) in the charcoal blast furnace slags. Calibration models were developed for the quantification of elements by multivariate analysis (PLS-R). Concentrations of different elements in an unknown sample were estimated by using developed models. These estimated values were compared with ICP results, and found in comparable ranges for most of the elements. The limits of detection were estimated as 0.10, 0.22, 0.02, 0.01, 0.01, 0.005, and 0.18 % for Al, Ca, Fe, K, Mg, Mn, and Si respectively.

Acknowledgement

This work is supported by Department of Energy's National Energy Technology Laboratory (NETL).

REFERENCES

[1] N. M. Piatak, *et al.*, "Characteristics and environmental aspects of slag: A review," *Applied Geochemistry,* vol. 57, pp. 236-266, 2015.

[2] V. F. Buchwald and H. Wivel, "Slag analysis as a method for the characterization and provenancing of ancient iron objects," *Materials characterization,* vol. 40, pp. 73-96, 1998.

[3] E. Blakelock, *et al.*, "Slag inclusions in iron objects and the quest for provenance: an experiment and a case study," *Journal of Archaeological Science,* vol. 36, pp. 1745-1757, 2009.

[4] J. R. White, "Historic blast furnace slags: archaeological and metallurgical analysis," *Historical metallurgy,* vol. 14, pp. 55-65, 1980.

[5] R. B. Gordon, "Process deduced from ironmaking wastes and artefacts," *Journal of Archaeological Science,* vol. 24, pp. 9-18, 1997.

[6] B. Das, *et al.*, "An overview of utilization of slag and sludge from steel industries," *Resources, conservation and recycling,* vol. 50, pp. 40-57, 2007.

[7] W. Devos, *et al.*, "Laser ablation inductively coupled plasma mass spectrometry (LA-ICP-MS) for spatially resolved trace analysis of early-medieval archaeological iron finds," *Fresenius' journal of analytical chemistry,* vol. 366, pp. 873-880, 2000.

[8] L. Marjanovic, *et al.*, "Use of a simplified generalized standard additions method for the analysis of cement, gypsum and basic slag by slurry nebulization ICP-OES," *Analytical and bioanalytical chemistry,* vol. 379, pp. 104-107, 2004.

[9] C. Navarro, *et al.*, "Physico-chemical characterization of steel slag. Study of its behavior under simulated environmental conditions," *Environmental science & technology,* vol. 44, pp. 5383-5388, 2010.

[10] M. L. F. Sanchez, *et al.*, "Direct analysis of slags by inductively coupled plasma atomic emission spectrometry using slurry sample introduction techniques," *Journal of Analytical Atomic Spectrometry,* vol. 6, pp. 397-401, 1991.

[11] A. K. Knight, *et al.*, "Characterization of laser-induced breakdown spectroscopy (LIBS) for application to space exploration," *Applied Spectroscopy,* vol. 54, pp. 331-340, 2000.

[12] B. Sallé, *et al.*, "Laser-induced breakdown spectroscopy for space exploration applications: Influence of the ambient pressure on the calibration curves prepared

from soil and clay samples," *Spectrochimica Acta Part B: Atomic Spectroscopy,* vol. 60, pp. 479-490, 2005.

[13] C. R. Bhatt*, et al.*, "Comparative Study of Elemental Nutrients in Organic and Conventional Vegetables Using Laser-Induced Breakdown Spectroscopy (LIBS)," *Applied spectroscopy,* p. 0003702817692810, 2017.

[14] F. Colao*, et al.*, "Investigation of LIBS feasibility for in situ planetary exploration: an analysis on Martian rock analogues," *Planetary and Space Science,* vol. 52, pp. 117-123, 2004.

[15] J. D. Winefordner*, et al.*, "Comparing several atomic spectrometric methods to the super stars: special emphasis on laser induced breakdown spectrometry, LIBS, a future super star," *Journal of Analytical Atomic Spectrometry,* vol. 19, pp. 1061-1083, 2004.

[16] B. Sallé*, et al.*, "Laser-induced breakdown spectroscopy for Mars surface analysis: capabilities at stand-off distances and detection of chlorine and sulfur elements," *Spectrochimica Acta Part B: Atomic Spectroscopy,* vol. 59, pp. 1413-1422, 2004.

[17] C. R. Bhatt*, et al.*, "Study of atomic and molecular emission spectra of Sr by laser induced breakdown spectroscopy (LIBS)," *Applied optics,* vol. 54, pp. 10264-10271, 2015.

[18] J. R. Wachter and D. A. Cremers, "Determination of uranium in solution using laser-induced breakdown spectroscopy," *Applied Spectroscopy,* vol. 41, pp. 1042-1048, 1987.

[19] F. DeLucia*, et al.*, "Laser-induced breakdown spectroscopy (LIBS): a promising versatile chemical sensor technology for hazardous material detection," *IEEE Sensors Journal,* vol. 5, pp. 681-689, 2005.

[20] C. R. Bhatt*, et al.*, "Univariate and multivariate analyses of rare earth elements by laser-induced breakdown spectroscopy," *Applied optics,* vol. 56, pp. 2280-2287, 2017.

[21] R. Noll*, et al.*, "Laser-induced breakdown spectrometry—applications for production control and quality assurance in the steel industry," *Spectrochimica Acta Part B: Atomic Spectroscopy,* vol. 56, pp. 637-649, 2001.

[22] C. Aragón*, et al.*, "Investigation of the analysis of pellet samples by laser-induced breakdown spectroscopy: Application to steel making slagss," in *Laser Induced Plasma Spectroscopy and Applications*, 2002, p. ThB3.

[23] M. Kraushaar, *et al.*, "Slag analysis with laser-induced breakdown spectrometry," *Applied spectroscopy,* vol. 57, pp. 1282-1287, 2003.

[24] V. Sturm, *et al.*, "Fast vacuum slag analysis in a steel works by laser-induced breakdown spectroscopy," *Spectrochimica Acta Part B: Atomic Spectroscopy,* vol. 63, pp. 1167-1170, 2008.

[25] V. Sturm, *et al.*, "Laser-induced breakdown spectroscopy for 24/7 automatic liquid slag analysis at a steel works," *Analytical chemistry,* vol. 86, pp. 9687-9692, 2014.

[26] C. Aragón and J. Aguilera, "Quantitative analysis by laser-induced breakdown spectroscopy based on generalized curves of growth," *Spectrochimica Acta Part B: Atomic Spectroscopy,* vol. 110, pp. 124-133, 2015.

[27] T. Zhang, *et al.*, "Quantitative and classification analysis of slag samples by laser induced breakdown spectroscopy (LIBS) coupled with support vector machine (SVM) and partial least square (PLS) methods," *Journal of Analytical Atomic Spectrometry,* vol. 30, pp. 368-374, 2015.

[28] P. Kolmhofer, *et al.*, "Calibration-free analysis of steel slag by laser-induced breakdown spectroscopy with combined UV and VIS spectra," *Spectrochimica Acta Part B: Atomic Spectroscopy,* vol. 106, pp. 67-74, 2015.

[29] C. Ahamer, *et al.*, "Laser-induced breakdown spectroscopy of major and minor oxides in steel slags: Influence of detection geometry and signal normalization," *Spectrochimica Acta Part B: Atomic Spectroscopy,* vol. 122, pp. 157-164, 2016.

[30] H. K. Sanghapi, *et al.*, "Analysis of slags using laser-induced breakdown spectroscopy," *Spectrochimica Acta Part B: Atomic Spectroscopy,* vol. 115, pp. 40-45, 2016.

[31] NIST Atomic Spectra Database [Online]. Available: https://www.nist.gov/pml/atomic-spectra-database

[32] J. W. B. Braga, *et al.*, "Comparison of univariate and multivariate calibration for the determination of micronutrients in pellets of plant materials by laser induced breakdown spectrometry," *Spectrochimica Acta Part B-Atomic Spectroscopy,* vol. 65, pp. 66-74, Jan 2010.

[33] C. B. Stipe, *et al.*, "Laser-Induced Breakdown Spectroscopy of Steel: A Comparison of Univariate and Multivariate Calibration Methods," *Applied Spectroscopy,* vol. 64, pp. 154-160, Feb 2010.

[34] M. M. Tripathi*, et al.*, "Multivariate calibration of spectra obtained by Laser Induced Breakdown Spectroscopy of plutonium oxide surrogate residues," *Spectrochimica Acta Part B-Atomic Spectroscopy,* vol. 64, pp. 1212-1218, Nov-Dec 2009.

[35] Available: http://www.camo.com/helpdocs/The_Unscrambler_Method_References.pdf

[36] S. M. Clegg*, et al.*, "Multivariate analysis of remote laser-induced breakdown spectroscopy spectra using partial least squares, principal component analysis, and related techniques," *Spectrochimica Acta Part B: Atomic Spectroscopy,* vol. 64, pp. 79-88, 2009.

[37] L. Xu and I. Schechter, "Wavelength selection for simultaneous spectroscopic analysis. Experimental and theoretical study," *Analytical Chemistry,* vol. 68, pp. 2392-2400, 1996.

CHAPTER V

STUDY OF RARE EARTH ELEMENTS BY LASER-INDUCED BREAKDOWN SPECTROSCOPY

5.1 Abstract

In this chapter, qualitative and quantitative analysis of various rare earth elements (REEs) in three different types of samples by LIBS is demonstrated. Firstly, univariate and multivariate analyses of six rare earth elements [cerium (Ce), europium (Eu), gadolinium (Gd), neodymium (Nd), samarium (Sm), and yttrium (Y)] have been performed using standard samples. Natural geological samples with low concentration of REEs were used for the LIBS study in the second part. Low and high intensity emission lines of Ce, La, Nd, Y, Pr, Sm, Eu, Gd, and Dy were identified and multivariate analysis was executed by developing partial least squares regression (PLS-R) models for the quantification of Ce, La, and Nd. After using standard and natural geological samples in powder form, liquid samples were used for the study of REEs with the LIBS technique. Eu and Yb in aqueous solutions at ambient and high-pressure conditions were used to record LIBS spectra. Temporal evolution of plasma and the effect of laser pulse energy and pressure on the plasma emission were studied.

A part of the content in this chapter has been adapted from *Applied Optics*, Volume 56, Pages 2280-2287 (2017), Chet R. Bhatt, Fang Y. Yueh, and Jagdish P. Singh, "Univariate and multivariate analyses of rare earth elements by laser-induced breakdown spectroscopy."

5.2 Introduction

Group of fifteen lanthanides with atomic numbers from 57 to 71(La to Lu) and two other elements scandium (Sc) and yttrium (Y) with atomic numbers 21 and 39, respectively are categorized as rare earth elements (REEs). Because of their unique physicochemical properties, REEs have become important for both scientific and technological point of views. Scientifically, the elements have been widely used in geochemistry because the knowledge of their distribution in rocks and minerals, and their mobilization under different environmental conditions can be used to sort out important geochemical and petrogenetic processes [1]. The economic interest of REEs is evident from the fact that the elements play an important role in various fields and are considered essential elements in many industrial applications [2]. The REEs are currently in high demand due to their application in defense and importance in renewable energy industries as well as their use in high-tech products, such as cell phones, magnets, fiber-optic cables, television, hybrid cars, and medical imaging. Though their name suggests that they would be rare, REE's are not that rare; they are relatively abundant in the earth's crust. The only currently discovered minable concentrations are less common than for other elements [3]. In light of globally increasing consumption of rare earth elements, their mining development is also expanding rapidly.

A part of the content in this chapter has been adapted from Applied Spectroscopy, Chet R. Bhatt, Jinesh Jain, Christian Goueguel, Dustin McIntyre, and Jagdish P. Singh, " EXPRESS: Determination of Rare Earth Elements in Geological Samples Using Laser-Induced Breakdown Spectroscopy (LIBS)."
Also, some part has been adapted from Spectrochimica Acta Part B: Atomic Spectroscopy, Chet R. Bhatt, Jinesh Jain, Christian Goueguel, Dustin McIntyre, and Jagdish P. Singh, "Measurement of Eu and Yb in aqueous solutions by underwater laser induced breakdown spectroscopy."

A challenging part of mining rare earth elements is that they are not found in pure form; they are found mostly in minerals as carbonates, halides, oxides, phosphates, and silicates [4, 5]. Several REEs are found usually together. In addition to geological materials (minerals, soils, rocks, ores, sands, and coals), REEs are also found in nuclear materials and biological samples; however their concentrations may vary from one sample to another [6].

Predominant source for mining and processing of these elements are REE-enriched ores. However, the extraction of REEs from these ores is not only a laborious task, but also has a significant environmental burden [7]. The aqueous byproducts or waste streams therefore appear to be an inexpensive alternative source of these critical materials. Geothermal fluids contain a variety of REEs and other valuable minerals [8, 9]. In fact, deep sea hydrothermal fluids are enriched in REEs over sea water by a factor of $10\text{-}10^3$ [10]. Produced waters from conventional oil/gas and shale gas extraction operations could be a potentially significant new source of REEs [7]. These fluids may be saline by nature and a precise determination of REEs in complex matrix samples can be a significant challenge for conventional spectroscopic techniques.

Most commonly used techniques in determination of REEs are ICP-MS (inductively coupled plasma-mass spectrometry), ICP-OES (inductively coupled plasma-optical emission spectrometry), NAA (neutron activation analysis), and XRF (X-ray fluorescence) [6]. ICP-MS and ICP-OES are very time consuming; they need tedious sample preparation/dissolution either using corrosive acids or fusion with fluxes. For direct analysis of solid samples, these techniques need to be coupled with an expensive laser ablation sampling technique [11]. NAA is a very sensitive technique but it requires

access to a nuclear reactor and long irradiation time for detection of REEs, especially direct analysis of solid samples. XRF also offers the possibility of direct analysis of solid samples. However, the technique is not suitable for lighter elements and WDXRF (wavelength dispersive-XRF) spectrometers are applied in REE determination rather than EDXRF (energy dispersive-XRF) instruments. Being larger in size, all above instruments cannot be taken to the field and samples must be brought to the lab for analysis. Moreover, in case of complex sample matrix, all these techniques suffer from interferences.

For rapid detection and analysis of rare earth elements, laser-induced breakdown spectroscopy (LIBS) can be used. LIBS is an *in situ* spectroscopic analytical technique that requires little to no sample preparation. High power laser energy is focused on the sample to be analyzed; spectral signatures of characteristic elements present in the sample are collected and analyzed to extract the necessary information. LIBS has been widely used for the detection and quantification of elements in materials irrespective of their states [12-19].

Some rare-earth elements previously have been studied by the LIBS technique [20-24]. Alamelu *et al*. determined Sm, Eu, and Gd in aqueous solutions using LIBS [20]. Quantitative LIBS analysis of doped rare earth elements (lanthanum (La) and neodymium (Nd)) in phosphors has been reported by Unnikrishnan *et al.* [21]. In addition to metallic elements, some rare earth elements (cerium, lanthanum, praseodymium, neodymium, yttrium, ytterbium, gadolinium, dysprosium, and erbium) were detected in sand by LIBS [22]. Martin *et al*. have reported an application of LIBS for quantification of some rare

earth elements in graphite matrix [23]. LIBS was used to measure the branching ratio in singly ionized neodymium [24].

In this chapter, I report application of LIBS to analyze various rare earth elements in three different types of sources; REEs in standard samples, natural geological samples, and aqueous solutions were separately studied and are reported below in parts A, B, and C, respectively.

5.3 Part A: Univariate and Multivariate Analyses of Rare Earth Elements by Laser-Induced Breakdown Spectroscopy (LIBS)

In this part, I have studied six rare earth elements: cerium (Ce), europium (Eu), gadolinium (Gd), neodymium (Nd), samarium (Sm), and yttrium (Y). This is the most comprehensive study demonstrating both univariate and multivariate LIBS analysis of rare earth elements. Varying concentrations of oxides of these elements in powder form were mixed with a balancing amount of Al_2O_3 to make a binary matrix of each element separately. From the binary mixtures, spectra were recorded to develop univariate calibration models. All six-element oxides in powder form were mixed together with Al_2O_3 to make a complex mixture for multivariate analysis.

5.3.1 Experimental Details

5.3.1.1 Experimental Set Up

The experimental set up as depicted in Fig. 5.1 was used to collect spectral signatures from the samples studied. Light of 532 nm from a frequency-doubled Q-switched Nd:YAG laser (Quantel CFR400, 20 Hz, 7-ns pulse width, 6-mm diameter, 235-mJ maximum) was focused onto the sample through a lens of focal length 30 cm and then a right-angle prism. The platform on which the sample was placed was rotated uniformly

so that consecutive laser pulses would not hit on the same spot of sample. When the plasma was generated from the sample, a pick-up lens (Ocean Optics Inc. (OOI) Part No.74-UV) which was connected to a spectrometer (Andor Technology model ME5000, 200-975 nm spectral range) via a 100-µm diameter optical fiber, collected the spectra from the plasma. The spectrograph signal was integrated with a 1024x1024 intensified charge-coupled device (ICCD) detector. The spectrograph has a digital delay generator (DDG), which was activated by the trigger from the laser Q-switch output to synchronize data acquisition with the laser pulse, and control the gate delay (GD) and gate width (GW). The spectrograph was connected to a computer for data acquisition.

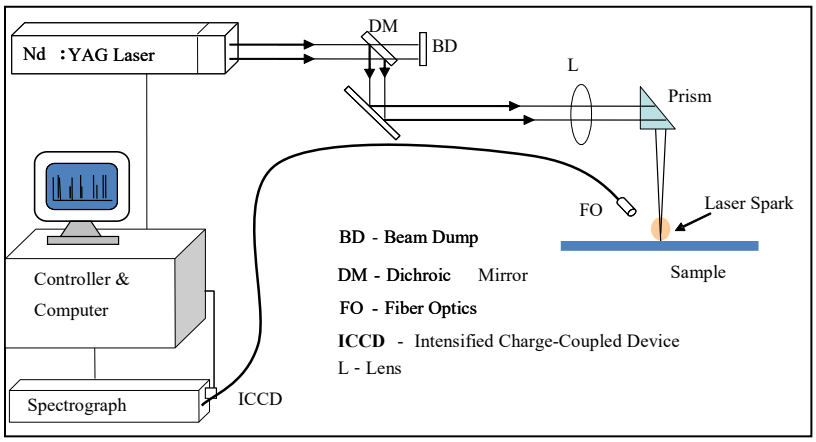

Figure 5.1 Schematic diagram of experimental set up to collect LIBS spectra from REE samples.

5.3.1.2 Sample Preparation and Experimental Conditions

Oxides of rare earth elements (REEs), CeO_2, Eu_2O_3, Gd_2O_3, Nd_2O_3, Sm_2O_3, and Y_2O_3 of 99.9% purity in powder form were used to prepare samples. Binary mixture of each rare earth element oxide with 99% pure Al_2O_3 was used as working samples to

execute univariate analysis while a complex mixture of all six rare earth elements with Al_2O_3 was used for multivariate analysis. To prepare binary mixtures, varying concentrations from 1 to 10% by weight of each element oxide were thoroughly mixed with a balancing amount of Al_2O_3 to make each sample's total weight 1g. To prepare complex mixtures, each REE oxide with concentrations from 1 to 50% (1, 3, 5, 7, 10, 15, 25, and 50) by weight were thoroughly mixed with equal amounts of all other REE oxides and Al_2O_3 to make each sample's total weight 1g. In this way, eight complex mixtures were prepared for each REE. Percentage weights of elements in their oxides are presented in Table 5.1. A small amount of about 20 mg of each sample was placed on a glass slide with double-sided tape on it and then was uniformly distributed on the slide. This slide with uniformly distributed sample was placed on the rotating platform where it interacted with the laser pulse. To obtain spectra from the samples, the optimum values of the experimental parameters (laser pulse energy, gate delays, and gate widths) were used. These experimental parameters were optimized by considering the best signal-to-noise ratio. In this experiment, 55-mJ laser pulse energy, 1-µs GD, and 5-µs GW were used to collect spectra from all the samples. The laser was operated at 2.0 Hz frequency. Each spectrum collected was an average of ten accumulations, and each accumulation was an average of ten laser shots.

Table 5.1 Weight percentage of elements (REE) in their oxides.

Oxide wt.%	Element wt.%					
	Ce	Eu	Gd	Nd	Sm	Y
1	0.814	0.864	0.867	0.857	0.862	0.787
3	2.442	2.591	2.603	2.572	2.587	2.362
5	4.070	4.319	4.338	4.286	4.312	3.937
7	5.698	6.045	6.073	6.001	6.036	5.512
10	8.140	8.636	8.675	8.573	8.623	7.874
15	12.211	12.954	13.014	12.860	12.935	11.811
25	20.352	21.590	21.689	21.433	21.559	19.686
50	40.704	43.180	43.379	42.867	43.118	39.372
100	81.408	86.361	86.759	85.735	86.236	78.744

5.3.2 Results and Discussion

5.3.2.1 Univariate Analysis

A large number of spectra were recorded on each binary mixture sample of each element oxide separately. Spectra obtained from binary mixtures of 10% concentration of each element oxide are shown in Fig. 5.2. Intensity of atomic lines of each element was taken into account for analysis and was calculated by using Andor Technology iStar software. Simple linear regression analysis (SLR) was performed on the experimental data to develop calibration models and correlation coefficient (R^2) values were determined. SLR was based on the plots of intensity (background subtracted) of the atomic lines as a function of concentration of the analyte. Since spectral peak intensities were not reliable for higher concentrations due to self-absorption, only concentrations up to 10% were used to develop calibration models.

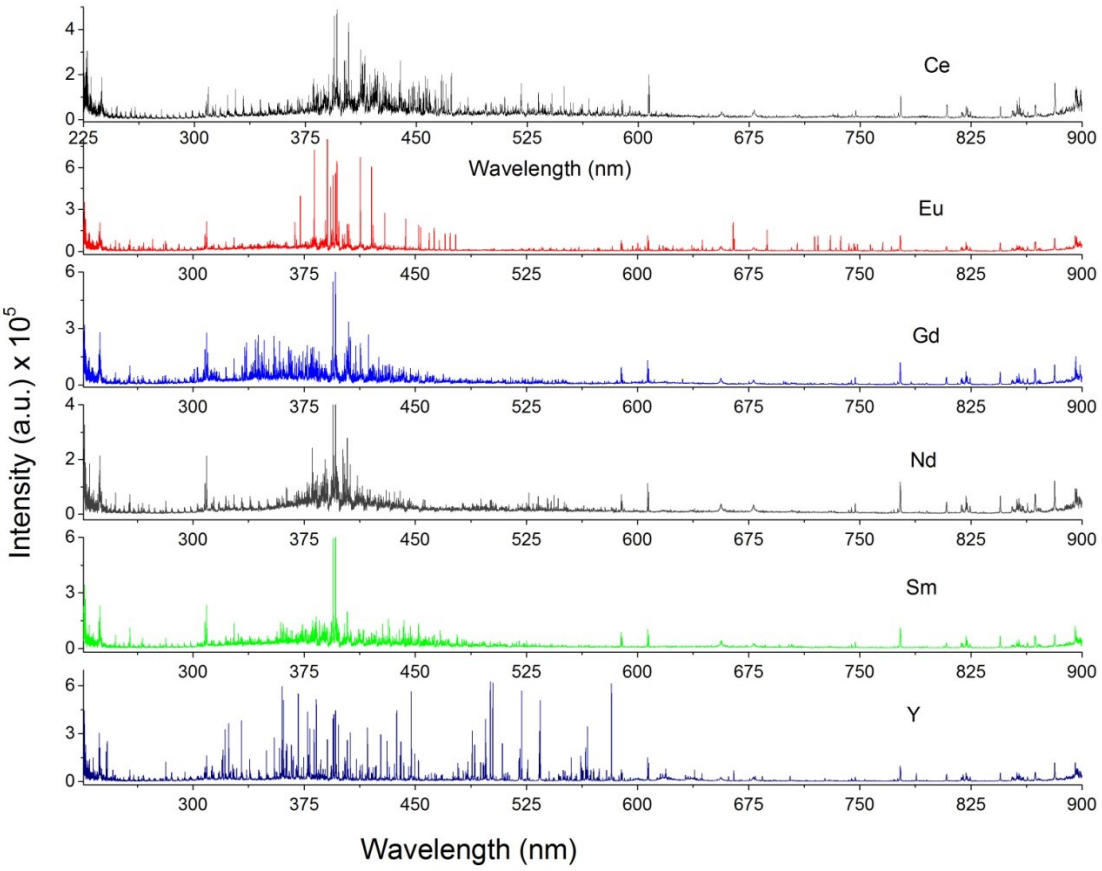

Figure 5.2 LIBS spectra obtained from binary mixture of 10% concentration of oxides of Ce, Eu, Gd, Nd, Sm, and Y.

5.3.2.1.1 Detection of Spectral Lines

With the help of NIST Atomic Database [25], many strong as well as weak emission lines were identified in the spectra obtained from each sample of binary mixture. Some of the spectral lines identified are marked in Fig. 5.3 and 5.4. These spectral peaks presented are from samples of binary mixture of 10% concentration of each element oxide separately.

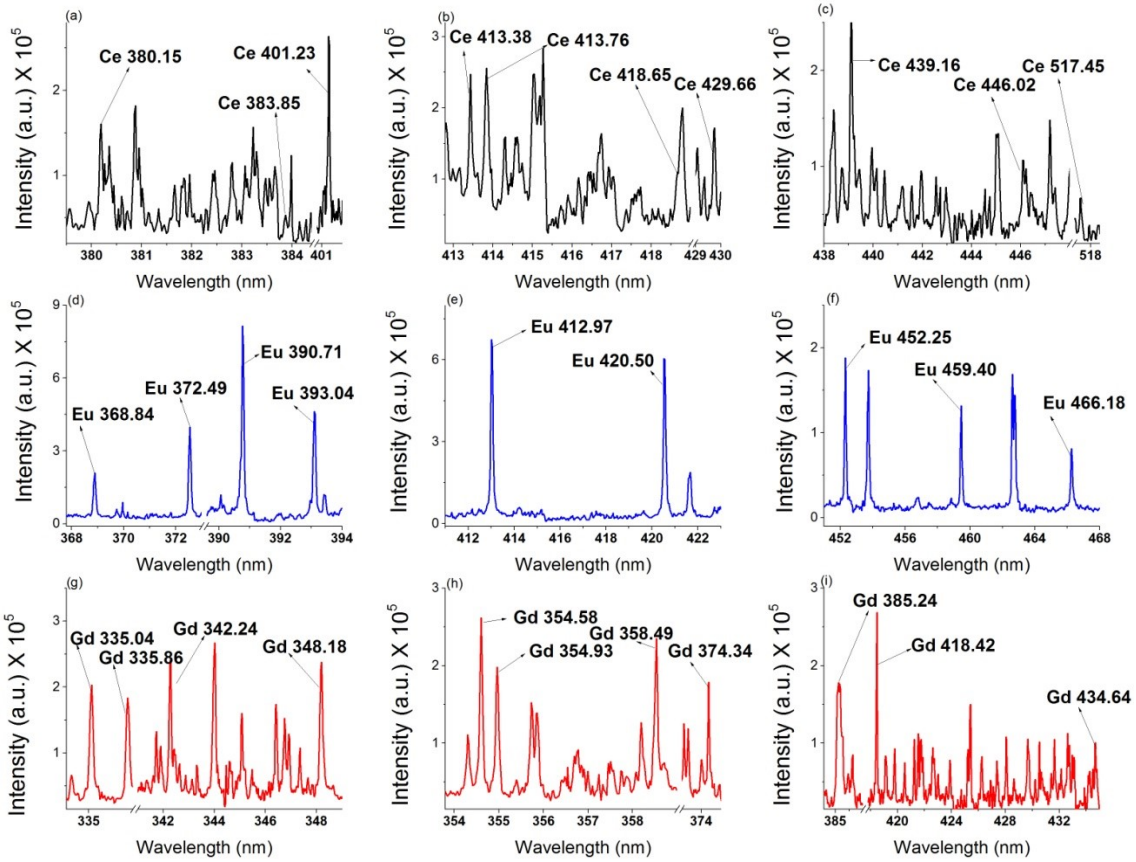

Figure 5.3 Emission lines of Ce, Eu, and Gd observed in the spectra obtained from the samples with 10% concentration of their oxides in Al_2O_3 matrix.

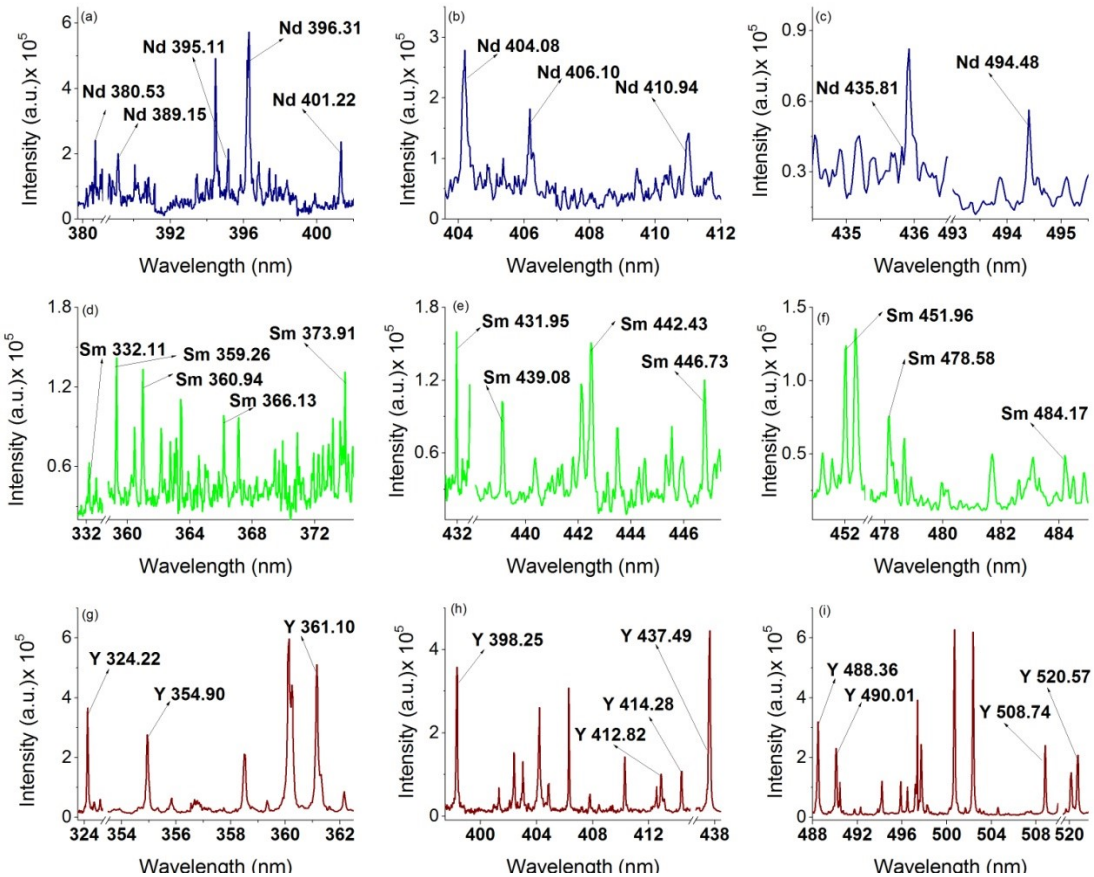

Figure 5.4 Emission lines of Nd, Sm, and Y observed in the spectra obtained from the samples with 10% concentration of their oxides in Al_2O_3 matrix.

5.3.2.1.2 Calibration Models

To develop calibration models, I selected three emission lines of each element, which were well separated and free from self-absorption. For Ce, the spectral peaks at wavelengths of 413.38, 418.65, and 439.16 nm were taken into account to develop the calibration model as shown in Fig. 5.5(a). Similarly, for Eu, peaks at wavelengths of 372.49, 390.71, and 452.25 nm; for Gd, those at 342.24, 348.18, and 418.42nm; for Nd, those at 380.53, 395.11, and 401.22nm; those for Sm at 439.08, 442.43, and 446.73 nm; and lastly for Y, peaks at wavelengths of 488.36, 490.01, and 520.57 nm were used to

plot calibration models. Calibration models are presented in Fig. 5.5. The R^2 values of all the calibration models were excellent. Hence, it shows that there is a linear relationship between intensity of spectral lines and concentration of analyte at least up to their 10% concentration. These calibration models could be useful for the estimation of REE concentrations when they are in low amount in test samples which are not complex.

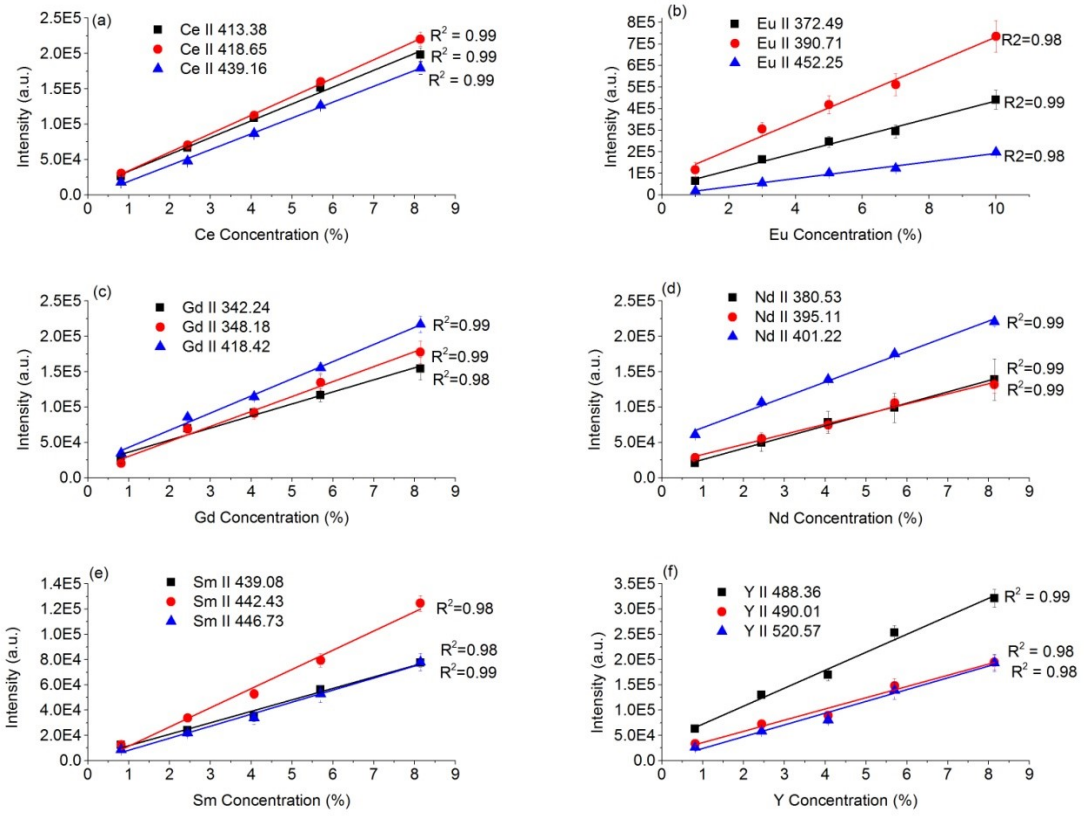

Figure 5.5 SLR - Calibration curves for (a) Ce, (b) Eu, (c) Gd, (d) Nd, (e) Sm, and (f) Y. Error bars represent the standard deviations of ten replicates.

5.3.2.1.3 Limits of Detection (LODs)

The limit of detection was calculated by using the equation

$$LOD = 3\frac{\sigma C}{I} \tag{5.1}$$

where σ is the standard deviation of the background, C/ I is the reciprocal of the slope of calibration curve. The calculated values of LOD are presented in Table 5.2.

Table 5.2 Limits of detection

Elements	LOD (wt %)
Ce	0.098
Eu	0.052
Gd	0.077
Nd	0.047
Sm	0.250
Y	0.036

5.3.2.2 Multivariate Analysis

When spectra are collected from a complex mixture of elements, the matrix effect, interference of spectral peaks of different elements, shifting of emission lines, and many other factors come into play to make the data analysis complicated. Fig. 5.6 shows a typical spectrum obtained from a mixture of six rare earth element oxides and Al_2O_3 in equal amount (14.3% each). A large number of spectral lines can be observed, but to identify and quantify emission lines of all the elements present in the spectra from the mixture is very challenging, tedious, and time consuming. Within a small range of wavelength, there could be a number of lines of different elements; it is hard to claim exactly which line corresponds to which element. In this situation, multivariate analysis could be a good alternative for quantification. It is not required to identify spectral peaks

for multivariate analysis, only wavelengths and corresponding intensities are required to plot calibration curves.

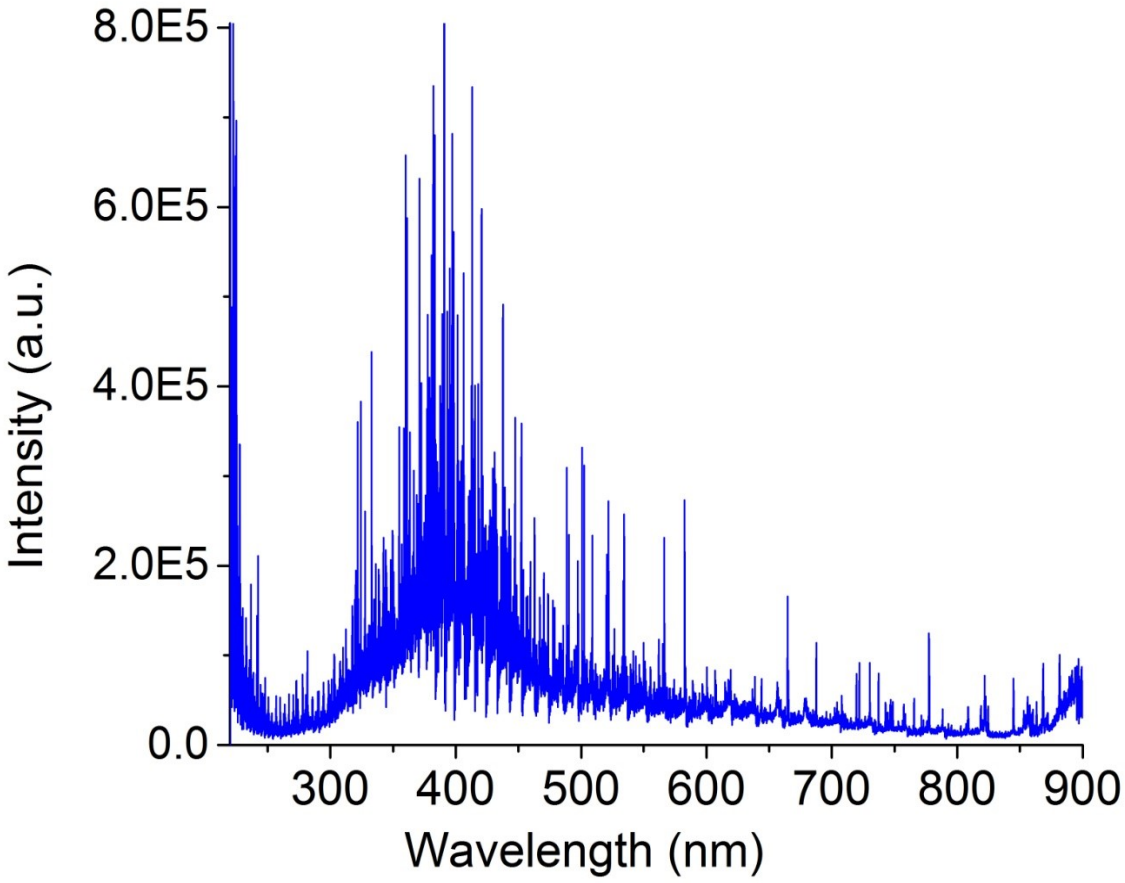

Figure 5.6 LIBS spectra from mixture of oxides of Ce, Eu, Gd, Nd, Sm, Y, and Al.

Partial least squares (PLS) is one of the multivariate analytical techniques used in chemometrics. It is very crucial to reduce the matrix effect when dealing with complex data [26]. It generates a regression model that correlates two matrices (X and Y) and finds variables in one (X) that predict variables in another (Y) [27]. So matrix X can be regarded as a set of predictors (*n* objects, *m* variables) and Y as a set of responses (*n* objects, *p* responses). Samples with known concentrations can be used to construct a

model correlating two matrices X and Y; this correlation can later be used to predict concentrations of unknown samples.

In this study, one hundred spectra were recorded from pure element oxides as well as eight complex mixtures prepared for each REE and averaged to minimize shot-to-shot fluctuation. Spectral intensities were taken as the *m* variables of predictors and concentrations as the *p* responses to obtain PLS models. Here, concentrations of elements (not of their oxides) were used in models). Xu and Schechter have suggested that better results can be obtained by selecting a proper spectral range [28]. Therefore, a reduced spectral range from the full spectrum was taken into account for PLS so that most of the strong emission lines of an element to be analyzed lie in the reduced range. The reduced wavelength ranges from 300 to 700 nm for Ce, 275 to 700 nm for Eu, 280 to 600 nm for Gd, 345 to 575nm for Nd, 325 to 530 for Sm, and 290 to 680 nm for Y were used to obtain calibration models. The Unscrambler X (version 10.3) CAMO software was used for PLS-R and Origin Software was used to plot graphs. We have taken seven components (factors) into account to obtain PLS-R plots. The explained variance illustrates how much of the total variation in X or Y is described by models including different numbers of components. Ideally, models should have large (close to 100%) total explained variance with as few components as possible. The predicted versus reference plot in PLS-R displays the predictive capacity of the developed models. Major statistics which determine the quality of the regression model are slope, offset, root mean square error (RMSE), and regression coefficient (R^2).

Explained validation variances of the analyzed elements are shown in Fig. 5.7, and calibration and validation curves are shown in Fig.5.8. The slopes, offsets, root mean

square error (RMSE), and regression coefficients for both calibration and validation sets are presented in Table 5.3. For all the elements studied, coefficients of determination (R^2) for both calibration and validation were excellent and slopes were close to one, which showed a strong correlation between predicted and reference values. Hence, it is demonstrated that PLS-R models for REE can be developed to predict the concentration of unknown samples.

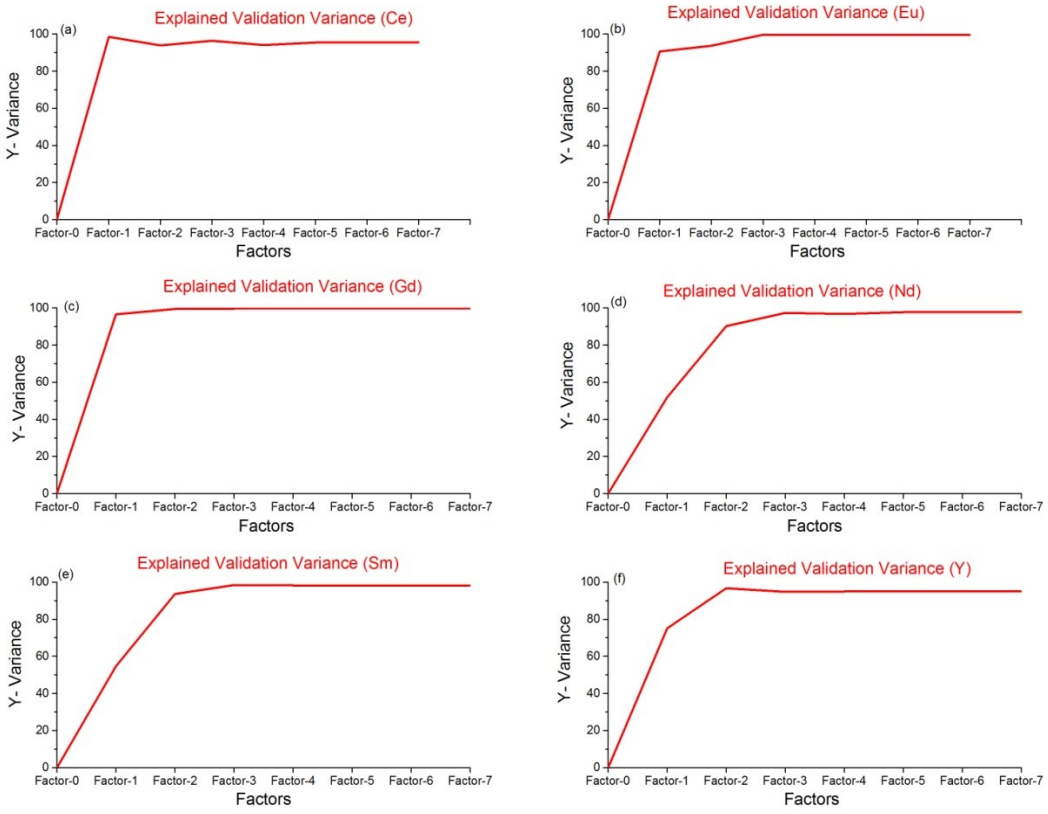

Figure 5.7 Explained validation variances for (a) Ce, (b) Eu, (c) Gd, (d) Nd, (e) Sm, and (f) Y.

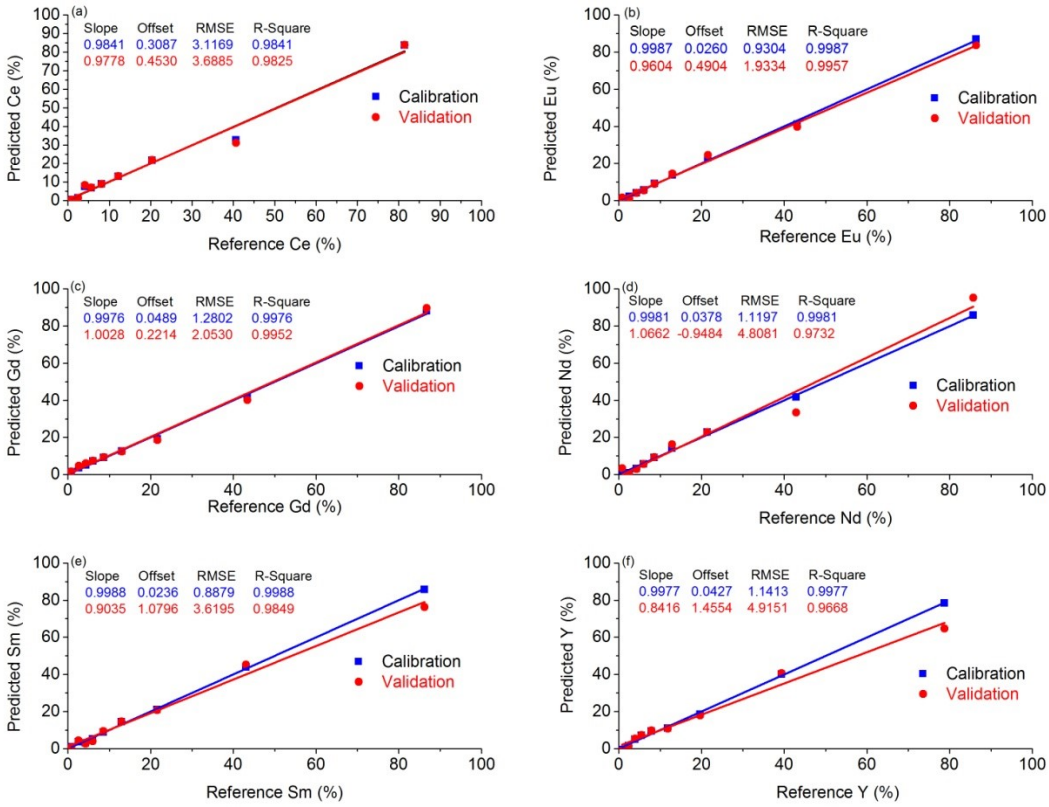

Figure 5.8 PLS-R calibration models for (a) Ce, (b) Eu, (c) Gd, (d) Nd, (e) Sm, and (f) Y.

Table 5.3 Slopes, offsets, root mean square errors (RMSE), R^2 regression coefficients for calibration and validation curves for rare earth elements.

Elements	Calibration/Validation	Slope	Offset	RMSE	R^2 values
Ce	Calibration	0.98	0.30	3.11	0.98
	Validation	0.97	0.45	3.68	0.98
Eu	Calibration	0.99	0.02	0.93	0.99
	Validation	0.96	0.49	1.93	0.99
Gd	Calibration	0.99	0.04	1.28	0.99
	Validation	1.00	0.22	2.05	0.99
Nd	Calibration	0.99	0.03	1.11	0.99
	Validation	1.06	-0.94	4.80	0.97
Sm	Calibration	0.99	0.02	0.88	0.99
	Validation	0.90	1.07	3.61	0.98
Y	Calibration	0.99	0.04	1.14	0.99
	Validation	0.84	1.45	4.90	0.96

5.3.3 Conclusions

The LIBS technique was used for univariate and multivariate analyses of six rare earth elements (Ce, Eu, Gd, Nd, Sm, and Y). Simple linear regression (SLR) - calibration models were developed by considering the selected emission lines for each element for their lower concentrations (up to 10%) in powder form. The limits of detection (LODs) for each element were calculated by using these calibration models and obtained values were 0.098, 0.052, 0.077, 0.047, 0.250, and 0.036 % for Ce, Eu, Gd, Nd, Sm, and Y, respectively. Partial least squares (PLS) was used as multivariate analytical technique for analysis of complex mixture in powder form of these rare earth elements. From PLS-regression, calibration and validation models were obtained for each element with very good correlation coefficients. Hence, this study demonstrated that analysis of simple to complex mixture of rare earth elements can be reliably performed by the LIBS technique.

5.4 Part B: Determination of Rare Earth Elements in Geological Samples by Laser-Induced Breakdown Spectroscopy (LIBS)

Laser-induced breakdown spectroscopy (LIBS) was used to detect rare earth elements (REEs) in natural geological samples. Low and high intensity emission lines of Ce, La, Nd, Y, Pr, Sm, Eu, Gd, and Dy were identified in the spectra recorded from samples to claim the presence of these REEs. Multivariate analysis was executed by developing partial least squares regression (PLS-R) models for the quantification of Ce, La, and Nd. Analysis of unknown samples indicated that the prediction results of these samples were found comparable to those obtained by ICP-MS analysis. Data support that LIBS has potential to quantify REEs in geological minerals/ores.

5.4.1 Experimental Setup

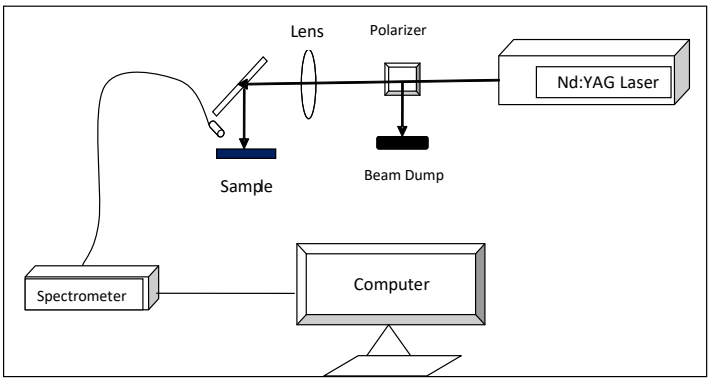

Figure 5.9 Experimental set up for LIBS

A schematic of the experimental set-up is shown in Figure 5.9. Laser pulses from a Q-switched Nd:YAG laser (TEMPEST, New Wave Research) operating at 1064-nm wavelength, 5-ns pulse duration, and 1-Hz repetition rate were focused on sample pellets placed on a uniformly rotating platform. Platform was rotated so that each laser shot would interact with fresh sample. The beam diameter of laser output was 5 mm. Argon gas was continuously supplied to the sample surface uniformly so that ablated aerosols will be swept out and created plasma would be produced in Ar atmosphere. Moreover, to provide a homogeneous Ar atmosphere around the plasma, this whole sample platform was enclosed by a small enclosure. The laser output energy was varied by means of a pair of a half-wave plate and a polarizing beam splitter cube (60:40). The pulse energy was monitored throughout the measurements using an Ophir® pyroelectric high energy sensor (PE25BF-DIF-C) and a compact Juno® USB interface connected to the computer. An N-BK7 plano-convex lens of 10-cm focal length was used to focus the laser beam onto the

sample surface at normal incidence. Plasma emission was collected through a telescope made of two UV-grade fused silica plano-convex lenses of 5-cm and 1-cm focal length, and an UV-Vis fiber optic of 1000-µm core diameter and 2-meter long (Ocean Optics). The optical fiber was connected to an Echelle spectrograph (ARYELLE 200, LTB Lasertechnik Berlin) which was coupled with a 1024×1024 intensified charge-coupled device (ICCD) camera (PI-MAX4, Princeton Instruments).

5.4.2 Sample Preparation

Eight geological samples (S1-S8) chosen from the NETL laboratory collection were dried and powdered in mortar and pestle. Part of each sample was used for ICP-MS measurement; the data are presented in Table 5.4. For LIBS analysis, pellets of 13-mm diameter were prepared using 0.5 g of powdered sample and 0.05 g of starch as binder using a Carver® bench top manual pellet press. A pressure of 6.5 tons was applied to prepare the pellets.

Table 5.4 Rare earth elements composition of geological samples determined by ICP-MS.

Samples	Concentrations (ppm)															
	Sc	Y	La	Ce	Pr	Nd	Sm	Eu	Gd	Tb	Dy	Ho	Er	Tm	Yb	Lu
S1	39	100	814	1367	118	429	55	14	51	6	28	4	12	1.4	9	1.3
S2	43	136	1103	1880	165	590	78	19	72	8	37	5	16	1.8	12	1.6
S3	71	293	1366	2193	212	740	89	22	93	11	63	11	32	3.9	24	3.2
S4	45	169	1479	2284	221	786	102	25	92	10	48	7	20	2.2	14	1.9
S5	45	196	1779	2685	265	957	126	31	113	12	59	8	23	2.5	16	2.1
S6	51	202	1794	2751	265	964	126	31	113	12	58	8	23	2.7	16	2.3
S7	44	206	1922	2861	285	1027	136	33	119	12	60	9	24	2.7	17	2.3
S8	14	750	26556	57513	7710	37833	4835	633	2552	201	711	36	199	5.1	32	3.5

For quantitative analysis, different amounts of pure oxides of Ce, La, and Nd were added to the seven samples (S1-S7) to make a wider range of concentration and the modified samples with added REEs are denoted by S1-M, S2-M, S3-M, S4-M, S5-M, S6-M, and S7-M (Table 5.5). The final concentration of Ce, La, and Nd in these samples varied in the range of 0.89-21.39, 0.85-21.46, and 0.81-17.78%, respectively (Table 5.5). No addition of REE oxides was made to the sample S8.

Table 5.5 Concentration of Ce, La, and Nd in pellets (including 10% starch as binder) prepared for quantitative analysis.

Samples	Concentration (wt %)		
	Ce	La	Nd
S1-M	0.89	0.85	0.81
S2-M	2.48	2.42	2.37
S3-M	4.05	4.00	3.93
S4-M	7.90	7.88	7.80
S5-M	10.79	10.79	10.70
S6-M	17.84	17.89	17.78
S7-M	21.39	21.46	14.22
S8	5.22	2.41	3.43

5.4.3 Results and Discussion

5.4.3.1 Qualitative Study

ICP analysis showed that all the samples except S8, had less than 0.3% (3000 ppm) concentration of each rare earth element; S8 had larger concentrations of Y, La, Ce, Pr, Nd, Sm, Eu, Gd, Dy ranging from 0.06 to 5.7 wt % (633 to 57513 ppm). Because of the low concentrations, spectral lines of rare earth elements tended to have a low intensity. Hence, spectra were recorded in an Ar atmosphere to see if intensity of the spectral lines could be enhanced. As expected, spectral peaks were found to be more intense in Ar atmosphere than in ambient air as shown in Fig. 5.10(a). The experimental parameters (gate delay, gate width, laser energy) were varied to find the best spectral signatures for most of the rare earth elements. Acquisition parameters of 2-µs gate delay (GD), 7-µs gate width (GW), and 45-mJ/ pulse laser energy were found to be the optimal conditions to observe emission lines. Since natural geological samples have a complex

matrix, the spectra obtained from these samples contained a large number of crowded and overlapping spectral peaks as shown in Fig. 5.10(b). I also recorded spectra from pure REE oxides to locate the wavelength position of different emission lines of these elements.

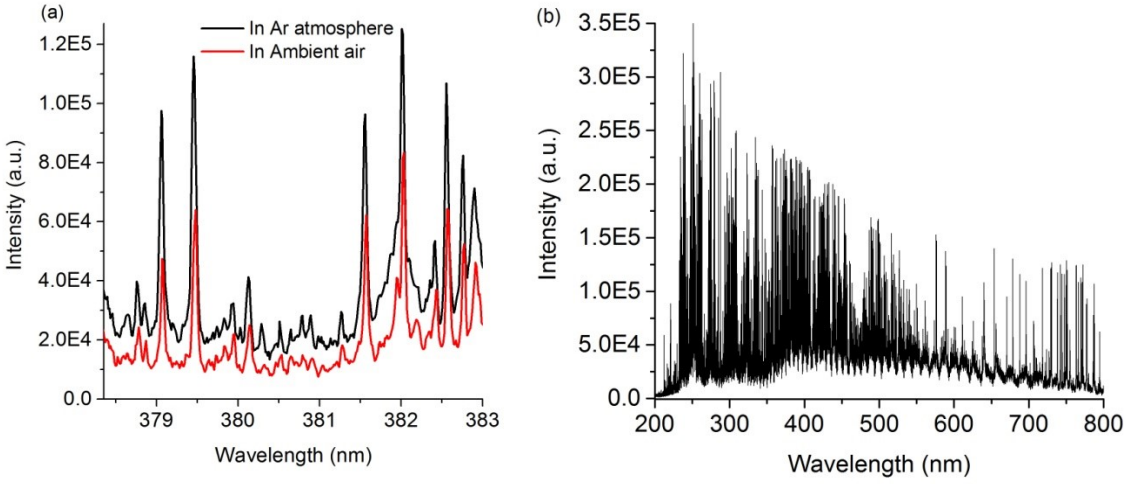

Figure 5.10 (a): LIBS spectra (in the range 377-383 nm) recorded in an Ar atmosphere and ambient air. (b): Full range (200-800 nm) LIBS spectra recorded from sample S1.

For the identification of spectral lines, we considered peaks with intensity levels higher than three times the noise (i.e., 3σ IUPAC criterion). To confirm that a peak corresponds to a particular emission line, wavelength positions given by NIST database [25] including that observed in spectra obtained from pure samples were taken as reference. Moreover, a peak was only considered if it was observed in all the ten spectra obtained from the sample with a consistent peak structure. To minimize the effect of shot-to-shot fluctuation, fifty acquisitions were averaged to get a single spectrum. I

checked for persistent emission lines of rare earth elements given by the NIST database within the wavelength range of 200 to 800 nm to identify these elements. I identified most of the persistent lines of Ce, Nd, and La in the spectra obtained from all the samples. These identified emission lines are presented in Table 5.6. In the sample S8, emission lines of Y(324.22, 354.90, 360.07, 361.10, 363.31, 371.02, 377.43, 407.73, 412.82, 417.75, 437.49, 488.36, 490.01, 508.741 nm), Pr (417.93, 420.67, 422.29, 495.13 nm), Sm (356.82, 359.26, 363.42, 369.39 , 442.43, 446.73, 447.08 nm), Eu(372.49, 381.96, 390.71, 397.19, 412.97, 420.50, 459.40, 462.72, 466.18 nm), Gd (335.04, 335.86, 342.24, 354.58, 358.49, 371.35, 374.34, 376.83, 379.63, 404.98, 405.36, 417.55, 451.96 nm), Dy (353.17, 364.53, 396.83, 404.59, 418.68 nm), Ce, Nd, and La (lines of Ce, Nd, La are presented in Table 5.6) were identified. Some of the observed emission lines are shown in Figs. 5.11 and 5.12.

Many REE emission lines were observed to suffer interferences from the major elements present in geological samples. I was not able to detect any emission lines of the elements Sc, Tb, Ho, Er, Tm, Yb, and Lu in the spectra obtained from the given samples, probably because of their low concentrations and poor resolution of the spectrometer.

Table 5.6 Identified emission lines of Ce, Nd, and La and corresponding samples in which they were detected

Identified lines	Samples in which these lines were detected
Ce I 560.12	S1, S2, S3, S4, S5, S6, S7, S8
Ce I 571.90	S2, S3, S4, S5, S6, S7, S8
Ce I 594.08	S1, S2, S3, S4, S5, S6, S8
Ce II 380.15	S1, S2, S3, S4, S5, S6, S7, S8
Ce II 413.76	S1, S2, S3, S4, S5, S6, S7, S8
Ce II 418.65	S1, S2, S3, S4, S5, S6, S7, S8
Ce II 446.02	S1, S2, S3, S4, S5, S6, S7, S8
Ce II 456.23	S1, S2, S3, S4, S5, S6, S7, S8
Nd II 378.42	S3, S6, S7, S8
Nd II 380.53	S1, S2, S3, S4, S5, S6, S7, S8
Nd II 386.34	S2, S3, S4, S5, S6, S8
Nd II 394.15	S6, S8
Nd II 395.11	S1, S2, S3, S4, S5, S6, S7, S8
Nd II 401.22	S1, S2, S3, S4, S5, S6, S7, S8
Nd II 415.60	S4, S6, S8
La I 428.02	S1, S2, S3, S4, S5, S6, S7, S8
La I 514.54	S1, S2, S3, S4, S5, S6, S7, S8
La I 521.18	S1, S2, S3, S4, S5, S6, S8
La I 550.13	S1, S2, S3, S4, S5, S6, S7, S8
La I 624.99	S3, S4, S5, S8
La II 379.08	S1, S3, S4, S5, S6, S8
La II 399.57	S1, S2, S3, S4, S5, S6, S7, S8
La II 404.29	S1, S2, S3, S4, S5, S6, S7, S8
La II 408.67	S1, S2, S3, S4, S5, S6, S7, S8
La II 433.37	S1, S2, S3, S4, S5, S6, S7, S8

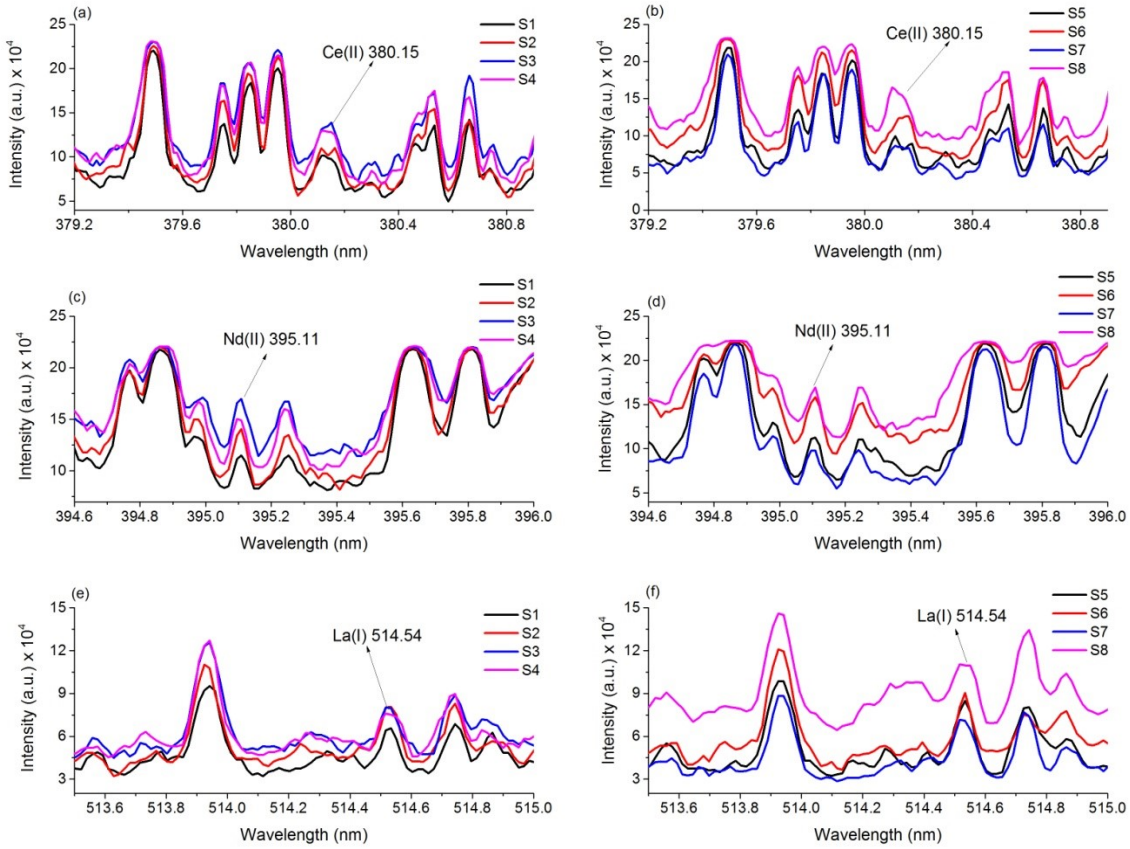

Figure 5.11 Emission lines Ce (II) 380.15, Nd (II) 395.11, and La (I) 514.54 nm observed in LIBS spectra obtained from different samples.

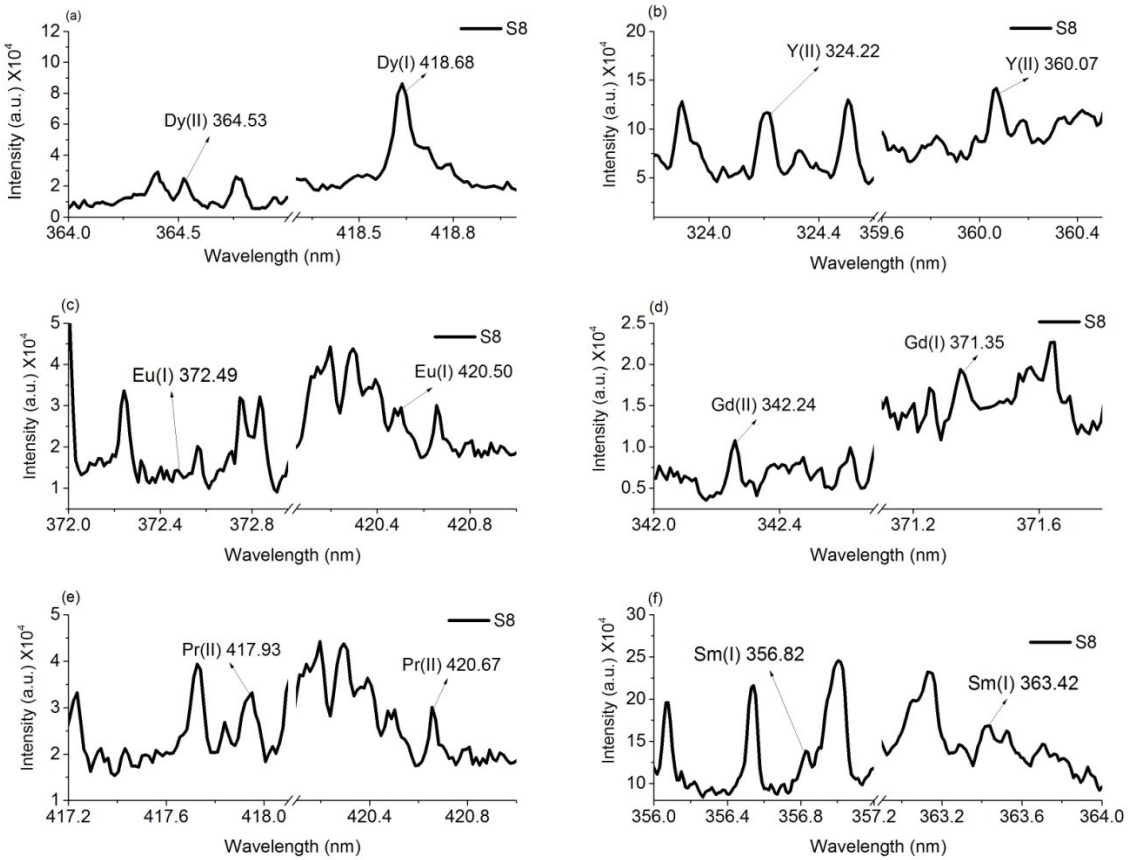

Figure 5.12 Emission lines of Dy, Y, Eu, Gd, Pr, and Sm observed in the spectra obtained from the sample S8.

5.4.3.2 Quantitative Study

As explained in section 5.4.3.1 (Qualitative Study), Ce, Nd, and La were detected in most of the samples. Therefore, these elements were selected for quantitative analysis. Except for sample S8, Ce, Nd, and La concentration varied only within a small range in all the samples; for example, Ce varies from 0.14 to 0.28% in seven samples (S1-S7), whereas sample S8 contains 5.75% Ce. Therefore, I could not expect significant difference in spectra from these seven samples to use them to develop calibration models. Hence I added varying amount of pure oxides of Ce, La, and Nd to the seven samples

(S1-S7) so that the concentration of Ce, La, and Nd varied in the range of 0.89- 21.39, 0.85 - 21.46, and 0.81 -17.78%, respectively, while the matrix remained the same. These new samples with added concentration of Ce, La, and Nd were denoted by S1-M, S2-M, S3-M, S4-M, S5-M, S6-M, and S7-M. Since these samples were complex mixtures of many elements, the matrix effect could be obvious. Therefore, multivariate analysis (MVA) was executed for quantification purposes. Partial least squares regression (PLS-R) models were developed by using Unscrambler X (Version 10.3) CAMO Software. Partial least squares (PLS) is one of the multivariate analytical techniques used in chemometrics. It helps to reduce the matrix effect when dealing with complex samples [26]. It generates a regression model that correlates the two matrices (X and Y) and finds variables in one (X) that predict variables in another (Y) [29]. So, the matrix X can be regarded as a set of predictors (n objects, m variables) and Y as a set of responses (n objects, p responses). The samples with known parameters are used to construct a model correlating two matrices X and Y, which can be later used to predict unknown parameters of other samples. The appropriate number of components (factors) can be selected to obtain PLS-R plots. The explained variance illustrates how much of the total variation in X or Y is described by models including different numbers of components. Ideally, models should have large (close to 100%) total explained variance with as few components as possible. The predicted versus reference plot in PLS-R displays the predictive capacity of the developed models. Major statistics which determine the quality of the regression model are slope, offset, root mean square error (RMSE), and regression coefficient (R^2).

In this study, spectra recorded from seven samples (S1-M to S7-M) with added concentration of Ce, La, and Nd were used to develop models and prediction capacity of those models were evaluated with the spectra obtained from the sample S8. The experimental parameters (gate delay, gate width, laser energy) were optimized by considering signal-to-noise ratio (SNR) separately for Ce, La, and Nd. The optimum laser energy was 45 mJ/pulse for the three elements, while gate delay and gate width were optimized to be 2μs and 7μs for Ce, 1μs and 7μs for Nd, and 2μs and 4μs for La.

The spectral intensities were normalized and were taken as *m* variables of predictors and concentrations were *p* responses. Better results are expected by selecting a proper spectral range [28]. Therefore, the wavelength range of 300 to 700 nm was selected for Ce, 320 to 650 nm for La, and 345 to 575 nm for Nd so that most of the strong emission lines of these elements were included. PLS-R calibration models for the elements Ce, La, and Nd were obtained by considering seven components (factors) in the Unscrambler software and later plotted in Origin software for better visualization. Explained variances and calibration-validation curves are shown in Fig. 5.13. In these figures, five spectra from each sample, which are average of fifty acquisitions, are used to obtain plots. For all three elements, very good coefficients of determination (R^2) were obtained for both calibration and validation plots.

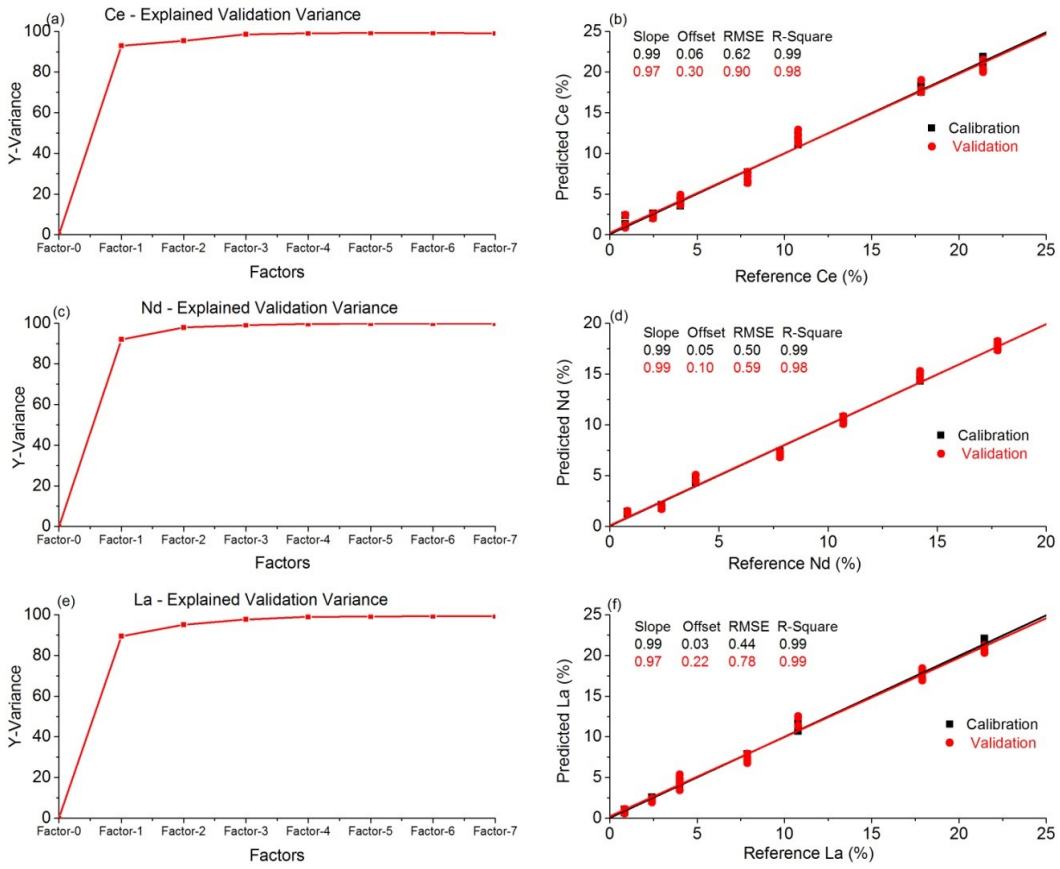

Figure 5.13 Explained validation variances and calibration-validation curves (a, b) for Ce, (c, d) for Nd and (e,f) for La.

5.4.3.2.1 Prediction Capacity of PLS-R Models

The concentration of Ce, La, and Nd in the sample S8 were predicted by using the developed PLS-Regression models. Five spectra, which were the average of fifty acquisitions individually, obtained from this sample were used for prediction and predicted values were compared with the values calculated from ICP-MS data. The results are given in Table 5.7 and presented graphically in Fig. 5.14. The relative differences were expressed in percentage where the ICP-MS values were taken as references. The values of relative differences of Ce, Nd and La concentrations were

found to be 6.7, 7.0, and 12.9 wt % respectively. Overall, it had demonstrated that the regression models can be produced and can be used to predict concentration of REEs in unknown samples.

Table 5.7 Concentrations of Ce, Nd, and La obtained by ICP-MS and LIBS.

Analyte	Concentration (wt %)		Relative difference (%)
	ICP-MS	LIBS	
Ce	5.22	5.58	6.76
Nd	3.43	3.19	7.09
La	2.41	2.72	12.95

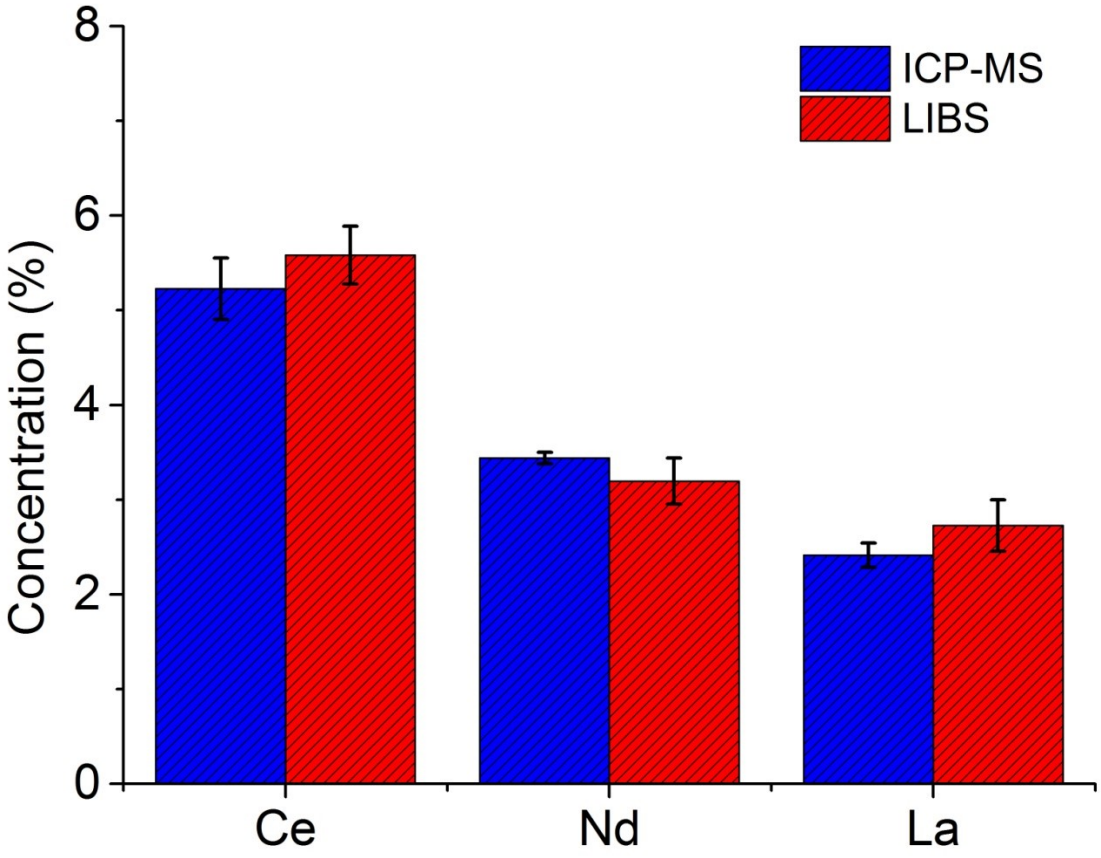

Figure 5.14 Graphical comparison of concentrations of Ce, La, and Nd calculated by ICP-MS and LIBS.

5.4.4 Conclusions

Different emission lines of rare earth elements were identified in the spectra obtained from natural geological samples, which confirmed the presence of those elements in corresponding samples. Ce, La, and Nd were detected in all the samples. Pr, Sm, Eu, Gd, and Dy were detected only in S8. Quantification of Ce, La, and Nd was performed by multivariate analysis. PLS- Regression models were developed by using the Unscrambler software where seven samples were used to produce models and these models were used to predict the concentration of Ce, Nd, and La in a separate sample taken as an unknown. Prediction results were found to be comparable to those obtained by ICP-MS analysis. The study indicates that the LIBS can be a potential technique for the detection and quantification of rare earth elements in geological samples.

5.5 Part C: Measurement of Eu and Yb in Aqueous Solutions by Underwater Laser-Induced Breakdown Spectroscopy (LIBS)

Two rare earth elements (Eu and Yb) were studied by using their solutions to obtain underwater LIBS spectra. To the best of our knowledge LIBS has not yet been used for the determination of any of the REEs in liquid samples by generating a direct spark inside the liquid. Alamelu *et al*. [20] have applied LIBS for the determination of Sm, Eu, and Gd in aqueous solution, however, LIBS spectra were not produced in liquids. They converted liquid solutions of these REEs into a solid substrate by filtration and evaporation, which was then used to collect LIBS spectra. Likewise, an application of LIBS for selective determination of Eu_2O_3 and $Eu(OH)_3$ colloids is reported by Yun *et al.* [30]. They have reported the solubility product of $Eu(OH)_3$ as a function of pH in addition to the spectroscopic features and detection sensitivity of Eu. The detection of

Eu^{3+} along with some other metal ions and colloidal suspension of Eu_2O_3 particles in aqueous solution by LIBS is explained by Bundschuh *et al*. [31]

Some strong emission lines were detected in the spectra and calibration models were developed by varying their concentrations from 500 ppm to 10,000 ppm. Temporal evolution of plasma and the effect of laser pulse energy and pressure on the plasma emission were studied. This study indicates the potential of LIBS for direct analysis of liquids for REEs. The developed technique could be useful for *in situ* determination of REEs in waste streams and can potentially be applied for real time monitoring in the REE processing plants.

5.5.1 Experimental Set-up and Samples

The experimental arrangement used for the underwater LIBS study of Eu and Yb at elevated pressure is shown in Figure 5.15. A Q-smart pulsed Nd: YAG laser (Quantel laser 450 mJ) controlled by the Q-Touch pad was used as an excitation source for laser-induced emission from REE solutions. The laser was operated at its fundamental wavelength of 1064-nm with a 6-ns pulse duration and a repetition rate of 10-Hz. The experimental solution was kept in a 0.5-liter stainless-steel high-pressure vessel (Thar Technologies Inc.) using a precision metering pump (QX-6000, Ametek Inc.) It has two sapphire windows of 22-mm diameter and 12.7-mm thickness. The pump was set to constant pressure mode so that it automatically injected or withdrew CO_2 as per requirement. The CO_2 used was an industrial grade gas contained in a high-pressure industrial cylinder. The laser beam was focused 2 cm inside the solution through a sapphire window by an air-spaced doublet (focal length 50 mm). Emitted light from the plasma was collected in a confocal manner via the same sapphire window while another

window was used to observe the created plasma. The laser output energy was varied by means of a pair of a half-wave plate and a polarizing beam splitter cube (50:50). The pulse energy was monitored throughout the measurements using an Ophir® pyroelectric high energy sensor (PE25BF-DIF-C) and a compact Juno® USB interface connected to the computer. The plasma emission was collected by a long-pass dichroic mirror (DMLP900, Thorlabs) and two UV-grade fused-silica plano-convex lenses (focal length 50 and 10 mm) and was carried to a Czerny-Turner spectrograph (Shamrock SR303i-A, Andor Technology) via optical fiber (SR-OPT-8014, Andor Technology). Time-resolved detection of the dispersed light was carried out using an intensified charge-coupled device (ICCD) camera (DH320T-25F-03, Andor Technology).

Solutions of Eu (10017±29 µg/mL Eu, 7% HNO_3) and Yb (9978±27 µg/mL Yb, 7% HNO_3) (Inorganic Ventures) were separately used as working samples in this study. These samples were diluted with deionized water containing 2% HNO_3 to obtain the desired concentrations. HNO_3 was used to prevent precipitation from the solution. The samples with 4000 ppm concentrations were used to study the plasma evolution and effect of energy on plasma for both Eu and Yb while concentrations were varied in the range of 500-10,000 ppm for generating the calibration curves. A 120-mL sample solution was used for each measurement.

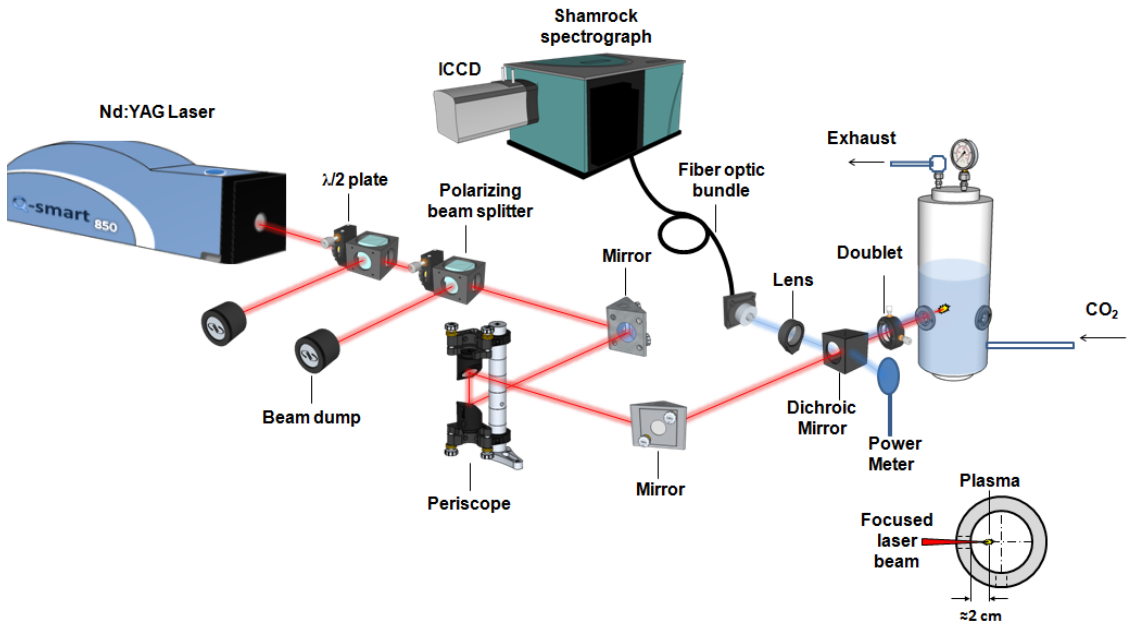

Figure 5.15 LIBS experimental set-up for liquid samples.

5.5.2 Result and Discussion

5.5.2.1 Detection of Emission Lines

When an incident laser pulse energy exceeds the breakdown threshold, laser induced breakdown of fluid occurs and emission from free electrons and electron-ion recombination produce a broadband plasma emission [32]. Compared to air, plasma produced in liquid is cooled much faster by Bremsstrahlung emission, thermal conduction, and shockwaves [32, 33]. Consequently, acquisition of underwater LIBS spectra is very critical. Moreover, the emission signal from within a liquid sample is very weak compared to that from plasmas created on a liquid surface.

Here, spectra were recorded from Eu solution and Yb solution separately at six different pressures (ambient, 50, 100, 150, 200, 250 bars) and various experimental parameters (laser energy, gate delay, gate width). The spectrometer was calibrated

according to dichroic mirror used for plasma emission collection, which showed the spectral window of wavelength range of 375-515 nm. Within the spectral window of the spectrometer (375-515nm), three neutral (459.40, 462.72, 466.18 nm) and seven ionic (381.96, 390.71, 393.04, 397.19, 412.97, 420.50, 443.55 nm) emission lines of Eu and one neutral line (398.79 nm) of Yb were detected at all the pressures taken into consideration within a certain range of experimental parameters. Spectra recorded from 4000 ppm concentrations of each of Eu and Yb are shown in Figure 5.16(a, b); the gate delay and laser energy were 50 ns and 20 mJ, respectively, for both Eu and Yb while gate widths were 500 and 600 ns respectively for Eu and Yb. Again, when spectra were recorded from the mixture of Eu and Yb solution samples at ambient and high (200 bar) pressures using gate delay 50 ns, laser energy 20 mJ, and gate width 500 ns, all the emission lines observed in the spectra taken from their separate solutions were detected as shown in Figure 5.16(c). To confirm the wavelength positions of emission lines, NIST atomic Database [25] was taken as reference. Spectroscopic data of these observed emission lines of Eu and Yb are presented in Table 5.8. Detection of these emission lines showed that the LIBS technique could be used for the *in situ* identification of REEs in liquid sources at low as well as high pressures.

I mentioned above the detection of emission lines of Eu and Yb at various pressures, but this is possible only when proper experimental parameters are used. Moreover, the intensity and intensity profile of emission lines were found to depend significantly on the laser pulse energy and gate delay. For accurate and precise analysis of REEs in liquid by LIBS, it is important to study the effects of different experimental

conditions on LIBS spectra. Dependence of emission spectra on gate delay, laser energy, and pressure are separately discussed in following sections.

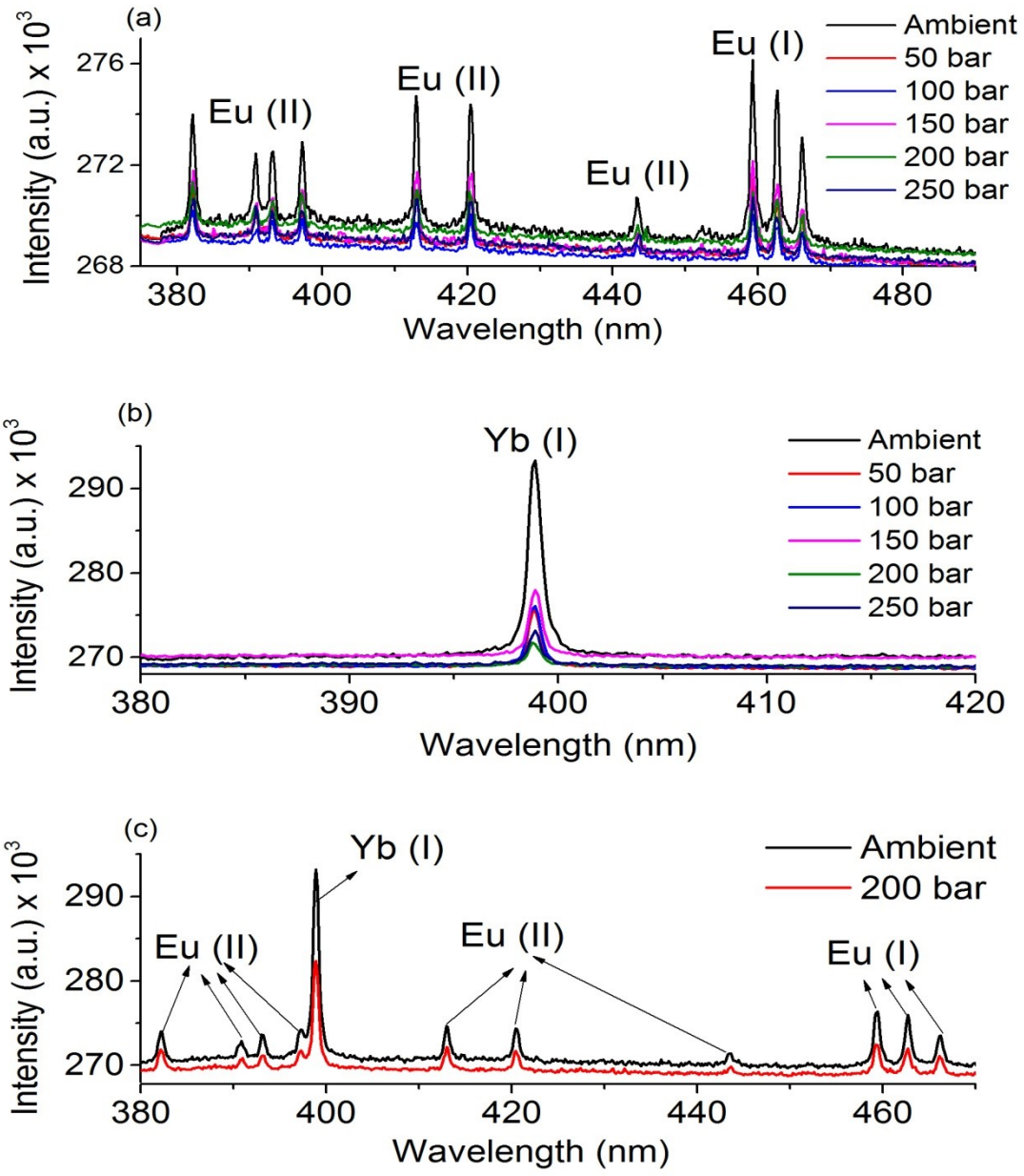

Figure 5.16 Emission lines of Eu and Yb identified in the spectra obtained from (a) 4000 ppm Eu solution (b) 4000 ppm Yb solution (c) solution of Eu and Yb with 4000 ppm concentration of each.

Table 5.8 Spectroscopic data of the spectral lines of Eu and Yb identified in the spectra. The wavelength (λ), lower and upper energy ($E_i - E_j$) and statistic weight ($g_j - g_j$) of the transition levels, and probability for spontaneous emission (A_{ij}) are indicated [25]

Species	λ_{ij} (nm)	$E_i - E_j$ (cm^{-1})	A_{ij} (10^8 s^{-1})	$g_i - g_j$
Eu II	381.967	0.00-26172.83	1.27	9-11
Eu II	390.710	1669.21-27256.35	1.37	7-5
Eu II	393.048	1669.21-27104.7	1.07	7-7
Eu II	397.196	1669.21-26838.50	0.89	7-9
Eu II	412.970	0.0-24207.86	0.68	9-9
Eu II	420.505	0.0-23774.28	0.71	9-7
Eu II	443.556	1669.21-24207.86	0.31	7-9
Eu I	459.403	0.0-21761.26	1.61	8-10
Eu I	462.722	0.0-21605.17	1.56	8-8
Eu I	466.188	0.0-21444.58	1.52	8-6
Yb I	398.799	0.0-25068.222	1.92	1-3

5.5.2.2 Time-Resolved Analysis of Plasma Emission

Laser induced plasma in liquid solution cools down much faster than in normal atmosphere. Because of transient plasma emission, gate delay (GD), the time gap between plasma emission and data recording have a crucial role in detecting spectral peaks of elements in aqueous media. To study the effect of gate time delay on spectra acquisition of Eu and Yb, spectra from their separate solutions of 4000 ppm concentrations were obtained at different gate time delays (1-300 ns) over the range of pressure from ambient to 250 bars. Gate widths of 500 ns and 600 ns, respectively were used for data acquisition of Eu and Yb while laser energy of 20 mJ was used for both. At shorter gate delays (≤ 60 ns), all the Eu lines (381.96, 390.71, 393.04, 397.19, 412.97, 420.50, 443.55, 459.40, 462.72, 466.18 nm) mentioned above were observed at all the pressures (ambient, 50, 100, 150, 200, 250 bars), while their detection seemed to depend on pressure at longer gate delays. Similarly, Yb line (398.79 nm) was observed until 150

ns of gate delay at all the pressures and its detection depended on the pressure when gate delays were longer.

For better understanding, the behaviors of two emission lines of Eu (420.50 and 459.40 nm) and one line of Yb (398.79 nm) at various gate delays and pressures were studied. Fig. 5.17. shows the histogram showing the gate time delay up to which these emission lines were detected at various pressures.

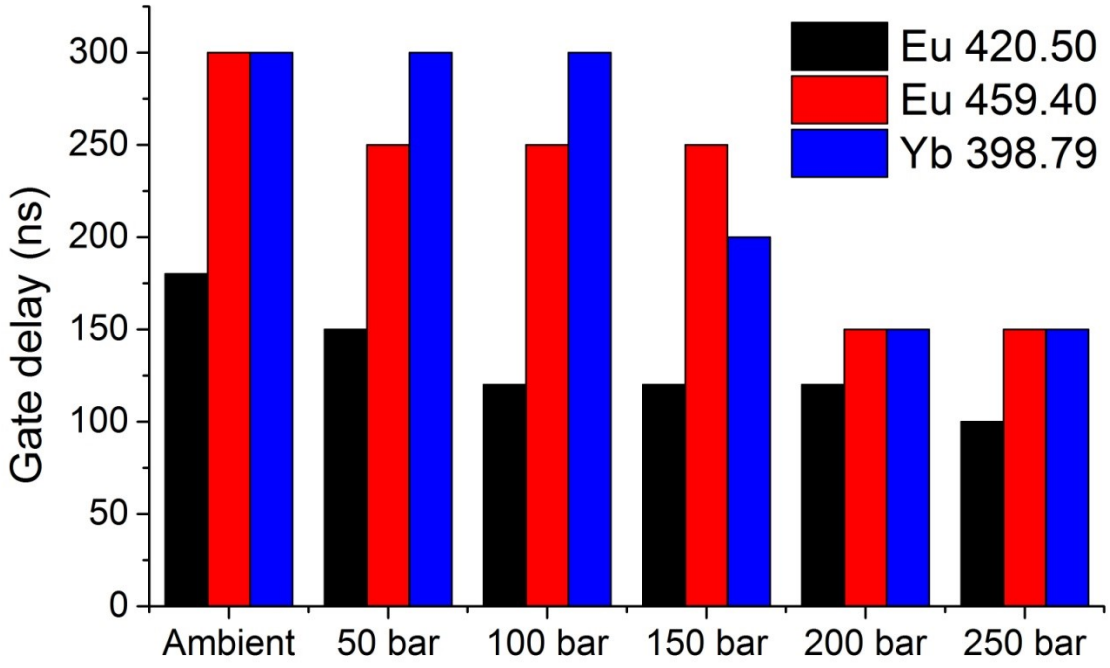

Figure 5.17 Histogram showing the gate time delay up to which spectral lines of Eu and Yb were detected at various pressures.

At ambient condition, the Eu (II) 420.50-nm line was observed up to the gate delay of 180 ns, while it was observed up to 150 ns at 50 bars, and up to 120 ns at higher

pressures (100, 150, 200 bars), and it disappeared after 100 ns when the pressure was 250 bars. Compared to the Eu (II) 420.50-nm (ionic) line, the Eu (I) 459.40-nm (neutral) line was observed for longer gate delays. At the least at the pressure taken into account (ambient), Eu (I) 459.40 nm was detected up to 300 ns, while it was detected up to 250 ns at pressures of 50, 100, and 150 bars, and it disappeared after 150 ns when the pressure was 200 and 250 bars. Similarly, Yb (I) 398.79 nm was detected up to 300ns at lower pressures (1-100 bars), up to 250 ns at 150 bars, and up to 150 ns at elevated pressures of 200 and 250 bars. This probably indicates the reduction in lifetime of emission lines at elevated pressures and the pressure has effect on plasma emission at its late stage of evolution. When intensities (background subtracted) of all these three lines were plotted as a function of gate delays, exponential decrease in intensities was found with the increase in gate delays at all the pressures taken into account as shown in Figure 5.18. Overall, it can be suggested that as pressure increases, lifetime of emission lines decreases or pressure has effect in detection at later times of plasma emission.

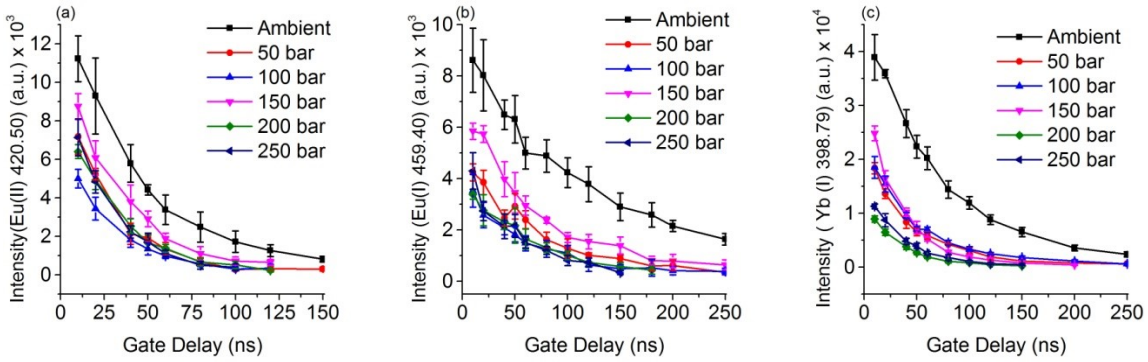

Figure 5.18 Variation of spectral intensity with gate delay for (a) Eu(II) 420.50 nm (b) Eu(I) 459.40 nm, and (c) Yb (I)398.79 nm. Error bars represent the standard deviations of five replicates.

5.5.2.3 Effect of Laser Energy in Plasma Emission

The effect of laser pulse energy on intensity of Eu and Yb emission lines was investigated by analyzing several spectra recorded over an energy range 4-100 mJ/pulse at six different pressures (ambient, 50, 100, 150, 200, 250 bars). Separate solutions of Eu and Yb with their concentration of 4000 ppm each were used as samples. Gate delay time of 50 ns and gate width of 500 ns for Eu and 600 ns for Yb were used to obtain data. Both the neutral (459.40, 462.72, 466.18 nm) and ionic (381.96, 390.71, 393.04, 397.19, 412.97, 420.50, 443.55 nm) lines of Eu and a neutral (398.79 nm) line of Yb were detected. Dependence of intensity of two Eu lines and one Yb line on laser energy at different pressures is presented in Fig. 5.19.

Neutral line (Eu (I) 459.40 nm) and ionic line (Eu (II) 420.50nm) of Eu were found to have an almost similar trend of increase of their intensity with laser energy except a slight decrease of intensity of neutral line at low values of energy for higher pressures (100, 150, 200, 250 bars) as shown in Fig.5.19 (a),(b).

Intensity of Yb (I) 398.79 nm was also found to increase almost linearly with an increase in laser energy at lower pressures (ambient, 50, 100 bars). At higher pressures (150, 200, 250 bars), intensity increased linearly with energy up to 40 mJ and then was almost constant for higher energy as shown in Fig. 5.19(c). Michel *et al*. [34] have reported increase in intensity of selected lines of Ca, Li, and Na, with the increase in energy until it reaches maximum and after reaching maximum, it decreases. This trend is supported by the results of Ca and K lines presented by Hou *et al*. [35]. However, the Mn triplet is reported to show the gradual decrease in its intensity with the increase in laser energy in [34]. These studies were also performed by creating underwater laser spark.

Comparing these reported studies with my results, it can be estimated that the effect of laser energy on intensity of spectral lines may depend on the elements, analyte lines, and experimental conditions.

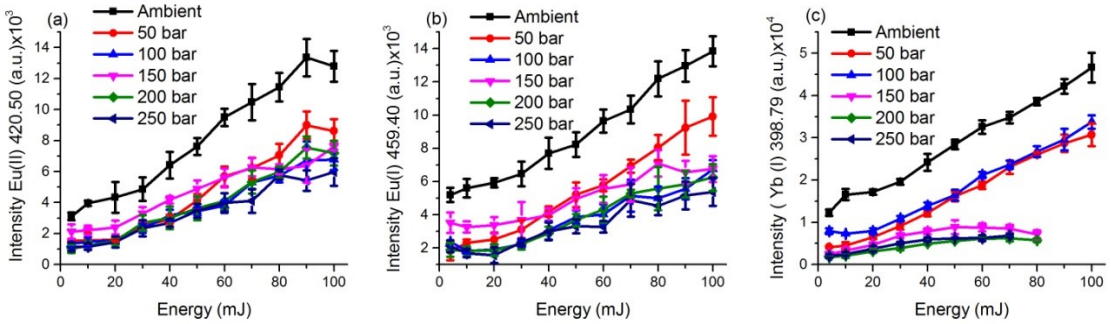

Figure 5.19 Effect of laser energy on the intensity of (a) Eu (II) 420.50, (b) Eu (I) 459.40, and (c) Yb (I) 398.79 nm at different pressures. Error bars represent the standard deviations of five replicates.

It is reported that higher laser energy causes adverse effects like plasma shielding and moving breakdown along the laser beam pathway [32]. Therefore, it is reasonable to apply moderate energy for underwater LIBS applications.

5.5.2.4 Pressure Effect on Emission Spectra

To study the effect of pressure on emission spectra, variation of intensity (background subtracted), area under curve (AUC), and width (FWHM) of spectral lines of Eu and Yb with pressure ranging from ambient to 250 bars was investigated. Spectra were recorded from 4000 ppm concentration of both Eu and Yb separately at three gate delays (20, 50, 100 ns), six different pressures (ambient, 50, 100, 150, 200, 250 bars), and gate widths were 500 ns for Eu and 600 ns for Yb. Two emission lines (Eu (II) 420.50 nm

and Eu (I) 459.40 nm) of Eu and one line (Yb (I) 398.79 nm) of Yb were taken in to consideration for the study.

Figures 5.20(a), (b), and (c) show the variations of intensity, AUC, and FWHM of Eu (II) 420.50 nm with pressure. Intensity and AUC decreased in similar fashion when pressure was elevated from ambient to 50 bar of CO_2 pressure at all the gate delays (20, 50,100 ns). For the further increase in pressure, both the intensity and AUC appeared to be almost independent of pressure. Width of the line seemed to be apparently impervious to pressure except its increase when pressure reached to 50 bars from ambient condition at gate delay of 100 ns. Behavior of neutral line Eu (I) 459.40 nm with pressure was similar to that of ionic Eu (II) 420.50-nm line; however, its width was almost unaffected by pressure at all three gate delays as shown in Figure 5.20 (d), (e), and (f).

Intensity and AUC of the Yb (I) 398.79-nm line were observed to decrease sharply when pressure was raised to 50 bars at all three gate delays (20, 50, 100 ns) as shown in Figure 5.20(g), (h). They were almost constant in the range of 50-150 bars, slightly decreased at 200 bars and then again were independent of pressure when gate delays were 20 and 50 ns. For gate delay of 100 ns, they were unaffected by pressure in 50-250 bars range. FWHM of the Yb (I) 398.79-nm line was observed to be almost independent of pressure at all three gate delays. Apparently, intensity and AUC of all three lines appeared to be more sensitive to pressure at lower gate delay (20 ns) compared to 50 and 100 ns, especially in the range of ambient to 100 bars.

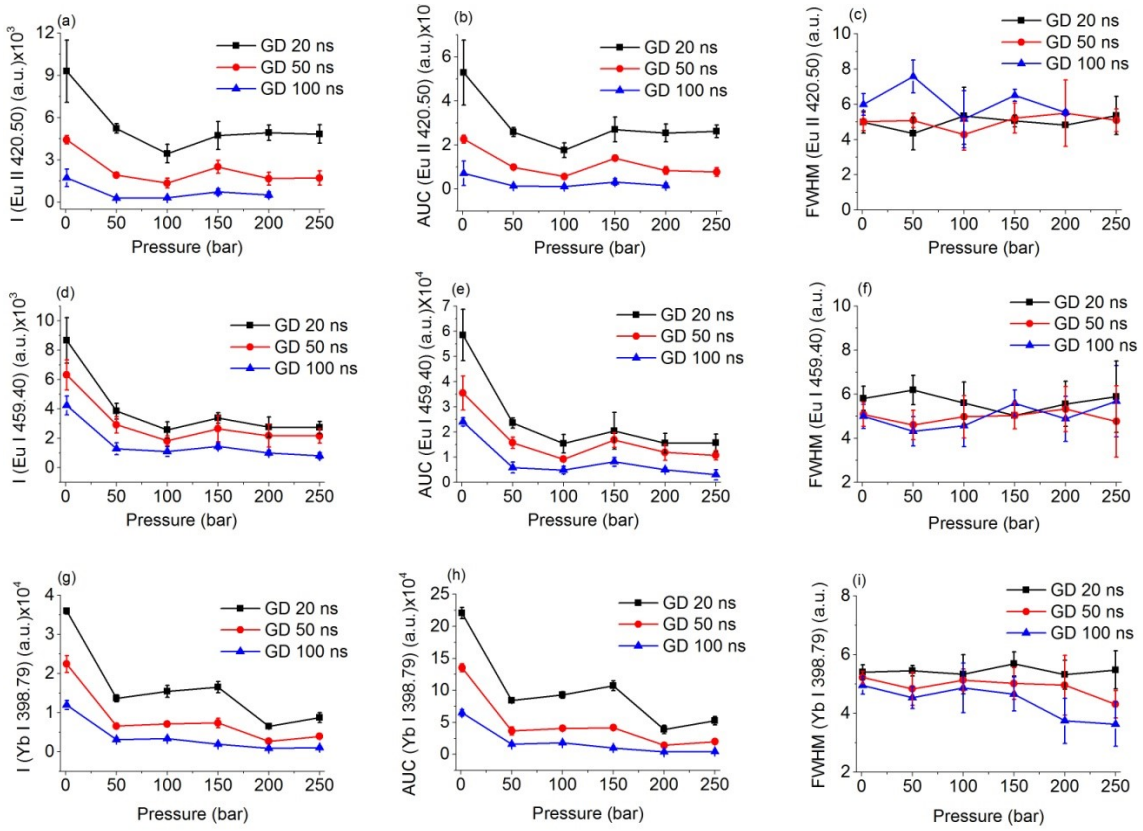

Figure 5.20 Influence of CO_2 pressure on intensity, area under curve (AUC), and FWHM of Eu and Yb spectral lines. Error bars represent the standard deviations of five replicates.

These observations suggest that the CO_2 pressure has an effect in the beginning when CO_2 is injected into the solution, which was initially at ambient conditions. It can be estimated that dissolved CO_2 confines the plasma and emission intensity is reduced due to plasma shielding. After dissolving of CO_2 into the solution, increase in its pressure has a very weak effect in the plasma emission. Similar observations of weak effect of pressure on Ca, Na, and Zn emission are reported by Michet *et al.*[34] and Thornton *et al.* [36]. As the liquid is almost incompressible, its density and thermal conductivity should

be unaffected by increasing pressure, which will keep the plasma expansion volume and degree of ionization nearly constant.

5.5.2.5 Calibration Models

To develop calibration models, eight sample solutions were prepared by using varying concentrations of Eu and Yb from 500 ppm to 10,000 ppm separately. Spectra were recorded from these samples using optimized experimental conditions at ambient conditions. Laser energy of 20 mJ and gate delay of 50 ns were used for both Eu and Yb while the used gate widths were different: 500 ns was used for Eu and 600 ns for Yb. To minimize the effect of shot-to-shot fluctuation, 500 acquisitions were averaged to get a single data point and measurements were repeated for five times. The standard deviations of these five measurements are reflected as error bars in the calibration plots. Two strong spectral lines of Eu [Eu (I) 459.40 nm and Eu (II) 420.50 nm] and one line of Yb [Yb (I) 398.79 nm] were considered for producing calibration curves. Background subtracted intensity of emission lines were plotted as a function of analyte concentration. For both Eu and Yb, linear relationship of intensity of emission lines with the concentration was obtained as shown in Fig. 5.21. The regression coefficient values of the linear fit were near unity for all three lines taken into consideration. These calibration curves can be used for quantitative analysis of REE in an aqueous solution.

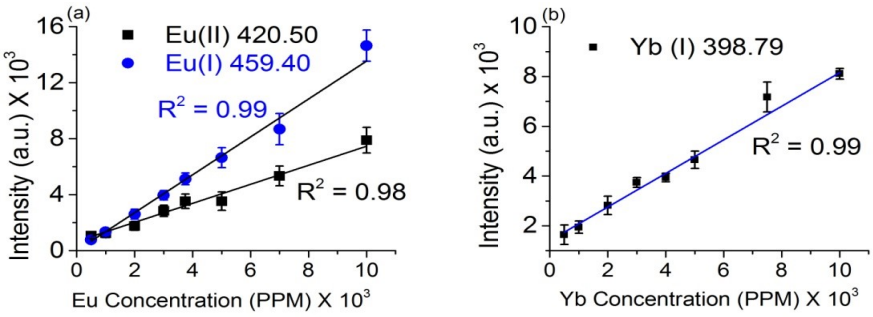

Figure 5.21 Calibration curves (a) for Eu lines, (b) for Yb line.

5.5.2.6 Limits of Detection (LOD)

Limits of detection for Eu and Yb were estimated by using an equation

$$LOD=3\sigma\frac{C}{I} \tag{5.2}$$

where σ is standard deviation of the background, C is the minimum concentration used in calibration curve, and I is intensity of emission line. For Eu, LOD was estimated to be 256 ppm by using neutral line (Eu (I) 459.40 nm) and 209 ppm by using ionic line (Eu (II) 420.50 nm). For Yb, it was estimated to be 156 ppm, which is slightly lower than the LODs of Eu.

5.5.2.7 Plasma Temperature and Electron Density Measurements

5.5.2.7.1 Temperature

The plasma temperature was determined by the Boltzmann plot method. Assuming the plasma is in local thermodynamic equilibrium (LTE) conditions and optically thin, the intensity of emitted radiation (I_{ik}) is given by [37, 38]

$$I_{ik} = NA_{ik}\frac{hc}{4\pi\lambda_{ik}}\frac{g_i}{U(T)}exp\left(-\frac{E_i}{k_BT}\right) \tag{5.3}$$

where N is the total population density, A_{ij} is coefficient of transition probability, g_i is the

statistical weight factor or degeneracy, U(T) is the partition function of the species, E_i is the energy of upper level of transition, and k_B is the Boltzmann's constant.

Taking the natural log on both sides of Equation (5.3) and solving,

$$ln\left(\frac{I_{ik}\lambda_{ik}}{g_i A_{ik}}\right) = \left(-\frac{1}{k_B T}\right) E_i + ln\left(\frac{Nhc}{4\pi U(T)}\right) \quad (5.4)$$

When the term on the left-hand side is plotted against E_i, it yields a linear plot known as the Boltzmann plot. The slope $-1/k_BT$ was used to determine the temperature T. Five emission lines Eu (II) (390.71, 393.04, 397.19, 412.97, 420.50 nm) were used to plot Boltzmann plot as shown in Fig. 5.22 and temperature was estimated to be 5000 K for Eu. Since only one line of Yb was detected, plasma temperature for Yb could not be estimated.

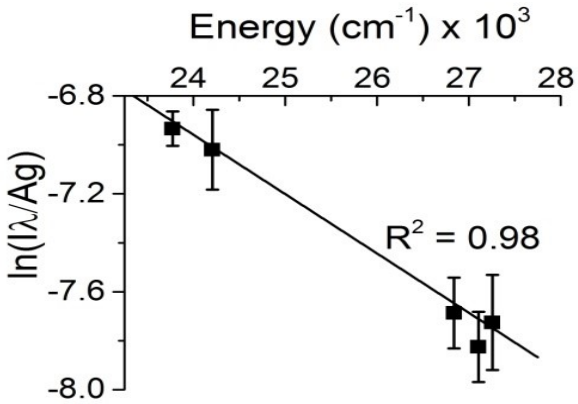

Figure 5.22 Boltzmann plot for Eu.

5.5.2.7.2 Electron Density

For the estimation of electron density, the Saha- Boltzmann equation was used, which is given as [38-40]

$$n_e = \frac{I_z^*}{I_{z+1}^*} 6.04 \times 10^{21} (T)^{3/2} \times exp\left[\frac{-E_{k.z+1} + E_{k,z} - \varkappa_z}{k_B T}\right] \quad cm^{-3} \qquad (5.5)$$

where $I_z^* = I_Z \lambda_{ki,z} / g_{k,Z} A_{ki,Z,}$ I_Z is intensity of spectral line of an element in the ionization stage z, and $\varkappa_z$ is the ionization energy of the species in the ionization stage z. For Eu, the electron density was estimated to be $n_e = 1.07 \times 10^{15}$ cm^{-3}.

5.5.2.8 Conclusions

Underwater LIBS was performed for the study of two rare earth elements Eu and Yb in aqueous solutions at ambient and elevated CO_2 pressures. Strong emission lines of Eu and Yb were detected in the spectra by creating a laser-induced spark in the bulk liquid solutions. Time-resolved analysis of plasma emission inferred that the increase in the surrounding pressure shortens the lifetime of spectral lines, which indicates the effect of pressure at later stages of plasma emission. Effects of laser energy and CO_2 pressure on the LIBS spectra were investigated in the pressure range of ambient to 250 bars. Comparing the results observed in this study with the reports in literatures, the effect of energy appeared to depend on the elements, analyte lines, and experimental conditions. Variation of intensity, area under curve (AUC), and width (FWHM) of two Eu lines and one Yb line with CO_2 pressure was analyzed. Observations suggested that the CO_2 pressure has an effect in the beginning when CO_2 is injected in to the solution, which was initially at ambient conditions. Spectral line intensity was reduced probably due to plasma confinement and shielding. After dissolving of CO_2 into the solution, plasma emission was observed to be less sensitive with the increase in its pressure. For the quantification, calibration models were developed by using two strong spectral lines of Eu (Eu (I) 459.40 and Eu (II) 420.50 nm) and one Yb line (Yb (I) 398.79 nm) in the

concentration range of 500-10000 ppm for each element. Limits of detection for Eu and Yb were estimated to be 209 and 156 ppm, respectively.

REFERENCES

[1] C. W. Noack*, et al.*, "Rare earth element geochemistry of outcrop and core samples from the Marcellus Shale," *Geochemical transactions,* vol. 16, pp. 1-11, 2015.

[2] K. Gschneidner Jr and V. Pecharsky, "Rare Earth: Science, Technology and Applications III, The Minerals, Metals, & Materials Society," ed: Warrendale, PA, 1997.

[3] C. Zhanheng, "Global rare earth resources and scenarios of future rare earth industry," *Journal of rare earths,* vol. 29, pp. 1-6, 2011.

[4] S. Vijayan*, et al.*, "Rare earths," *Min. Eng.(Littleton, Colo.);(United States),* vol. 41, 1989.

[5] S. I. Levy, "rare earths, their occurrence, chemistry, and technology," 1924.

[6] B. Zawisza*, et al.*, "Determination of rare earth elements by spectroscopic techniques: a review," *Journal of Analytical Atomic Spectrometry,* vol. 26, pp. 2373-2390, 2011.

[7] C. W. Noack*, et al.*, "Determination of Rare Earth Elements in Hypersaline Solutions Using Low-Volume, Liquid–Liquid Extraction," *Environmental science & technology,* vol. 49, pp. 9423-9430, 2015.

[8] G. Neupane and D. S. Wendt, "Assessment of Mineral Resources in Geothermal Brines in the US."

[9] X. Wang*, et al.*, "Rare earth elements in hydrothermal fluids from Kueishantao, off northeastern Taiwan: Indicators of shallow-water, sub-seafloor hydrothermal processes," *Chinese Science Bulletin,* vol. 58, pp. 4012-4020, 2013.

[10] A. Mitra*, et al.*, "Rare earth elements in submarine hydrothermal fluids and plumes from the Mid-Atlantic Ridge," *Marine Chemistry,* vol. 46, pp. 217-235, 1994.

[11] J. Fedorowich*, et al.*, "A rapid method for REE and trace-element analysis using laser sampling ICP-MS on direct fusion whole-rock glasses," *Chemical Geology,* vol. 106, pp. 229-249, 1993.

[12] D. Rusak*, et al.*, "Fundamentals and applications of laser-induced breakdown spectroscopy," *Critical Reviews in Analytical Chemistry,* vol. 27, pp. 257-290, 1997.

[13] K. Melessanaki, *et al.*, "The application of LIBS for the analysis of archaeological ceramic and metal artifacts," *Applied surface science,* vol. 197, pp. 156-163, 2002.

[14] G. Hubmer, *et al.*, "Application of LIBS to the in-line process control of liquid high-alloy steel under pressure," *Analytical and bioanalytical chemistry,* vol. 385, pp. 219-224, 2006.

[15] M. Dong, *et al.*, "Application of LIBS for direct determination of volatile matter content in coal," *Journal of Analytical Atomic Spectrometry,* vol. 26, pp. 2183-2188, 2011.

[16] A. K. Knight, *et al.*, "Characterization of laser-induced breakdown spectroscopy (LIBS) for application to space exploration," *Applied Spectroscopy,* vol. 54, pp. 331-340, 2000.

[17] C. R. Bhatt, *et al.*, "Study of atomic and molecular emission spectra of Sr by laser induced breakdown spectroscopy (LIBS)," *Appl Opt,* vol. 54, pp. 10264-71, Dec 01 2015.

[18] P. Fichet, *et al.*, "Determination of impurities in uranium and plutonium dioxides by laser-induced breakdown spectroscopy," *Applied Spectroscopy,* vol. 53, pp. 1111-1117, 1999.

[19] V. K. Singh and A. K. Rai, "Prospects for laser-induced breakdown spectroscopy for biomedical applications: a review," *Lasers in medical science,* vol. 26, pp. 673-687, 2011.

[20] D. Alamelu, *et al.*, "Laser-induced breakdown spectroscopy for simultaneous determination of Sm, Eu and Gd in aqueous solution," *Talanta,* vol. 77, pp. 256-261, 2008.

[21] V. Unnikrishnan, *et al.*, "Calibration based laser-induced breakdown spectroscopy (LIBS) for quantitative analysis of doped rare earth elements in phosphors," *Materials Letters,* vol. 107, pp. 322-324, 2013.

[22] K. Abedin, *et al.*, "Identification of multiple rare earths and associated elements in raw monazite sands by laser-induced breakdown spectroscopy," *Optics & Laser Technology,* vol. 43, pp. 45-49, 2011.

[23] M. Martin, *et al.*, "Quantification of rare earth elements using laser-induced breakdown spectroscopy," *Spectrochimica Acta Part B: Atomic Spectroscopy,* vol. 114, pp. 65-73, 2015.

[24] S. J. Rehse and C. A. Ryder, "Laser-induced breakdown spectroscopy for branching ratio and atomic lifetime measurements in singly-ionized neodymium and gallium," *Spectrochimica Acta Part B: Atomic Spectroscopy,* vol. 64, pp. 974-980, 2009.

[25] NIST Atomic Spectra Database [Online]. Available: https://www.nist.gov/pml/atomic-spectra-database

[26] S. M. Clegg*, et al.*, "Multivariate analysis of remote laser-induced breakdown spectroscopy spectra using partial least squares, principal component analysis, and related techniques," *Spectrochimica Acta Part B: Atomic Spectroscopy,* vol. 64, pp. 79-88, 2009.

[27] *The Unscrambler*. Available: http://www.camo.com/helpdocs/The_Unscrambler_Method_References.pdf

[28] L. Xu and I. Schechter, "Wavelength selection for simultaneous spectroscopic analysis. Experimental and theoretical study," *Analytical Chemistry,* vol. 68, pp. 2392-2400, 1996.

[29] T. Hussain*, et al.*, "Measurement of nutrients in green house soil with laser induced breakdown spectroscopy," *Environmental monitoring and assessment,* vol. 124, pp. 131-139, 2007.

[30] J.-I. Yun*, et al.*, "Selective Determination of Europium(III) Oxide and Hydroxide Colloids in Aqueous Solution by Laser-Induced Breakdown Spectroscopy," *Applied spectroscopy,* vol. 55, pp. 273-278, 2001/03/01 2001.

[31] T. Bundschuh*, et al.*, "Determination of size, concentration and elemental composition of colloids with laser-induced breakdown detection/spectroscopy (LIBD/S)," *Fresenius' journal of analytical chemistry,* vol. 371, pp. 1063-1069, 2001.

[32] P. K. Kennedy*, et al.*, "Laser-induced breakdown in aqueous media," *Progress in Quantum Electronics,* vol. 21, pp. 155-248, 1997.

[33] F. Docchio*, et al.*, "Study of the temporal and spatial dynamics of plasmas induced in liquids by nanosecond Nd:YAG laser pulses. 2: Plasma luminescence and shielding," *Appl Opt,* vol. 27, pp. 3669-74, Sep 01 1988.

[34] A. P. Michel*, et al.*, "Laser-induced breakdown spectroscopy of bulk aqueous solutions at oceanic pressures: evaluation of key measurement parameters," *Applied optics,* vol. 46, pp. 2507-2515, 2007.

[35] H. M. Hou*, et al.*, "Study of pressure effects on laser induced plasma in bulk seawater," *Journal of Analytical Atomic Spectrometry,* vol. 29, pp. 169-175, Jan 2014.

[36] B. Thornton and T. Ura, "Effects of Pressure on the Optical Emissions Observed from Solids Immersed in Water Using a Single Pulse Laser," *Applied Physics Express,* vol. 4, Feb 2011.

[37] D. Devia*, et al.*, "Métodos empleados en el análisis de espectroscopia óptica de emisión: una revisión," *Ingeniería y Ciencia,* vol. 11, pp. 239-268, 2015.

[38] V. Unnikrishnan*, et al.*, "Measurements of plasma temperature and electron density in laser-induced copper plasma by time-resolved spectroscopy of neutral atom and ion emissions," *Pramana J. Phys,* vol. 74, pp. 983-993, 2010.

[39] H. R. Griem, *Principles of plasma spectroscopy* vol. 2: Cambridge University Press, 2005.

[40] C. Aragón and J. A. Aguilera, "Characterization of laser induced plasmas by optical emission spectroscopy: A review of experiments and methods," *Spectrochimica Acta Part B: Atomic Spectroscopy,* vol. 63, pp. 893-916, 2008.

CHAPTER VI

SUMMARY AND RECOMMENDATIONS FOR FUTURE RESEARCH

In this chapter, a summary of the dissertation described in chapter two through chapter five on the laser-induced breakdown spectroscopy for material characterization is presented. In addition, some recommendations for future research in this field are also presented.

In chapter two, quantitative and qualitative analyses of atomic and molecular emissions of Sr are described. Binary mixtures of $SrCl_2$ and Al_2O_3 with varying concentration in powder form were used to record LIBS spectra for the analysis. Four spectral lines of Sr (430.54, 460.73, 481.18 and 548.08 nm) free from self-absorption and having good intensity profile were used for the study of atomic emission. When spectra were recorded at longer gate delays and gate widths, molecular bands of SrCl and SrO were observed. Three small spectral regions were selected for both SrCl and SrO bands to study the molecular emission from Sr. Background subtracted intensity, area under curve (AUC), and normalized area under curve of selected spectral lines and bands were plotted as a function of Sr concentration to prepare calibration models. These calibration models were validated with other samples which were not used in the models. Linear relationship of intensity and AUC of spectral lines and bands with Sr concentration was observed for lower values of concentration while for higher concentration, saturation effect was

observed. The values of limits of detection of Sr by using these lines and bands were also estimated.

Chapter three presents the study of presence of various nutrients in organic and conventional vegetables by LIBS method. Spectral lines of Ca, Mg, K, Na, and Fe were identified in the spectra obtained from both organic and conventional cauliflower as well as broccoli. Identification of different spectral lines confirms the presence of elements Ca, Mg, K, Na, and Fe in cauliflower and broccoli. To distinguish between organic and conventional vegetables in terms of nutrient elements, one- to-one comparison of spectral line intensity using Student's t test and PCA of LIBS spectra were performed. It is inferred that there should not be consistently systematic difference in nutritional status of organic and conventional vegetable flowers just on being so. It is suggested that it may depend on the circumstances under which these vegetable flowers are grown, seed quality or seed variety, geographical location of the farm, climatic conditions, soil quality in which they are grown, naturally and manually provided fertilizers' quality, etc.

In chapter four, an application of LIBS technique for the analysis of historic charcoal blast furnace slags is described. Ten slag samples were collected from iron furnace sites in eastern (2 samples) and northwestern (8 samples) Pennsylvania. The principal years of furnace operation at these sites were between 1833 and 1857. Spectral lines of Al, Ca, Fe, K, Mg, Mn, and Si were identified in the LIBS spectra recorded from these slag samples. For the quantification of analytes, multivariate analysis was performed. Partial least squares regression (PLS-R) models were developed by using the Unscrambler software. Here, nine samples were used to develop the models and one sample was used to check the predictive capacity of these models. Prediction results were

compared with those obtained by ICP-OES analysis and relative differences were found to be less than 25% taking ICP values as reference. Limits of detection for Al, Ca, Fe, K, Mg, Mn, and Si, were estimated to be 0.10, 0.22, 0.02, 0.01, 0.01, 0.005, and 0.18 wt % respectively.

Study of various rare earth elements by laser induced breakdown spectroscopy is described in chapter five. Detection and quantification of REEs in standard samples, natural geological samples, and aqueous solutions are separately discussed. In the first part, univariate and multivariate LIBS analyses of six rare earth elements [cerium (Ce), europium (Eu), gadolinium (Gd), neodymium (Nd), samarium (Sm), and yttrium (Y)] in standard powder samples are presented. LIBS study of REE in natural geological samples with their low concentration is described in the second part. Spectral lines of Ce, La, Nd, Y, Pr, Sm, Eu, Gd, and Dy were identified in the LIBS spectra recorded from those natural samples. Partial least squares regression (PLS-R) models were developed for the quantification of Ce, La, and Nd. Prediction capacity of these models was evaluated by comparing values predicted by these models with those obtained from ICP-MS analysis. These two studies of REEs in standard and natural geological samples showed the possibility of using LIBS technique for their qualitative and quantitative analyses in solid sources. To evaluate an application of LIBS for the study of REEs in liquid samples in an oceanic environment, LIBS analysis of Eu and Yb in their aqueous solutions is presented in the third part of chapter five. Temporal evolution of plasma, effect of laser pulse energy and surrounding pressure in plasma emission are described by analyzing under water LIBS spectra recorded at ambient and elevated CO_2 pressure conditions. Calibration models for Eu and Yb were developed for their quantification and limits of

detection were estimated be 209 and 156 ppm for Eu and Yb, respectively. Overall, the studies reported in chapters 2 through 5 showed the possibility of using LIBS as a robust analytical technique for rapid material characterization even in harsh environment, which is unattainable with existing traditional techniques.

Recommendations for Future Research

In chapter two, atomic and molecular emission of Sr are described for its quantification and $SrCl_2$ in Al_2O_3 matrix was used as sample. This showed the possibility of using atomic and molecular emission simultaneously in LIBS for material characterization. To enhance its scope, it is recommended to perform a similar study of different other elements using various sample matrices. Future work should also be able to explain matrix effect and other environmental effects.

Comparative study of elemental nutrients in organic and conventional vegetables by LIBS technique is presented by the case study of cauliflower and broccoli in chapter three. This study should be widened by studying other vegetables grown at various locations and known environmental conditions. Moreover, the results obtained from LIBS analysis can be compared with those obtained by other established techniques.

In chapter five, qualitative and quantitative analyses of some REEs are explained. It is recommended to execute LIBS study for all the REEs in various natural resources. I have described under water LIBS for only two elements (Eu and Yb), future work should include maximum number of REEs in various matrices. To better understand the underwater plasma of REEs, an imaging technique can be coupled with LIBS and phenomena, like matrix effect and self-absorption can be explained.